Title
Noradrenergic signaling acts through astrocytes to modulate cortical activity and state

Author
Reitman, Michael

Publication Date
2022

Peer reviewed|Thesis/dissertation

Noradrenergic signaling acts through astrocytes to modulate cortical activity and state

by
Michael Reitman

DISSERTATION
Submitted in partial satisfaction of the requirements for degree of
DOCTOR OF PHILOSOPHY

in

Neuroscience

in the

GRADUATE DIVISION
of the
UNIVERSITY OF CALIFORNIA, SAN FRANCISCO

Approved:

DocuSigned by:
Erik Ullian
1ACF3D77A55F4F0...

Erik Ullian
Chair

DocuSigned by:
Kira Poskanzer
DocuSigned by:
Evan Feinberg
DocuSigned by:
Michael Stryker
15DFF21E2A5440C...

Kira Poskanzer
Evan Feinberg
Michael Stryker

Committee Members

ACKNOWLEDGEMENTS

For my inspirations: Rose, Jen, and Mihir, who kept me from being lost. For my steadfast supporters: Ben, Sofia, and Eszter who gave me love when I was full and when I was lacking. And for the pieces of my heart: Rich, Martha, Alex, Karen, Baruch and Itai, who I feel with me every day.

CONTRIBUTIONS

This thesis was written by Michael E. Reitman. It represents ongoing and unpublished work and was generated in collaboration with Vincent Tse, Xuelong Mi, Alba Peinado, Alexander Aivazidis, Bat-Erdene Myagmar, Paul C. Simpson, Jr., Omer A. Bayraktar, Guoqiang Yu, and Kira E. Poskanzer.

M.E.R. and K.E.P. designed the study. M.E.R., V.T., and A.A. conducted the experiments. M.E.R., X. M., V.T., A.P., and A.A. analyzed the data. B.M. and P.C.S. developed the mutant mouse line. M.E.R and K.E.P. wrote the results. O.A.B., G.Y. and K.E.P managed the project and provided financial support.

NORADRENERGIC SIGNALING ACTS THROUGH ASTROCYTES TO MODULATE CORTICAL ACTIVITY AND STATE

Michael Reitman

ABSTRACT

There is growing evidence that non-neuronal cells in the nervous system, particularly astrocytes, have their own distinct patterns of activity and may act as additional players in the physiological functioning of neural circuits. However, the drivers and pattern of physiological astrocyte activity, its relationship to neuromodulatory signaling and local circuit activity, and its role in neural circuits is not known. Using a combination of *in vivo* two-photon imaging, electrophysiology, pharmacology, and genetic and chemogenetic perturbations in mouse visual cortex, I describe structured astrocyte activity patterns driven by the monoamine norepinephrine across behavioral states which alters the level and pattern of activity in the nearby cortical circuit. These results likely extend bi-hemispherically through an inhibitory pathway downstream of astrocyte activity. In sum, this work indicates that astrocytes act as a distinct neuromodulatory pathway for regulating the amount and pattern of nearby neuronal activity in the typical wakeful functioning of the cortex, and builds on a growing literature directly implicating astrocytes as crucial components in neural circuits.

TABLE OF CONTENTS

Introduction 1

References 12

NE links astrocytic activity to regulation of cortical state 24

1.1 Abstract 24

1.2 Introduction 24

1.3 Results 27

1.4 Discussion 48

1.5 Methods 53

1.6 Figures 69

1.7 Extended Data 83

1.8 References 99

Conclusion 111

LIST OF FIGURES

Figure 1. Changes in arousal shape astrocyte Ca^{2+} activity independent of locomotion. 70

Figure 2. Astrocytes are sensitive to a range of norepinephrine increases. 72

Figure 3. Astrocyte Ca^{2+} precedes increased neuronal activity following spontaneous arousal. 74

Figure 4. Arousal-driven astrocyte Ca^{2+} is not dependent on local neuronal activity. 75

Figure 5. NE-dependent astrocyte Ca^{2+} occurs at the crux of cortical state changes. 77

Figure 6. Adra1a receptors modulate basal neuronal activity and neuronal population responses to arousal. 79

Figure 7. Genetic removal of astrocyte Arda1a impairs cortical resynchronization after arousal. 81

Figure 8. Model of astrocyte regulation of arousal-associated cortical state. 82

Extended Data Figure 1. Dissection of astrocyte Ca^{2+} and behavioral state. 84

Extended Data Figure 2. Hemodynamic correction of 2P GRABNE signals 86

Extended Data Figure 3. Analysis of contributions to astrocyte Ca^{2+} 87

Extended Data Figure 4. Cortical astrocyte expression of adrenergic receptors. 88

Extended Data Figure 5. Generation of $Adra1a^{fl/fl}$ mice. 89

Extended Data Figure 6. Astrocyte-specific Cre expression. 91

Extended Data Figure 7. Increased activity in $Adra1a^{fl/fl}$ mice imaging at 7.5Hz. 92

Extended Data Figure 8. Quantification of arousal-associated neuronal activity 94

LIST OF TABLES

Supplementary Table 1. Statistics for Fig. 1d 95

Supplementary Table 2. Statistics for Fig. 2h 96

Supplementary Table 3. Supplementary Table 3: Statistics for Fig. 2j 97

Supplementary Table 4. Statistics for Fig. 4d 98

LIST OF ABBREVIATIONS

Calcium – Ca^{2+}

Locus Coeruleus - LC

Norepinephrine – NE

INTRODUCTION

From anatomy to function: studying astrocytes in physiological circuits

A major priority in modern neuroscience is well summarized by the first two goals listed in the NIH Brain Research Through Advancing Innovative Neurotechnologies (BRAIN) 2025 report which are “#1. Discovering diversity: Identify and provide experimental access to the different brain cell types to determine their roles in health and disease” and “#2. Maps at multiple scales: Generate circuit diagrams that vary in resolution from synapses to the whole brain” [1]. These goals together aim to generate what is commonly referred to as a “wiring diagram” or “connectome”, a full list of the constituent parts that make up the brain and their connections[2]. While this is a necessary step for understanding the brain, extensive work in organisms for which a complete anatomical description is available, such as the worm *Caenorhabditis elegans* and the crustacean stomatogastric ganglion, have demonstrated that such a diagram is not sufficient for understanding the principles and functions of neural circuits[3]. Rather, we must also investigate the interplay between the activity patterns of different cells, and cell-types, in the nervous system and form theoretical models for their fundamental roles in neural circuits. This perspective has been particularly useful in describing neuromodulators—signaling molecules that can alter patterns of activity in neural circuits—and their role in neural circuits[4]. However, this approach has primarily focused on molecular neuromodulators and cellular mechanisms that come from neuronal sources.

There is growing evidence that non-neuronal cells in the nervous system, particularly astrocytes, have their own distinct patterns of activity and may act as additional players

in the physiological functioning of neural circuits[5]. Current descriptions of the activity patterns of astrocytes, how their activity relates to activity patterns of nearby neurons and the neural circuit as a whole, as well as the downstream consequences of astrocyte activity, are substantially more rudimentary than for their neuronal counterparts. In this thesis, I investigate these questions: what does the physiological pattern of astrocyte activity look like, how does it relate to known neuromodulatory signaling, how does it relate to the activity of the nearby neural circuit, and what could this astrocytic activity contribute to neural circuit function. I use the mouse visual cortex as a model system for its genetic access and well characterized functional and anatomical properties. Using this system, I describe a deeper structure to astrocyte activity than previously understood, and link a particular type of astrocytic activity, NE/arousal-driven astrocyte activity, to changes in the amount and pattern of neuronal circuit activity. Further evidence demonstrates that this pattern, while pronounced in the visual cortex, may be regional, with profoundly different activity patterns observed in the prefrontal cortex. Therefore, from a narrow perspective this work provides a better understanding of how patterns of activity in the mouse visual cortex are controlled and from a broader perspective this work furthers our understanding of general nervous system principles and how astrocytes can be actively integrated into descriptions of neural circuits.

The mouse visual cortex as a model system

The visual cortex provides a powerful model system for understanding the form and function of complex neural circuits. It has a highly conserved anatomy across the mammalian lineage which has allowed for deep understandings of the role of the cortex in sensation and behavior[6]. This anatomy consists of multiple layers distinguished by

the organization of cells and connections whose functional relevance have been extensively studied, with the canonical structure described as an input layer (IV) which projects to a processing layer (II/III) and deep output layers (V/VI), although the true organization is substantially more complex[7]. In addition, the functional properties of this cortical region have also been studied, and its relevance to sensation is starkly apparent[8]. It receives major direct projections from the visual thalamus, which directly receives inputs from the retina, and the cells in visual cortex are highly responsive to visual input, contrast, and borders. This brain region then has an extensive cortical and subcortical projection system which allows it to share visual information with higher order visual areas and other brain regions[9,10]. In the mouse, there are a variety of methods and tools to record from and genetically alter the visual circuit, which has greatly advanced understandings of the computational and functional properties of the cortex[6,11].

The mouse visual cortex is also an excellent system for studying how circuit activity is shaped and modulated over time. It exhibits structured spontaneous patterns of neural activity, even in the absence of external visual stimuli. These endogenous patterns are dynamic and shift between states characterized by synchronized or desynchronized neural activity[12]. Changes in behavioral state, such as the initiation of locomotion, are accompanied by desynchronization of the cortex and dramatic modulation of neuronal and circuit properties[13]. These cortical state changes are not solely due to motor feedback but are also due to concurrent changes in arousal[14], which can be (noisily) read out by external biomarkers such as pupil diameter[15,16]. Indeed, spontaneous changes in arousal during stationary periods have been shown to modulate cortical

state as well[17]. Importantly, these changes are also not epiphenomenal. Patterns of spontaneous cortical activity have been shown to be a major determinant of sensory perception and cortical function[18].

Overall, the genetic access, well-defined anatomy, and dynamic spontaneous activity changes in the mouse visual cortex make it a powerful system for understanding circuits and their modulation overtime. However, despite the extensive work in visual cortex, it is only relatively recently that non-neuronal cells, such as astrocytes, have begun to be incorporated into models of circuit function.

Astrocytes observe and respond to neuronal signaling

Astrocytes are one of the most abundant cell types in the brain and play a critical role in synaptic formation, regulation of the extracellular environment, modulation of neurovascular coupling, and neurotransmitter transport/reuptake[19]. They appear throughout the mammalian lineage and have been identified in rodents, ferrets[20], and primates[21], including humans[22]. More recently, astrocyte-like cells have characterized in flies[23], and fish[24], and there is evidence of non-neuronal cells that serve similar roles to mammalian astrocytes in as evolutionarily divergent species from human as worms[25]. These results suggest necessary and conserved functions for astrocytes across evolution[26]. Despite the importance of astrocytes, the majority of studies have investigated the role of astrocytes in the formation of the nervous system, as regulators of metabolism and waste clearance, and in disease states[27]. Relatively little is known about the activity of these cells in the baseline function of neural circuits.

Astrocytes are sensitive to neurotransmitters, particularly NE

Historically the role of astrocytes in neural circuit function has been studied *ex vivo*, and many early advances were made using dissociated cultures or brain slices. Studies in the late twentieth century built on initial observations of glial responses to neuronal activity[28], and showed compellingly that astrocytes show both changes in membrane potential[29], and increases in intracellular Ca^{2+} elevations in response to glutamate[30], one of the primary neurotransmitters in the mammalian nervous system. Additional studies soon indicated that astrocytes are sensitive to a variety of neurotransmitters, including the other primary mammalian neurotransmitter GABA[31]. With modern bulk and single-cell sequencing techniques, receptors and transporters for many of the main neurotransmitters in the nervous system have now been identified on astrocytes, both in rodents and humans[32–34]. However, whether astrocytes are actually sensitive to physiological levels of *in vivo* neuronal activity remained an outstanding question.

With advances in optical techniques, developments in Ca^{2+} dyes, and the advent of genetically encoded Ca^{2+} indicators, *in vivo* imaging of astrocyte Ca^{2+} activity became possible[35]. Primarily looking in the mouse neocortex due to ease of accessibility and the aforementioned well established anatomy and circuit properties, experiments were performed to observe both the spontaneous activity and sensory stimulation-driven responses of astrocytes[36,37]. These studies revealed that *in vivo* neuronal activity could drive astrocyte activity, suggesting a physiological role for astrocytic signaling in response to classical neurotransmitters. Contemporaneously, studies of *in vivo* Ca^{2+} activity also described a novel form of astrocyte activity that does not occur *ex vivo*: large “bursts” of population-wide increases in Ca^{2+} signaling[38]. This activity sparked

great interest, both because these were very large and robust increases in astrocyte activity, and because it seemed to depend on the active function of the cortex; anesthesia abolished these bursts of Ca^{2+} activity[39]. Intriguingly, pharmacological blockade experiments indicated that this type of astrocyte activity was not dependent on glutamatergic or purinergic signaling. Instead, using a LC-specific toxin or direct application of pharmacological ligands *in vivo*, it was determined that the neuromodulator NE was the primary driver of astrocyte Ca^{2+} bursts[40,41]. These findings have since been corroborated in further studies[42,43].

The Locus Coeruleus and norepinephrine in the mouse neocortex

Anatomical projections of the LC

Like many classical neurotransmitters, NE is a small molecule derived from a single amino acid. For NE, its derivation comes from tyrosine through a biosynthetic pathway which includes the neurotransmitter dopamine which then is converted by one enzyme, Dopamine β-hydroxylase, into NE[44]. In the mid-twentieth century, the presence and projection patterns of NE-containing neurons was investigated using autoradiography[45], immunohistochemistry[46], and fluorescent histochemistry[47,48]. These studies conclusively showed that in the mammalian forebrain, the sole source of NE comes from one small nucleus in the brain stem known as the Locus Coeruleus (LC)[49]. This nucleus has wide-spread projections to almost all brain regions, with the notable exception of the striatum, and unlike classical synapses, these projections often have pronounced varicosities which are thought to release large amounts of NE into the extracellular space extrasynaptically, a process termed volume transmission[50,51]. More specifically in the cortex, the LC projects to all layers, although there is potentially preferential volume

transmission in the superficial and deep layers as indicated by greater varicosities[52]. Although it was initially thought that the LC was a homogenous collection of cells, recent work suggests there is some level of variation in both the projection and activity patterns of neurons, suggesting that there may be both global and more specific functions for these cells and NE throughout the brain[53,54]. The function of this heterogeneity is unknown and may interact with the multiple receptor subtypes for NE to provide brain-region, circuit, or even cell-type specific effects.

NE receptor subtypes

NE is sensed primarily through G-protein coupled receptors which have been grouped into two main families, α-receptors and β-receptors. β-receptors are generally Gs-coupled and the α-receptors have been divided into two subfamilies, the Gq-coupled α1 and Gi/o-coupled α2 receptors[55]. These receptor families not only differ in their signaling mechanisms, but have also been reported to have different affinities for NE, with the β-receptors likely having lower affinity than the α-receptors[56]. This contrasts with recent summaries of NE receptor affinites[57], although much of this work was conducted using biochemical assays of purified tissue outside the nervous system. Therefore, while it is possible there are different receptor affinities for NE, the endogenous affinities of these receptors in the nervous system are not fully known. Furthermore, the role of NE signaling through different receptors, and how that may affect different cellular populations is also not well known. This is true for both neuronal and astrocyte populations, which have been shown through bulk and single-cell RNA sequencing to express many of the NE receptors[32–34]. Instead, rather than focusing on cell-type specific signaling pathways, much of the current work on NE function in the cortex has

used LC stimulation and pharmacology to determine the functional roles of NE and its role in shaping circuit activity.

LC affects neuronal activity and cortical state

The function of NE both in the nervous system as a whole, and in the cortex specifically, has been studied in terms of its effect on individual neurons, circuit activity, and behavior[58]. Much of the interpretation of its role has been influenced by the state-specific nature of LC activity, which is particularly high during wakefulness and robustly increases with startle, or movement, while being suppressed during sleep[59–62]. These findings have led to the labeling of NE as an arousing neuromodulator. Contemporary work using the specificity afforded by mouse genetics and optogenetic techniques has corroborated these findings, suggesting that on a broad-scale, the LC controls arousal and wakefulness[63].

At the level of individual neurons, NE has been shown to raise the resting membrane potential by reducing a potassium leak current, for both inhibitory and excitatory neurons[64,65]. *In vivo*, this phenomenon is also apparent, and experiments using locally applied NE antagonists lead to the conclusion that NE acts to not only tonically depolarize neurons, but also to reduce spontaneous and visual stimulation evoked neuronal activity[66]. Conversely, direct application of NE into the cortex has been shown to increase the ratio of evoked to spontaneous activity in subpopulations of cortical neurons[67,68] although these results are not always consistent[69]. However, on the whole, the majority of the literature suggests that NE acts to increase the signal-to-noise ratio of incoming signals in the brain[58]. This finding that NE can sensitize the cortex for external information matches circuit-level investigations which find that phasic electrical

or optogenetic activation of the LC drives patterns of activity which sensitize the cortex to sensory stimulation across behavioral states[70–72]. Despite these advances in our understanding of the actions of NE and the LC on single neurons and cortical circuits, the full range of receptor subtype-specific effects of NE, and indirect effects of NE through non-neuronal cellular populations have not been explored. Given the strong responses of astrocytes to NE, and previous work suggesting that astrocytes can modulate cortical circuit activity, astrocytic contributions to cortical circuit function downstream of NE has become a compelling research avenue.

Astrocytic regulation of neuronal activity and cortical circuit function

Building on observations that astrocytes respond to many neurotransmitters, determining the functions of neurotransmitter-mediated astrocyte activity became a main goal for the field. Within the last few decades, roles for astrocytes in manipulating the function of neuronal activity has become more fully established. Some of the earliest and most consistent descriptions for the role of astrocyte activation downstream of neuromodulators have found that neurotransmitter-mediated stimulation can result in changes in the extracellular concentration of potassium[28,73–76] and glutamate[77–79] leading primarily to increases in the activity of nearby neurons. Further studies have expanded our understanding of the molecular repertoire astrocytes may employ to modulate neuronal activity. Currently proposed mechanisms include not only the release or change in uptake of classical neurotransmitters, but also purinergic signaling pathways[80], release of co-factors for neurotransmitter receptors such as D-serine[81], and a variety of non-canonical small molecules such as nitric oxide[82] and arachidonic acid[83]. These variety of mechanisms have also been linked to a variety of effects on neuronal

activity and electrophysiological properties beyond the simple initial descriptions of activation. Current models propose that astrocytic modulation can lead both to activation and inhibition of neuronal activity as well as changes in both pre- and post-synaptic properties including either facilitation and depression over multiple timescales[84,85]. Based on the wide range of effectors that astrocytes can use, and the diversity of neuronal responses to these effectors, extrapolation of the role of astrocytes in circuit function from their modulation of single neurons is challenging. Therefore, contemporary studies have started to expand to include the role of astrocytes in circuit activity and function.

Astrocytes as modulators of cortical state

Only much more recently have the implications for astrocytes on circuit properties begun to be explored, particularly *in vivo*. In the last decade, studies from multiple laboratories have identified that one role for cortical astrocytes may be as key contributors to the generation and regulation of cortical oscillations. Experiments using inhibitory or excitatory manipulations of astrocytes demonstrated their capacity to generate slow oscillations *in situ*[86], under anesthesia[87], and in the context of sleep[88,89], suggesting astrocytes may play a synchronizing role in cortical circuits. While these studies did not clearly identify the input mechanisms that lead to astrocyte-mediated synchrony, contemporary work from multiple groups has reproduced initial findings that astrocytes are sensitive to physiological levels of sensory stimuli-driven neural activity across sensory areas[90–92], and a recent study suggests this leads to reduced sensitivity and increased network synchronization[93]. In contrast, other work in the prefrontal cortex has identified that GABAergic signaling to astrocytes causes general neuronal excitation

and gamma oscillations which effect behavior[94]. Therefore, while astrocytic contributions to neuronal oscillations are now recognized, there may be input and region-specific roles for astrocyte in the modulation of cortical circuits.

Does NE signaling to astrocytes influence cortical state?

Crucially, previous work has rarely described the role of NE signaling to astrocytes in modulation of neuronal activity or cortical state. This is despite intense speculation in the field due to both the robust activation of cortical astrocytes by arousal and NE and overlapping mechanisms of action by NE with known astrocytic functions (i.e. changes in neuronal potassium currents, changes in neuronal activity, and modulation of cortical state)[95–97]. This interest has been compounded by recent identification of the role of NE signaling to astrocytes in other brain regions and model systems. Across multiple species, NE-driven astrocytic involvement in inhibiting motor output and sensory input at the level of the brain stem/spinal cord[98–100]. However, in the cortex current roles for NE-driven astrocyte fundamental questions about the regionalization, structure, and role of cortical astrocyte activation by NE remain unanswered. Here we build on previous work to better define the relationship between astrocyte activity, NE, and cortical circuit function and propose a region-specific role for astrocytes in regulating cortical state downstream of NE.

References

1. Bargmann, C., Newsome, W. & Anderson, A. BRAIN 2025: a scientific vision. *… Report to the Advisory …* (2014).

2. Cobb, M. A brief history of wires in the brain. *Frontiers in Ecology and Evolution* (2021).

3. Bargmann, C. I. & Marder, E. From the connectome to brain function. *Nat. Methods* **10,** 483–490 (2013).

4. Bargmann, C. I. Beyond the connectome: how neuromodulators shape neural circuits. *Bioessays* **34,** 458–465 (2012).

5. Hwang, S.-N., Lee, J. S., Seo, K. & Lee, H. Astrocytic regulation of neural circuits underlying behaviors. *Cells* **10,** (2021).

6. Niell, C. M. Cell types, circuits, and receptive fields in the mouse visual cortex. *Annu. Rev. Neurosci.* **38,** 413–431 (2015).

7. Adesnik, H. & Naka, A. Cracking the function of layers in the sensory cortex. *Neuron* **100,** 1028–1043 (2018).

8. Hübener, M. Mouse visual cortex. *Curr. Opin. Neurobiol.* **13,** 413–420 (2003).

9. Swadlow, H. A. Efferent systems of primary visual cortex: a review of structure and function. *Brain Res.* **287,** 1–24 (1983).

10. Froudarakis, E. *et al.* The visual cortex in context. *Annu. Rev. Vis. Sci.* **5,** 317–339 (2019).

11. Niell, C. M. & Scanziani, M. How cortical circuits implement cortical computations: mouse visual cortex as a model. *Annu. Rev. Neurosci.* **44,** 517–546 (2021).

12. Steriade, M. Grouping of brain rhythms in corticothalamic systems. *Neuroscience* **137,** 1087–1106 (2006).

13. Niell, C. M. & Stryker, M. P. Modulation of visual responses by behavioral state in mouse visual cortex. *Neuron* **65,** 472–479 (2010).

14. Vinck, M., Batista-Brito, R., Knoblich, U. & Cardin, J. A. Arousal and locomotion make distinct contributions to cortical activity patterns and visual encoding. *Neuron* **86,** 740–754 (2015).

15. Larsen, R. S. & Waters, J. Neuromodulatory correlates of pupil dilation. *Front. Neural Circuits* **12,** 21 (2018).

16. Megemont, M., McBurney-Lin, J. & Yang, H. Pupil diameter is not an accurate real-time readout of locus coeruleus activity. *Elife* **11,** (2022).

17. McGinley, M. J. *et al.* Waking state: rapid variations modulate neural and behavioral responses. *Neuron* **87,** 1143–1161 (2015).

18. Hasenstaub, A., Sachdev, R. N. S. & McCormick, D. A. State changes rapidly modulate cortical neuronal responsiveness. *J. Neurosci.* **27,** 9607–9622 (2007).

19. Bazargani, N. & Attwell, D. Astrocyte calcium signaling: the third wave. *Nat. Neurosci.* **19,** 182–189 (2016).

20. Schummers, J., Yu, H. & Sur, M. Tuned responses of astrocytes and their influence on hemodynamic signals in the visual cortex. *Science* **320,** 1638–1643 (2008).

21. Colombo, J. A., Schleicher, A. & Zilles, K. Patterned distribution of immunoreactive astroglial processes in the striate (V1) cortex of New World monkeys. *Glia* **25,** 85–92 (1999).

22. Oberheim, N. A., Wang, X., Goldman, S. & Nedergaard, M. Astrocytic complexity distinguishes the human brain. *Trends Neurosci.* **29,** 547–553 (2006).

23. Freeman, M. R. Drosophila central nervous system glia. *Cold Spring Harb. Perspect. Biol.* **7,** (2015).

24. Chen, J., Poskanzer, K. E., Freeman, M. R. & Monk, K. R. Live-imaging of astrocyte morphogenesis and function in zebrafish neural circuits. *Nat. Neurosci.* **23,** 1297–1306 (2020).

25. Oikonomou, G. & Shaham, S. The glia of Caenorhabditis elegans. *Glia* **59,** 1253–1263 (2011).

26. Freeman, M. R. & Rowitch, D. H. Evolving concepts of gliogenesis: a look way back and ahead to the next 25 years. *Neuron* **80,** 613–623 (2013).

27. Molofsky, A. V. *et al.* Astrocytes and disease: a neurodevelopmental perspective. *Genes Dev.* **26,** 891–907 (2012).

28. Orkand, R. K., Nicholls, J. G. & Kuffler, S. W. Effect of nerve impulses on the membrane potential of glial cells in the central nervous system of amphibia. *J. Neurophysiol.* **29,** 788–806 (1966).

29. Hösli, L., Andrès, P. F. & Hösli, E. Depolarization of cultured astrocytes by glutamate and aspartate. *Neuroscience* **4,** 1593–1598 (1979).

30. Cornell-Bell, A. H., Finkbeiner, S. M., Cooper, M. S. & Smith, S. J. Glutamate induces calcium waves in cultured astrocytes: long-range glial signaling. *Science* **247,** 470–473 (1990).

31. MacVicar, B. A., Tse, F. W., Crichton, S. A. & Kettenmann, H. GABA-activated Cl- channels in astrocytes of hippocampal slices. *J. Neurosci.* **9,** 3577–3583 (1989).

32. Zhang, Y. *et al.* An RNA-sequencing transcriptome and splicing database of glia, neurons, and vascular cells of the cerebral cortex. *J. Neurosci.* **34,** 11929–11947 (2014).

33. Batiuk, M. Y. *et al.* Identification of region-specific astrocyte subtypes at single cell resolution. *Nat. Commun.* **11,** 1220 (2020).

34. Cahoy, J. D. *et al.* A transcriptome database for astrocytes, neurons, and oligodendrocytes: a new resource for understanding brain development and function. *J. Neurosci.* **28,** 264–278 (2008).

35. Tian, G.-F. *et al.* Imaging of cortical astrocytes using 2-photon laser scanning microscopy in the intact mouse brain. *Adv. Drug Deliv. Rev.* **58,** 773–787 (2006).

36. Wang, X. *et al.* Astrocytic Ca2+ signaling evoked by sensory stimulation in vivo. *Nat. Neurosci.* **9,** 816–823 (2006).

37. Hirase, H., Qian, L., Barthó, P. & Buzsáki, G. Calcium dynamics of cortical astrocytic networks in vivo. *PLoS Biol.* **2,** E96 (2004).

38. Nimmerjahn, A., Mukamel, E. A. & Schnitzer, M. J. Motor behavior activates Bergmann glial networks. *Neuron* **62,** 400–412 (2009).

39. Thrane, A. S. *et al.* General anesthesia selectively disrupts astrocyte calcium signaling in the awake mouse cortex. *Proc. Natl. Acad. Sci. USA* **109,** 18974–18979 (2012).

40. Ding, F. *et al.* α1-Adrenergic receptors mediate coordinated Ca2+ signaling of cortical astrocytes in awake, behaving mice. *Cell Calcium* **54,** 387–394 (2013).

41. Bekar, L. K., He, W. & Nedergaard, M. Locus coeruleus alpha-adrenergic-mediated activation of cortical astrocytes in vivo. *Cereb. Cortex* **18,** 2789–2795 (2008).

42. Paukert, M. *et al.* Norepinephrine controls astroglial responsiveness to local circuit activity. *Neuron* **82,** 1263–1270 (2014).

43. Ye, L. *et al.* Ethanol abolishes vigilance-dependent astroglia network activation in mice by inhibiting norepinephrine release. *Nat. Commun.* **11,** 6157 (2020).

44. Fernstrom, J. D. & Fernstrom, M. H. Tyrosine, phenylalanine, and catecholamine synthesis and function in the brain. *J. Nutr.* **137,** 1539S–1547S; discussion 1548S (2007).

45. DE Wolfe, Potter, L. T., Richardson, K. C. & Axelrod, J. Localizing tritiated norepinephrine in sympathetic axons by electron microscopic autoradiography. *Science* (1962).

46. Verhofstad, A. A., Steinbusch, H. W. & Penke, B. Use of antibodies to norepinephrine and epinephrine in immunohistochemistry. *Advances in …* (1980).

47. Corrodi, H. & Jonsson, G. Fluorescence methods for the histochemical demonstration of monoamines: 4. Histochemical differentiation between dopamine and noradrenaline in models. *Journal of Histochemistry & …* (1965).

48. Lindvall, O., Björklund, A. & Falck, B. Letters to the editor: New principles for microspectrofluorometric differentiation between DOPA, dopamine and noradrenaline. *… of Histochemistry & …* (1975).

49. Swanson, L. W. & Hartman, B. K. The central adrenergic system. An immunofluorescence study of the location of cell bodies and their efferent connections in the rat utilizing dopamine-beta-hydroxylase as a marker. *J. Comp. Neurol.* **163,** 467–505 (1975).

50. Fuxe, K. *et al.* The discovery of central monoamine neurons gave volume transmission to the wired brain. *Prog. Neurobiol.* **90,** 82–100 (2010).

51. Descarries, L., Watkins, K. C. & Lapierre, Y. Noradrenergic axon terminals in the cerebral cortex of rat. III. Topometric ultrastructural analysis. *Brain Res.* **133,** 197–222 (1977).

52. Agster, K. L., Mejias-Aponte, C. A., Clark, B. D. & Waterhouse, B. D. Evidence for a regional specificity in the density and distribution of noradrenergic varicosities in rat cortex. *J. Comp. Neurol.* **521,** 2195–2207 (2013).

53. Schwarz, L. A. & Luo, L. Organization of the locus coeruleus-norepinephrine system. *Curr. Biol.* **25,** R1051–R1056 (2015).

54. Chandler, D. J., Gao, W.-J. & Waterhouse, B. D. Heterogeneous organization of the locus coeruleus projections to prefrontal and motor cortices. *Proc. Natl. Acad. Sci. USA* **111,** 6816–6821 (2014).

55. Molinoff, P. B. α-and β-Adrenergic Receptor Subtypes. *Drugs* (1984).

56. Ramos, B. P. & Arnsten, A. F. T. Adrenergic pharmacology and cognition: focus on the prefrontal cortex. *Pharmacol. Ther.* **113,** 523–536 (2007).

57. Wu, Y., Zeng, L. & Zhao, S. Ligands of adrenergic receptors: A structural point of view. *Biomolecules* **11,** (2021).

58. McBurney-Lin, J., Lu, J., Zuo, Y. & Yang, H. Locus coeruleus-norepinephrine modulation of sensory processing and perception: A focused review. *Neurosci. Biobehav. Rev.* **105,** 190–199 (2019).

59. Berridge, C. W., Schmeichel, B. E. & España, R. A. Noradrenergic modulation of wakefulness/arousal. *Sleep Med. Rev.* **16,** 187–197 (2012).

60. Aston-Jones, G. & Bloom, F. E. Activity of norepinephrine-containing locus coeruleus neurons in behaving rats anticipates fluctuations in the sleep-waking cycle. *J. Neurosci.* **1,** 876–886 (1981).

61. Foote, S. L., Aston-Jones, G. & Bloom, F. E. Impulse activity of locus coeruleus neurons in awake rats and monkeys is a function of sensory stimulation and arousal. *Proc. Natl. Acad. Sci. USA* **77,** 3033–3037 (1980).

62. Berridge, C. W. & Waterhouse, B. D. The locus coeruleus-noradrenergic system: modulation of behavioral state and state-dependent cognitive processes. *Brain Res Brain Res Rev* **42,** 33–84 (2003).

63. Carter, M. E. *et al.* Tuning arousal with optogenetic modulation of locus coeruleus neurons. *Nat. Neurosci.* **13,** 1526–1533 (2010).

64. McCormick, D. A., Wang, Z. & Huguenard, J. Neurotransmitter control of neocortical neuronal activity and excitability. *Cereb. Cortex* **3,** 387–398 (1993).

65. Kawaguchi, Y. & Shindou, T. Noradrenergic excitation and inhibition of GABAergic cell types in rat frontal cortex. *J. Neurosci.* **18,** 6963–6976 (1998).

66. Polack, P.-O., Friedman, J. & Golshani, P. Cellular mechanisms of brain state-dependent gain modulation in visual cortex. *Nat. Neurosci.* **16,** 1331–1339 (2013).

67. Kasamatsu, T. & Heggelund, P. Single cell responses in cat visual cortex to visual stimulation during iontophoresis of noradrenaline. *Exp. Brain Res.* **45,** 317–327 (1982).

68. Hasselmo, M. E., Linster, C., Patil, M., Ma, D. & Cekic, M. Noradrenergic suppression of synaptic transmission may influence cortical signal-to-noise ratio. *J. Neurophysiol.* **77,** 3326–3339 (1997).

69. Sato, H., Fox, K. & Daw, N. W. Effect of electrical stimulation of locus coeruleus on the activity of neurons in the cat visual cortex. *J. Neurophysiol.* **62,** 946–958 (1989).

70. Vazey, E. M., Moorman, D. E. & Aston-Jones, G. Phasic locus coeruleus activity regulates cortical encoding of salience information. *Proc. Natl. Acad. Sci. USA* **115,** E9439–E9448 (2018).

71. Devilbiss, D. M. & Waterhouse, B. D. Phasic and tonic patterns of locus coeruleus output differentially modulate sensory network function in the awake rat. *J. Neurophysiol.* **105,** 69–87 (2011).

72. Hayat, H. *et al.* Locus coeruleus norepinephrine activity mediates sensory-evoked awakenings from sleep. *Sci. Adv.* **6,** eaaz4232 (2020).

73. Kofuji, P. *et al.* Genetic inactivation of an inwardly rectifying potassium channel (Kir4.1 subunit) in mice: phenotypic impact in retina. *J. Neurosci.* **20,** 5733–5740 (2000).

74. Bay, V. & Butt, A. M. Relationship between glial potassium regulation and axon excitability: a role for glial Kir4.1 channels. *Glia* **60,** 651–660 (2012).

75. Kofuji, P. & Connors, N. C. Molecular substrates of potassium spatial buffering in glial cells. *Mol. Neurobiol.* **28,** 195–208 (2003).

76. Bellot-Saez, A., Kékesi, O., Morley, J. W. & Buskila, Y. Astrocytic modulation of neuronal excitability through K+ spatial buffering. *Neurosci. Biobehav. Rev.* **77,** 87–97 (2017).

77. Pasti, L., Volterra, A., Pozzan, T. & Carmignoto, G. Intracellular calcium oscillations in astrocytes: a highly plastic, bidirectional form of communication between neurons and astrocytes in situ. *J. Neurosci.* **17,** 7817–7830 (1997).

78. Newman, E. A. & Zahs, K. R. Modulation of neuronal activity by glial cells in the retina. *J. Neurosci.* **18,** 4022–4028 (1998).

79. Angulo, M. C., Kozlov, A. S., Charpak, S. & Audinat, E. Glutamate released from glial cells synchronizes neuronal activity in the hippocampus. *J. Neurosci.* **24,** 6920–6927 (2004).

80. Pascual, O. *et al.* Astrocytic purinergic signaling coordinates synaptic networks. *Science* **310,** 113–116 (2005).

81. Mothet, J.-P. *et al.* Glutamate receptor activation triggers a calcium-dependent and SNARE protein-dependent release of the gliotransmitter D-serine. *Proc. Natl. Acad. Sci. USA* **102,** 5606–5611 (2005).

82. Mehta, B., Begum, G., Joshi, N. B. & Joshi, P. G. Nitric oxide-mediated modulation of synaptic activity by astrocytic P2Y receptors. *J. Gen. Physiol.* **132,** 339–349 (2008).

83. Stella, N., Tencé, M., Glowinski, J. & Prémont, J. Glutamate-evoked release of arachidonic acid from mouse brain astrocytes. *J. Neurosci.* **14,** 568–575 (1994).

84. Halassa, M. M. & Haydon, P. G. Integrated brain circuits: astrocytic networks modulate neuronal activity and behavior. *Annu. Rev. Physiol.* **72,** 335–355 (2010).

85. Guerra-Gomes, S., Sousa, N., Pinto, L. & Oliveira, J. F. Functional roles of astrocyte calcium elevations: from synapses to behavior. *Front. Cell Neurosci.* **11,** 427 (2017).

86. Poskanzer, K. E. & Yuste, R. Astrocytic regulation of cortical UP states. *Proc. Natl. Acad. Sci. USA* **108,** 18453–18458 (2011).

87. Poskanzer, K. E. & Yuste, R. Astrocytes regulate cortical state switching in vivo. *Proc. Natl. Acad. Sci. USA* **113,** E2675–84 (2016).

88. Halassa, M. M. *et al.* Astrocytic modulation of sleep homeostasis and cognitive consequences of sleep loss. *Neuron* **61,** 213–219 (2009).

89. Fellin, T. *et al.* Endogenous nonneuronal modulators of synaptic transmission control cortical slow oscillations in vivo. *Proc. Natl. Acad. Sci. USA* **106,** 15037–15042 (2009).

90. Stobart, J. L. *et al.* Cortical circuit activity evokes rapid astrocyte calcium signals on a similar timescale to neurons. *Neuron* **98,** 726–735.e4 (2018).

91. Sonoda, K., Matsui, T., Bito, H. & Ohki, K. Astrocytes in the mouse visual cortex reliably respond to visual stimulation. *Biochem. Biophys. Res. Commun.* **505,** 1216–1222 (2018).

92. Slezak, M. *et al.* Distinct Mechanisms for Visual and Motor-Related Astrocyte Responses in Mouse Visual Cortex. *Curr. Biol.* **29,** 3120–3127.e5 (2019).

93. Lines, J., Martin, E. D., Kofuji, P., Aguilar, J. & Araque, A. Astrocytes modulate sensory-evoked neuronal network activity. *Nat. Commun.* **11,** 3689 (2020).

94. Mederos, S. *et al.* GABAergic signaling to astrocytes in the prefrontal cortex sustains goal-directed behaviors. *Nat. Neurosci.* **24,** 82–92 (2021).

95. Bazargani, N. & Attwell, D. Amines, astrocytes, and arousal. *Neuron* **94,** 228–231 (2017).

96. Wahis, J. & Holt, M. G. Astrocytes, Noradrenaline, α1-Adrenoreceptors, and Neuromodulation: Evidence and Unanswered Questions. *Front. Cell Neurosci.* **15,** 645691 (2021).

97. Pacholko, A. G., Wotton, C. A. & Bekar, L. K. Astrocytes-The Ultimate Effectors of Long-Range Neuromodulatory Networks? *Front. Cell Neurosci.* **14,** 581075 (2020).

98. Ma, Z., Stork, T., Bergles, D. E. & Freeman, M. R. Neuromodulators signal through astrocytes to alter neural circuit activity and behaviour. *Nature* **539,** 428–432 (2016).

99. Mu, Y. *et al.* Glia Accumulate Evidence that Actions Are Futile and Suppress Unsuccessful Behavior. *Cell* **178,** 27–43.e19 (2019).

100. Kohro, Y. *et al.* Spinal astrocytes in superficial laminae gate brainstem descending control of mechanosensory hypersensitivity. *Nat. Neurosci.* **23,** 1376–1387 (2020).

NE LINKS ASTROCYTIC ACTIVITY TO REGULATION OF CORTICAL STATE

1.1 Abstract

Cortical state, defined by population-level neuronal activity patterns, determines sensory perception. While arousal-associated neuromodulators—including norepinephrine (NE)—reduce cortical synchrony, how the cortex resynchronizes remains unknown. Furthermore, general mechanisms regulating cortical synchrony in the wake state are poorly understood. Using in vivo imaging and electrophysiology in mouse visual cortex, we describe a critical role for cortical astrocytes in circuit resynchronization. We characterize astrocytes' calcium responses to changes in behavioral arousal and NE, and show that astrocytes signal when arousal-driven neuronal activity is reduced and bi-hemispheric cortical synchrony is increased. Using in vivo pharmacology, we uncover a paradoxical, synchronizing response to Adra1a receptor stimulation. We reconcile these results by demonstrating that astrocyte-specific deletion of Adra1a enhances arousal-driven neuronal activity, while impairing arousal-related cortical synchrony. Our findings demonstrate that astrocytic NE signaling acts as a distinct neuromodulatory pathway, regulating cortical state and linking arousal-associated desynchrony to cortical circuit resynchronization.

1.2 Introduction

Patterns of neural activity in the awake cortex are variable[1]. They range from states of highly synchronized neuronal activity during periods of low arousal, to states of -desynchronized activity during high arousal periods with behavioral activity such as

whisking[2] and running[3]. These different cortical states can be identified both by the correlation between individual neurons[4], and in the overall pattern of cortical electrophysiological activity: synchronized cortical states display greater low-frequency (LF) oscillations and reduced high-frequency (HF) oscillations than desynchronized cortical states[5]. While HF oscillations are important for processing of incoming information[6], LF oscillations during the wake state are less well characterized and have recently been of particular interest in the field. Generally described within a 2–10Hz range[2,7–10], wakeful LF power differs substantively from patterns of cortical activity during sleep[2], indicating a unique role for synchronized cortical states in awake animals. Previous work strongly suggests that one role of awake cortical synchrony is to modulate sensory responses to external stimuli. Increased LF power is associated with reduced neuronal gain[7] and broader tuning[11] in sensory cortex, as well as diminished behavioral performance on sensory perception tasks[3,8,11].

Substantial work has gone into defining the mechanisms by which cortical state is regulated, and in particular, how the cortex becomes sensitized to external stimuli. One central mechanism is the release of NE from the LC, which regulates a primary hallmark of behavioral arousal—pupil diameter[12,13]—and alters the firing properties of cortical neurons[14], leading to desynchronized cortical activity[15]. However, while the desynchronizing effects of NE have been investigated for many years[16], mechanisms that increase waking synchrony have not been well studied[17]. A full understanding of the mechanisms that regulate awake cortical synchrony will be necessary to explain fluctuations in perception and behavior.

Neurons are not the only NE-responsive cells in the cortex; many other cell types sense NE[18–21]. Astrocytes, a non-neuronal cell type abundant throughout the cortex, respond to high levels of NE with robust calcium (Ca^{2+}) signaling[22–28]. However, on the circuit level, astrocyte Ca^{2+} has been linked to cortical state regulation when NE signaling is low, including during sleep[29–31] and under anesthesia[32,33]. In this work, we aimed to resolve the disparity between these two lines of inquiry: both an astrocytic role in sleep generation, as well as their activation by desynchronizing stimuli such as movement. We hypothesized that NE-specific astrocytic signaling might act as a counterintuitive mechanism to regulate the amount of NE-driven cortical desynchrony, and to restore cortical synchrony after changes in arousal.

Here we use *in vivo*, two-photon (2P) Ca^{2+} imaging to show that astrocytes in mouse visual cortex proportionally respond to changes in arousal, rather than the absolute level, positioning astrocytes as a feedback mechanism to increases in arousal. We find that astrocytes respond to changes in NE specifically, with proportional and temporally specific Ca^{2+} signaling. This was true even with small changes in NE, and in the absence of locomotion. This NE-driven astrocyte Ca^{2+} signaling occurs alongside reductions in arousal-associated neuronal activity. Using *in vivo* recordings of local field potential (LFP), we further show that arousal-driven astrocyte Ca^{2+} activity during wake occurs at transitions from cortical desynchrony to synchrony, and that this relationship is dependent on NE signaling. Pharmacological stimulation of Adra1a receptors counterintuitively increases wakeful cortical synchrony, and astrocyte-specific removal of Adra1a enhances total and arousal-driven neuronal activity, while impairing arousal-related cortical synchrony. Our results link astrocytic NE receptors directly to regulation

of cortical state. We identify NE signaling to astrocytes as a new circuit mechanism in which astrocytes act as sensors of NE changes, and subsequently synchronize the cortex in response to changes in arousal.

1.3 Results

Astrocyte Ca^{2+} correlates with relative increases in pupil diameter

To determine whether astrocyte Ca^{2+} activity is dynamically modulated by arousal, we carried out *in vivo*, 2P Ca^{2+} imaging in visual cortex of awake, head-fixed mice while simultaneously recording pupil diameter and running speed (Fig. 1a). We expressed the genetically encoded Ca^{2+} indicator GCaMP in cortical astrocytes under the $GfaABC_1D$ promoter using viral injection (Extended Data Fig. 1a). To identify astrocyte Ca^{2+} activity, we took advantage of our recently developed Astrocyte Quantitative Analysis (AQuA) toolkit[34] that enables us to accurately capture dynamic fluorescent astrocyte signals in an unbiased manner, even from events that are spatially overlapping (Extended Data Fig. 1a–b).

We first extracted fluorescence traces from all AQuA-detected Ca^{2+} events to examine how astrocyte Ca^{2+} varies with arousal. Consistent with previous reports, we found that periods of locomotion were accompanied by large increases in astrocyte Ca^{2+} activity[22,24,35] as well as large increases in arousal[7,8], as reported by increased pupil diameter (Fig. 1b, left). We also observed that even during stationary periods, astrocyte Ca^{2+} activity was accompanied by concurrent and proportional fluctuations in arousal (Fig. 1b, right). To quantify this relationship, we calculated the correlation between average astrocyte Ca^{2+} and either running speed or pupil diameter over the entire recording, and found that for all mice (n = 6 mice), population astrocyte Ca^{2+}

activity was positively correlated with pupil diameter. The average correlation between astrocyte Ca^{2+} and pupil diameter (0.51 ± 0.09) was higher than that of astrocyte Ca^{2+} and running speed (0.21 ± 0.07) when comparing across mice (Fig. 1c, top) or using hierarchical bootstrapping (HB, Fig. 1c, bottom, Methods). In addition, individual astrocyte Ca^{2+} events were more strongly correlated with arousal compared with either speed- or time-shuffled data (Extended Data Fig. 1c, left). Most of these individual Ca^{2+} events (9597/11674, 82.2%) exhibited a signal cross-correlation with pupil diameter within ten seconds and a short (0.32 ± 0.01s S.E.M) lag, consistent with arousal driving astrocyte activity (Extended Data Fig. 1c, right).

Our first analysis indicated that arousal contributes to astrocyte Ca^{2+} beyond its association with movement. However, both absolute pupil diameter[36] and relative changes in pupil diameter[37] can reflect changes in cortical activity. To investigate whether astrocytes sense absolute levels of arousal, we looked at the relationship between average GCaMP fluorescence and pupil diameter. We binned the pupil diameter into ten deciles (Fig. 1d, left), then calculated the average Ca^{2+} fluorescence in each bin, to analyze the effect of arousal level independent of temporal structure. We saw that astrocyte Ca^{2+} dynamically varied with pupil diameter only when the pupil was ~40–80% of maximum diameter (Fig. 1d, right; Supplementary Table 1). This range matched the overlap in pupil diameter found between stationary and movement periods (Extended Data Fig. 1d), indicating this relationship was a function of movement, and suggesting that absolute pupil diameter did not adequately explain the relationship between arousal and astrocyte Ca^{2+}.

To confirm this finding, and to test whether relative changes in pupil diameter were linked to astrocyte Ca^{2+} responses, we calculated an event-triggered average relative to the start of movement. As expected, we found that both astrocyte Ca^{2+} and pupil diameter increased around movement onset, with a short delay between the onset of pupil dilation and the increase in astrocyte Ca^{2+} (Fig. 1e). We then asked whether the level of movement-evoked astrocyte Ca^{2+} activity could be explained by either the absolute level or relative change in movement speed and pupil diameter (Fig. 1f–h). We found that speed was a poor predictor of the maximal astrocyte Ca^{2+} fluorescence (Fig. 1f, left) as previously reported[24], as was the relative change in speed (Fig. 1f, right). In addition, absolute pupil diameter following movement had a weak correlation with astrocyte Ca^{2} fluorescence, indicating that even during behavioral state changes, pupil diameter is a poor predictor of astrocyte responses (Fig. 1g, left). In contrast, the relative change in pupil diameter explains a substantial portion of the astrocyte Ca^{2+} response to movement, indicating that astrocytes are specifically sensitive to relative changes in arousal (Fig. 1g, right).

To support this finding, we next sought to dissociate the effects of movement and arousal on astrocytes by separating behavioral state periods (Extended Data Fig. 1e) and focusing exclusively on stationary periods with increases in arousal. The relationship between astrocyte Ca^{2+} and increases in pupil diameter persisted during stationary periods (Fig. 1i), demonstrating that astrocytes are sensitive to changes in arousal on a smaller scale than previously recognized. Changes in pupil diameter were smaller during stationary periods (Extended Data Fig. 1f), but still predictive of changes in astrocyte Ca^{2+} (Fig. 1j).

The above analyses identified relative changes in arousal as a key driver of both movement-associated and spontaneous fluctuations in astrocyte Ca^{2+} activity. We next wondered whether this relationship might also explain the timing of astrocyte Ca^{2+} activity. We noticed that although astrocyte Ca^{2+} events occurred throughout increases in arousal, the fluorescence often peaked with pupil diameter around movement offset (Fig. 1k). We found that the time from movement onset to the maximum pupil diameter was strongly correlated with the time to peak astrocyte activity (Fig. 1l). Both were also dependent on the duration of the movement bout (Extended Data Fig. 1g). This finding was not solely related to movement. When examining all astrocyte Ca^{2+} events, onsets occurred more often during dilation and offsets occurred more often during constriction, indicating arousal-associated astrocyte Ca^{2+} is tailored to the duration as well as the magnitude of arousal (Fig. 1m). These findings indicate that changes in arousal shape the timing and level of astrocyte Ca^{2+} activity.

Phasic increases in norepinephrine precede astrocyte Ca^{2+} across behavioral states

NE is a key driver of both changes in pupil diameter and arousal-associated changes in the brain[38]. While recent work has suggested that astrocytes preferentially respond via Ca^{2+} to “multi-peaked” NE axonal activity[23], the impact of behavioral state has not yet been considered. In light of the sensitive relationship between arousal and astrocyte Ca^{2+} (Fig. 1), we wondered whether NE was also linked to small changes in astrocyte Ca^{2+} during stationary periods, in addition to large movement-evoked changes in astrocyte Ca^{2+}. This finding would suggest cortical astrocytes play a broader role in arousal-associated changes than previously recognized.

To determine the relationship between NE and astrocyte Ca^{2+} activity, we simultaneously expressed a fluorescent sensor of NE, $GRAB_{NE}$[39], in cortical neurons under the h-syn promoter and the genetically encoded Ca^{2+} indicator jRGECO1b in cortical astrocytes under the $GfaABC_1D$ promoter (Fig. 2a). We simultaneously imaged these sensors using 950nm and 1040nm excitation, and were able to clearly resolve astrocyte Ca^{2+} and extracellular NE (Fig. 2a, Supplementary Video 1). Examining the raw fluorescence of the $GRAB_{NE}$ signal, we saw that in addition to the expected increases in fluorescence, many parts in the imaging field-of-view displayed reductions in fluorescence that closely matched changes in the size and fluorescence of background vasculature. This was independent of the average region brightness or standard deviation (Extended Data Fig. 2a). To ensure that our analysis accurately reflected NE levels, and not background vascular dynamics, we developed a method to compensate for hemodynamic signals in 2P imaging (Extended Data Fig. 2b, Methods). To further ensure limited hemodynamic contamination, we took the mean of the corrected $GRAB_{NE}$ signal, excluding highly contaminated or artifactual pixels, which resulted in a corrected signal that preserved fluctuations in $GRAB_{NE}$ signal (Extended Data Fig. 2c). This corrected $GRAB_{NE}$ signal showed little correlation with vasculature or regions that had highly hemodynamically contaminated signals ($r < 0.2$), but correlated well with regions that had active $GRAB_{NE}$ signal (Extended Data Fig. 2d). To further validate our methodology in an unbiased manner, we looked at how individual pixels recording $GRAB_{NE}$ fluorescence correlated with pupil diameter, and grouped these pixels into bins based on their correlation with pupil diameter (Extended Data Fig. 2e). We found that our corrected $GRAB_{NE}$ linearly correlated with pixels that match changes

with pupil diameter, suggesting our method reflects $GRAB_{NE}$ signal that occurs from pupil-related increases in NE, and not areas of the imaging field that show dimming in response to pupil dilation, like vasculature (Extended Data Fig. 2f).

Using our corrected $GRAB_{NE}$ signal, we found that $GRAB_{NE}$ fluorescence matched changes in pupil diameter and astrocyte Ca^{2+} activity, although the $GRAB_{NE}$ showed a slow decay, similar to previous reports[23] (Fig. 2b, left). This relationship persisted even during stationary periods (Fig. 2b, right). The slow NE decay was reflected by the $GRAB_{NE}$ power spectrum, which showed an inverse relationship with frequency (Fig. 2c). Slow (0.01–0.03Hz) $GRAB_{NE}$ fluctuations had more power than the empirically fit 1/f relationship, suggesting long-lasting fluctuations in “tonic” NE predominate the $GRAB_{NE}$ signal.

To confirm the link between $GRAB_{NE}$ and arousal, we examined the cross-correlation between pupil diameter and $GRAB_{NE}$. We found a positive correlation between $GRAB_{NE}$ and spontaneous changes in pupil diameter ($r = 0.13$, Fig. 2d), similar to that previously described for cortical NE axons[40]. However, the maximum cross-correlation was broad and continued for at least 20s after the pupil diameter, reflecting the persistence of extracellular NE (Fig. 2d, left). Further, unlike what has been reported for NE axons[40], $GRAB_{NE}$ showed poor cross-correlation ($r = 0.04$) with the derivative of pupil diameter (Fig. 2d, right) and the overall correlation between $GRAB_{NE}$ and pupil diameter was significantly higher than for pupil diameter derivative (Fig. 2e). These results suggest that cortical $GRAB_{NE}$ dynamics best report arousal level rather than changes in arousal, and may substantively differ from the activity pattern of the underlying NE axons.

We next quantified the relationship between $GRAB_{NE}$ and astrocyte Ca^{2+} activity. We found a positive, broad correlation (r = 0.17) between the two, similar to that found between pupil diameter and $GRAB_{NE}$ (Fig. 2f, left). The average delay (-5.7s ± 3.1s) between $GRAB_{NE}$ and astrocyte Ca^{2+} indicated that changes in NE preceded changes in astrocyte Ca^{2+} (Fig. 2f, right). The $GRAB_{NE}$ correlation was not significantly different between pupil diameter and astrocyte Ca^{2+} (Fig. 2g), suggesting $GRAB_{NE}$ is similarly linked to arousal and astrocyte Ca^{2+}.

Although slow NE fluctuations predominated our $GRAB_{NE}$ signal (Fig. 2c), we also noticed short phasic increases in NE (Fig. 2h, left, triangles). We wondered whether these phasic increases were a primary driver of astrocyte Ca^{2+}. We segregated phasic NE peaks by their amplitude (Fig. 2h, left, triangles), and saw that larger phasic $GRAB_{NE}$ activity was also longer lasting (Fig. 2h, right; Supplementary Table 2). We then examined how astrocyte Ca^{2+} changed following phasic NE activity. We saw that large (≥2 std) phasic changes in NE preceded prolonged increases in astrocyte Ca^{2+} that scaled with the amplitude of the $GRAB_{NE}$ signal (Fig. 2i–j, left; Supplementary Table 3, left). Phasic $GRAB_{NE}$ activity also co-occurred with small increases in astrocyte Ca^{2+} that were proportional to the $GRAB_{NE}$ amplitude (Fig. 2i, right). These increases were observed even with smaller (1 std) changes in NE (Fig. 2j, right; Supplementary Table 3, right). These results suggest astrocytes dynamically respond to phasic changes in NE, in both the duration and amplitude of their Ca^{2+} signaling.

While these results showed that phasic NE preceded increases in astrocyte Ca^{2+}, they did not indicate whether this held true across behavioral states. In addition, this analysis only looked at peaks in $GRAB_{NE}$ signaling which varied in width, so the temporal

relationship between NE and astrocyte Ca^{2+} was hard to determine. To expand our analysis, we calculated the event-triggered average around the onset of astrocyte Ca^{2+} events. We confirmed that astrocyte Ca^{2+} was preceded by increases in NE, which peaked shortly after astrocyte Ca^{2+} signaling had begun (Fig. 2k). This relationship was true for both astrocyte Ca^{2+} events that occurred during movement (Fig.2k, left), and during stationary periods (Fig. 2k, right). In sum, these results indicate that astrocytes are sensitive to changes in NE across behavioral states.

Arousal-driven astrocyte Ca^{2+} is positioned to counteract increases in arousal-associated neuronal activity

Although we observed spontaneous arousal-related changes in astrocyte Ca^{2+}, arousal also strongly modulates ongoing neuronal activity[7,37,41]. Since astrocytes respond to neuronal activity[42–44], we wondered how arousal-mediated changes in nearby neurons might be related to astrocyte Ca^{2+} activity. To answer this, we expressed hSyn-GCaMP6f in neurons and GfaABC$_1$D-jRGECO1b in astrocytes to record the Ca^{2+} activity of both cellular populations simultaneously (Fig. 3a and Supplementary Video 2). This method generated widespread, spatially overlapping expression in astrocytes and neurons *in vivo* (Fig. 3b). Although there was a small amount of GCaMP bleed-through into the red channel (Fig. 3b, yellow arrow), neurons and astrocytes were easily distinguishable based on both emission wavelength and morphology, and the majority of neurons appeared as holes in the astrocyte syncytium (Fig. 3b, white arrow). To further ensure that neuronal activity was not misidentified as an astrocyte event, we also

delineated regions of likely spectral cross-talk and did not pick events from these regions (Methods).

We found that astrocyte Ca^{2+} and neuronal activity often spontaneously fluctuated together, along with movement and arousal/pupil diameter (Fig. 3c). The average fluorescence traces of neurons and astrocytes were maximally correlated when there was no time-shift, a relationship enhanced during movement (Fig. 3d, black, r = 0.46 ± 0.06) compared to stationary periods (Fig. 3d, grey, r = 0.34 ± 0.04). We next wanted to investigate how astrocyte Ca^{2+} relates to arousal-driven neuronal activity specifically. To do this, we used principal component (PC) analysis to identify the major axes of variance in the neuronal activity, and then identified the PC most correlated with arousal (arousal PC) [41,45]. We found that the arousal PC of neuronal activity (Fig. 3e, top, red line) often better matched the pupil diameter (Fig. 3e, top, light grey) than the mean neuronal activity (Fig. 3e, top, dark grey). This was likely due to the variability in neuronal responses to arousal, which could be seen when plotting neuronal activity and sorting by their arousal PC weight (Fig. 3e, bottom), with the arousal PC capturing differential neuronal responses to arousal[41]. This was particularly obvious during large increases in arousal such as movement onset (Fig. 3e, bottom, red dashed lines).

In agreement with previous work[41], we found that the arousal PC was usually PC1 (Fig. 3f, grey, 28/35 recordings). Furthermore, when cross-correlating with pupil diameter, we found that average astrocyte Ca^{2+} activity (Fig. 3g, left, magenta) was better correlated with pupil diameter than average neuronal Ca^{2+} activity (Fig. 3f, left, grey), but that this relationship was reversed when cross-correlating using the arousal PC of astrocyte (Fig. 3g, right, magenta) and neuronal (Fig. 3g, right, grey) activity instead. This was evident

when comparing across recordings, with the arousal PC consistently reflecting arousal-associated neuronal activity better than using mean fluorescence (Fig. 3h, grey dots). In contrast, arousal-associated astrocyte Ca^{2+} activity was poorly represented when using an astrocyte arousal PC and better represented by taking the mean fluorescence activity alone (Fig. 3h, magenta dots). These results suggest that astrocytes and neurons differentially respond to arousal. Astrocytic responses to arousal are best characterized by a consistent increase in activity which can be captured by taking the mean of the population activity, while the neuronal response to arousal is best captured by describing the variability in neuronal activity using PC analysis.

We next looked at how astrocyte Ca^{2+} and arousal-driven neuronal activity changed with increases in arousal. We found that with both movement (Fig. 3i, top) and stationary increases in pupil diameter (Fig. 3i, bottom), arousal-associated neuronal activity (Fig. 3i, grey) increased alongside increases in astrocyte Ca^{2+} (Fig. 3i, magenta). We also saw that the large increases in astrocyte Ca^{2+} occurred with arousal-associated neuronal activity and peaked when the neuronal activity began to diminish (Fig. 3i). To investigate this further, we looked at how the neuronal arousal PC changed relative to astrocyte Ca^{2+} activity. Taking the average neuronal activity around the onset of all astrocyte Ca^{2+} events (Fig. 3j, top left), we found that astrocyte Ca^{2+} events tended to occur at the peak of arousal-associated neuronal activity, right before a reduction in the neuronal arousal PC. Using the first derivative of the neuronal PC (Fig. 3j, bottom left), we saw a clear relationship with astrocyte Ca^{2+} occurring at a transition point between increasing and decreasing arousal-associated neuronal activity. This relationship was not only movement-associated, but also could be seen when looking

only at astrocyte Ca^{2+} events during stationary periods (Fig. 3j, right). These results indicate that while neuronal responses to arousal occur alongside astrocyte responses, astrocyte activity occurs at the crux of increasing-to-decreasing arousal-related neuronal activity, and is positioned to counteract the effects of arousal on the local neuronal population.

These results also raise the possibility that astrocyte Ca^{2+} may be a response to changes in local arousal-associated neuronal activity, rather than arousal or NE *per se*. To better understand and dissect the effects of neuronal activity and arousal on astrocyte Ca^{2+} we used machine learning via Random Forest Regression to predict astrocyte Ca^{2+} (Extended Data Fig. 3). Using this strategy, we could explain ~85% of the variance in astrocyte Ca^{2+} fluorescence (Extended Data Fig. 3a, left). Permutation-based feature importance analysis indicated that pupil diameter was the most important predictor of astrocyte Ca^{2+}, and a substantially better predictor than the next most important factor, local neuronal Ca^{2+} fluorescence (Extended Data Fig. 3a, right). When using the neuronal arousal PC data, we found that the model was still able to predict astrocyte Ca^{2+} well, explaining ~85% of the variance in astrocyte Ca^{2+} fluorescence (Extended Data Fig. 3b, left). Using feature analysis, we found that while pupil diameter was still the best predictor of astrocyte Ca^{2+}, it had less relative importance, consistent with our intentional isolation of neuronal activity that most correlated to arousal and thus providing redundant information to the model. (Extended Data Fig. 3b, right). We interpret these results as evidence that while astrocytes are responsive to local neuronal activity, they are sensitive to arousal beyond the influence of nearby neurons.

Dampening local neuronal activity does not eliminate arousal-driven astrocyte Ca^{2+}

Our dual-color imaging approach showed that astrocyte Ca^{2+} activity occurs around reductions in the arousal-associated activity of nearby neurons, and our Random Forest Regression analysis suggested that nearby neurons are not the main drivers of astrocyte Ca^{2+}. However, these experiments did not answer whether astrocytes were sensing changes in neuronal activity and responding to this activity rather than to changes in arousal *per se*. To determine whether arousal or local neuronal activity was the major driver of arousal-associated astrocyte Ca^{2+}, we expressed hM4Di, an inhibitory Gi-coupled Designer Receptor Exclusively Activated by Designer Drugs (DREADDs) [46] in neurons, as well as GCaMP6f in astrocytes to image Ca^{2+} (Fig. 4a). We found no difference in the average frequency of astrocyte Ca^{2+} events from baseline following administration of either the hM4Di agonist CNO or saline, although the overall variability increased (Fig. 4b, resampled distributions from each condition, Methods). We next asked whether astrocyte Ca^{2+} responded differently to large increases in arousal due to movement (Fig. 4c), and found that there was no difference in the magnitude of astrocyte Ca^{2+} responses with either saline or CNO administration (Fig. 4d, Supplementary Table 4). This finding extended to small increases in arousal during stationary periods as well, and we saw no difference in arousal-associated astrocyte Ca^{2+} except at a high CNO concentration (5 mg/kg), where we recorded an enhancement of arousal-associated Ca^{2+} (Fig. 4e–f, Supplementary Table 5). These results indicate that local neuronal activity is not necessary for astrocyte Ca^{2+} responses to arousal, and further suggest that astrocytes may be more sensitive to NE input when the activity level of nearby neurons is low. These data

support the idea that astrocytes also monitor and reflect the state of local circuit activity when directly responding to changes in arousal.

NE ties astrocyte Ca^{2+} to changes in cortical state

In Figure 3, we showed that astrocyte Ca^{2+} events occur before reductions in arousal-associated neuronal activity. We wondered, however, whether the relationship we described between astrocyte Ca^{2+} and neuronal activity was only true for nearby neurons, or if it extended to the broader cortical circuit. To answer this question, in a subset of our mice expressing Ca^{2+} indicators in neurons (hysn-GCaMP6f) and astrocytes (GFAP-jRGECO1b), we implanted low-impedance electrodes into the ipsilateral cortex near the imaging window, and into the contralateral cortex (Fig. 5a). Using this methodology, we recorded the LFP (Fig. 5b, top), which in contrast to our spatially restricted Ca^{2+} imaging window, reflects the integrated electrical inputs and activity of the visual cortex and surrounding brain regions as a whole[47]. In these LFP recordings, we could observe spontaneous transitions between cortical states dominated by LF power (2–7 Hz; running-evoked 7–10 Hz was excluded) and those dominated by high frequency (HF, 70–100 Hz) power, indicative of synchronous and desynchronized cortical states respectively (Fig. 5b) [1]. We noticed that when mice transitioned to a low-arousal state following movement, astrocyte Ca^{2+} peaked as LF power increased (Fig. 5c, left) and HF power decreased (Fig. 5c, right).

To further investigate this relationship, we asked how astrocyte Ca^{2+} cross-correlated with LFP power, and changes in LFP power indicated by the derivative, and compared this with neuronal Ca^{2+} activity. We found that astrocyte cross-correlations with LFP

power were right-shifted from the equivalent neuronal cross-correlations (Fig. 5d–e). When looking at LF power specifically (Fig 5d, left, magenta), we found that astrocyte Ca^{2+} was negatively correlated at negative lags, and positively correlated with LF power at positive lags, indicating astrocyte Ca^{2+} preceded increases in LF power (Fig 5d, left, magenta). In contrast, neuronal Ca^{2+} was only significantly positively correlated with LF power when there was no lag (Fig. 5d, left, grey), indicating that LF power and neuronal population activity are coordinated. These findings were confirmed when examining the derivative of LF power. We found that changes in LF power were maximally correlated with astrocyte activity without any lag (Fig. 5d, right, magenta), while neuronal activity was maximally correlated when LF power change came before neuronal activity (Fig. 5d, right, grey). Our results demonstrate that while neuronal Ca^{2+} is correlated with LF power, astrocyte Ca^{2+} is correlated with changes in LF power.

We found a similar relationship among HF power and neuronal and astrocyte Ca^{2+} activity, although inverted about the y-axis. Both cell types were positively correlated with HF power when HF power preceded neuronal and astrocyte Ca^{2+}, and neurons were negatively correlated with HF power with no lag, while astrocytes were negatively correlated when HF power followed astrocyte Ca^{2+} (Fig. 5e, left). In addition, both astrocyte and neuronal Ca^{2+} were negatively correlated with the derivative of HF power, but for neurons this correlation only held true when changes in HF power preceded neuronal Ca^{2+}, while for astrocytes this relationship was true both when HF power preceded or had no lag with astrocyte Ca^{2+} (Fig. 5e, right). These results indicate that while HF power precedes both neuronal and astrocyte Ca^{2+}, neuronal Ca^{2+} is inversely related to absolute HF power while astrocyte Ca^{2+} is inversely related to changes in HF

power. Overall, this analysis demonstrates that arousal-associated fluctuations in local neuronal Ca^{2+} activity are reflected by absolute LFP power, while astrocyte Ca^{2+} is instead tied to changes in LFP power.

We next sought to determine whether astrocyte Ca^{2+} was tied to changes in LFP power solely during large changes in arousal due to movement, or if this was a property of arousal-driven astrocyte Ca^{2+} more generally. To answer this question, we computed an event-triggered spectrogram, and considered how LFP power varied before and after all astrocyte Ca^{2+} events (Fig. 5f). We found that astrocyte Ca^{2+} signaling occurred at the crux of a transition from a HF-dominated cortical state to one dominated by LF power. This was reflected in an increase in LF power, and decrease in HF power, following astrocyte Ca^{2+} events (Fig. 5f, right). This relationship was also seen in the LFP power of the contralateral cortex (Fig. 5g), indicating that astrocyte Ca^{2+} is tied to the transition of neuronal activity from a high to low-arousal state not just at a local level (Fig. 3j), and at the level of the nearby cortex (Fig. 5f), but also to bi-hemispheric changes in cortical state.

Since we earlier identified changes in arousal and NE as major drivers of spontaneous changes in astrocyte Ca^{2+} (Fig. 1 and 2), we hypothesized that NE was necessary for the link between astrocyte Ca^{2+} and cortical state transitions. In particular, we hypothesized that Adra1 receptors might underlie this relationship due to their importance for astrocyte physiology[22,24,28,48]. We pharmacologically blocked Adra1 receptors using the antagonist Prazosin (5mg/kg, i.p.) and found that the relationship between astrocytes and cortical state was reduced (Fig. 5h–i), confirming that NE signaling links astrocyte Ca^{2+} to cortical state changes.

Enrichment of Adra1a receptors in visual cortex astrocytes

Our pharmacological blockade using Prazosin (Fig 5h-i) indicated that the connection between astrocyte Ca^{2+} and cortical state was dependent on signaling through Adra1 receptors. However, our experiments could not determine which Adra1 receptors were most likely to underlie the connection between astrocytes and cortical state, nor whether there was spatial or laminar specificity of receptor expression which could indicate preferential involvement in the regulation of cortical state. To answer these questions, we analyzed a previously published dataset which profiled the ribosome-associated mRNA expression of astrocytes in the mouse visual cortex[49]. We looked at adrenergic receptor expression in the adult (P120) dataset and confirmed astrocytic expression of most adrenergic receptors, although astrocytes showed little Adra2b, Adrab2, and Adra3b in this dataset (Extended Data Fig. 4a, left). When analyzing the astrocytic expression of adrenergic receptors relative to an input control, the relative expression of Adra1a was higher than that of the other adrenergic receptors, indicating that Adra1a may be preferentially enriched in visual cortex astrocytes compared to other cell types (Extended Data Fig. 4a, right).

To confirm astrocytic expression of the Adra1a receptor, as well as its laminar specificity, we used spatial transcriptomics to assess the expression of Adra1a, as well as Adra1b and Adra2a (Extended Data Fig. 4b). Using LaST map single-molecule *in situ* hybridization (smFISH) [50], we were able to see the mRNA expression of each of these receptors, which showed striking heterogeneity throughout the brain (Extended Data Fig. 4b, left). All three receptors we profiled showed cortical expression in

astrocytes, as delineated by expression of the astrocyte-specific mRNA SlcA3 (GLAST), as well as in non-astrocytic cell-types (Extended Data Fig. 4b, right). We quantified mRNA spots per astrocyte in the visual cortex for each of these receptors, and found higher expression at deep layers of cortex (Extended Data Fig. 4c). This was particularly true for Adra2a and Adra1b receptors, while Adra1a receptors also showed higher expression in intermediate layers of cortex (Extended Data Fig. 4c), where the effects of cortical synchrony are particularly important for perception[51].

Astrocyte Adra1a receptor signaling shapes neuronal activity

Based on pharmacological and transcriptomic data, we identified Adra1a as an astrocytic adrenergic receptor with the appropriate spatial and laminar distribution to have a role connecting astrocytes and cortical state. This receptor subtype has also been implicated previously in astrocytic activation in other contexts[23–25,52,53]. To test how Adra1a receptors modulated cortical activity, we activated Adra1a receptors by injecting (I.P.) the specific Adra1a agonist A61603 (10mg/kg.)—which stimulates astrocytes in acute cortical slices[48]—while recording cortical astrocyte and neuron Ca^{2+} activity (Fig. 6a). We saw robust responses in both astrocytes and neurons within minutes of A61603 administration (Fig. 6b). Specific stimulation of Adra1a receptors led to astrocyte Ca^{2+} that was more homogenous (Fig. 6c) than before injection, with an overall increase as shown by the z-scored change in fluorescence (Fig. 6d, left). In contrast, neuronal Ca^{2+} showed a general reduction in baseline Ca^{2+} (z-scored change in normalized fluorescence, Fig. 6d, right), while also exhibiting similar oscillatory activity as astrocytes. To better quantify these neuronal changes, we took the power spectra of

each neuron and separated the activity into power occurring from slower (> 0.05Hz, Fig. 6e, left) and faster fluctuations (< 0.05Hz, Fig. 6f, left). We found that after A61603 administration, there was more power in > 0.05Hz fluctuations (Fig. 6e, right) and less power in > 0.05Hz fluctuations (Fig. 6f, right). Our results indicate that A61603 administration, while increasing the coordination and level of Ca^{2+} activity in astrocytes, broadly leads to inhibition of neuronal activity and shapes the overall pattern of neuronal activity.

Next, to determine how astrocytic Adra1a receptors specifically altered cortical neuronal activity, we generated a new mouse line with LoxP sites flanking the Adra1a gene, allowing for Cre-specific deletion of the receptor (Extended Data Fig. 5). By injecting an astrocyte-specific Cre-GFP virus into the cortex of $Adra1a^{fl/fl}$ mice (or wild-type littermate controls), we removed Adra1a receptors from astrocytes and performed neuronal Ca^{2+} imaging while recording locomotion and pupillometry (Fig. 6g). In agreement with previous work[54], we found that this strategy resulted in robust, astrocyte-specific Cre expression which colocalized with the astrocytic marker S100β, but not the neuronal marker NeuN (Extended Data Fig. 6). Overall activity in these mice showed more neuronal Ca^{2+} events (Fig. 6h), as well as less power in < 0.05 Hz Ca^{2+} fluctuations (Fig. 6i) and more power in < 0.05Hz Ca^{2+} fluctuations (Fig. 6j). These results are inverse to the effects we observed when stimulating Adra1a receptors using A61603, suggesting NE-signaling through astrocyte Adra1a receptors is a major pathway for both dampening neuronal activity and shaping the pattern of neuronal activity. To ensure these results were not an artifact of imaging rate, we recorded neuronal activity

using resonant galvanometers for a 7.5Hz effective frame rate, and saw the same results (Extended Data Fig. 7).

We next determined whether astrocyte Adra1a receptors impacted arousal-related neuronal activity. As before (Fig. 3i), we assessed how arousal-related neuronal activity changed either with movement (Fig. 6k) or stationary pupil dilation (Fig. 6l). In both cases, mice lacking astrocyte Adra1a receptors displayed enhanced arousal-related neuronal activity compared to wild-type littermate controls (Fig. 6k–l). In this dataset, the distribution of durations during movement bouts (Extended Data Fig. 8a) and stationary pupil dilations (Extended Data Fig. 8b) was wide, and differed between Adra1a$^{fl/fl}$ mice and wild-type controls. To account for this, we only analyzed arousal-related neuronal activity during the movement (Extended Data Fig. 8b) or pupil dilation event (Extended Data Fig. 8c), including a ~1s offset to account for a delayed response in neuronal activity. Using this analysis, we saw increased arousal-related neuronal activity in Adra1a$^{fl/fl}$ mice compared to wild-type littermate control mice following both movement related (Fig. 6k) and stationary (Fig. 6l) increases in arousal. These results suggest that NE-signaling through astrocyte Adra1a receptors regulates and dampens arousal-associated neuronal activity. Finally, an explanation for the increased response of neurons to arousal in Adra1a$^{fl/fl}$ mice might be a stronger connection to arousal overall. To test this, we looked at the cross-correlation between arousal-related neuronal activity and pupil diameter (Fig. 6m, top), and found that Adra1a$^{fl/fl}$ mice had a lower correlation between pupil diameter and arousal-associated neuronal activity than their wild-type littermates (Fig. 6m, bottom). These results indicate that not only does signaling through astrocyte Adra1a receptors affect the magnitude of the neuronal response to arousal,

but it is also important for shaping the pattern of neuronal activity to best match changes in arousal.

NE signaling through astrocyte Adra1a receptors modulates cortical state

Based on the Adra1a dependent relationship between astrocytes and cortical state, we hypothesized that, in contrast to the desynchronizing effect of NE on the cortex generally[55], signaling through astrocytic Adra1a receptors would lead to cortical synchrony. To examine the effect of stimulating the Adra1a receptor on cortical synchrony, we again injected the specific agonist A61603 (1mg/kg, i.p.)—while recording cortical LFP (Fig. 7a). Compared to saline control, A61603 treatment resulted in high-amplitude fluctuations in the LFP (Fig. 7b) which was reflected by increased power at lower frequencies in the spectrogram (Fig. 7c). To quantify this, we specifically examined LF power (2–7Hz), which increased following astrocyte Ca^{2+} (Fig. 5), and saw a significant increase compared to controls (Fig. 7d). In contrast, we saw no significant difference in HF power (70–100Hz, Fig. 7e), which we found to change prior to astrocyte Ca^{2+} (Fig. 5). These results indicate that contrary to the role of NE more broadly[15], specific stimulation of Adra1a receptors results in increased cortical synchrony.

While our experiments with A61603 suggested a synchronizing effect of stimulating Adra1a receptors, our manipulation was body-wide due to I.P. injection and could affect all Adra1a-expressing cells. However, our Ca^{2+} imaging results (Fig. 6 g–m) in $Adra1A^{fl/fl}$ mice indicated that NE signaling to astrocytic Adra1a might modulate changes in cortical state. To test this, we again injected an astrocyte-specific Cre-GFP

virus into the cortex of Adra1a$^{fl/fl}$ mice (or wild-type littermate controls) to remove the Adra1a receptor from astrocytes, and recorded cortical LFP (Fig. 7f). In Adra1a$^{fl/fl}$ mice, the cortical LFP was generally higher amplitude than in controls (Fig. 7g). This was evident in the LFP power spectra, in which Adra1a$^{fl/fl}$ mice showed higher power across all frequency bands compared to wild-type mice (Fig. 7h, left), and higher total LFP power on average (Fig. 7h, right).

In agreement with previous results (Fig. 6h), this LFP spectral analysis indicates that NE signaling to astrocytes modulates overall cortical neuronal activity. We hypothesized that there might be specific effects of removing astrocytic Adra1a receptors at NE-related cortical state transitions, where astrocytes preferentially signal in response to NE (Fig. 1k; Fig. 5c). We focused on times when mice stopped moving, and found a substantial difference between the median normalized spectrograms for Adra1a$^{fl/fl}$ and wild-type mice (Fig. 7i, top row). Compared to wild-type mice, Adra1a$^{fl/fl}$ mice had increased HF power during movement (Fig. 7i, middle row). This enhancement was seen both when looking at all movement offsets in the entire cohort (Fig. 7j, left), and on average between the two cohorts of mice (Fig. 7j, right). In contrast, following movement, there was less LF power in the Adra1a$^{fl/fl}$ mice compared to wild-type mice (Fig. 7i, bottom row). This dampened LF power was also evident both in the pooled movement-offsets (Fig. 7k, left), and on average between Adra1a$^{fl/fl}$ and wild-type mice (Fig. 7k, right). Taken together, these data show that selectively removing a NE receptor from astrocytes alters arousal-related cortical state changes, enhancing the desynchronizing effects of arousal and reducing the ability of the cortex to subsequently resynchronize afterwards.

1.4 Discussion

Understanding awake cortical state regulation is crucial for understanding perception, attention, and behavior[1]. Most research examining wake cortical states has focused on arousal mechanisms—such as release of NE—that desynchronize the cortex and lead to increased sensitivity to external stimuli[7,8,37,56]. However, we found that NE (Fig. 8, green) not only desynchronizes cortical neuronal activity, but also leads to cortical synchrony by activating astrocytic Adra1a receptors. This model places astrocytes in a central role for awake cortical state regulation, acting as a negative feedback mechanism for arousal-associated desynchrony (Fig. 8).

A new mechanism for regulating arousal-associated cortical circuit activity and state changes

We found that astrocytes responded to arousal broadly (Fig.1), and to NE specifically, more sensitively than previously recognized[22–25] (Fig. 2). This arousal-associated Ca^{2+} activity occurred at the crux of both reductions in arousal-associated neuronal activity (Fig. 3) and bi-hemispheric cortical state changes (Fig. 5), and occurred even when impairing local neuronal activity (Fig. 4). These results suggest NE signaling directly to astrocytes acts as a separate neuromodulatory pathway. Furthermore, we identified a causal link in NE signaling through the Adra1a receptor on astrocytes to the regulation of neuronal activity overall (Fig. 6h–j), the response of neurons to arousal specifically (Fig. 6k–m), and to the modulation of arousal-associated cortical state transitions (Fig. 7f–k). Importantly, rather than being sensitive to arousal *per se*, we identify that astrocytes specifically detect relative changes in arousal, providing them with the potential to specifically act as a feedback mechanism without working against the

arousal system more generally. This role may be particularly useful in the context of heterogenous cortical NE dynamics we described here: by assessing extracellular fluctuations in NE[39], we observed signaling on a time scale of seconds, similar to the reported activity patterns of the underlying locus coeruleus axons[40], as well as much slower signaling on the order of tens of seconds to minutes (Fig. 2c). Thus, change-detection may allow astrocytes to ignore the tonic fluctuations of cortical NE in order to sensitively respond to phasic increases in NE.

Arousal-associated astrocyte Ca^{2+} is poised to regulate arousal-associated neuronal activity

Of course, astrocytes are not the sole detectors of cortical NE. Neurons, among other cell types[18–21], also show strong responses to arousal[3,8,9,37] and NE[14]. Understanding the relative effects of arousal on neuronal and astrocytic activity is crucial to understand how these cellular populations contribute to arousal-mediated cortical state changes. Our results are particularly significant in the context of previous research placing astrocyte Ca^{2+} responses downstream of neuronal activity, or to driving changes in neuronal activity on long timescales[42–44,48,57,58]. In contrast, our data show that arousal-associated astrocyte Ca^{2+} signaling occurs at the crux of the neuronal response to arousal, co-occurring with transitions in arousal-associated neuronal activity (Fig. 3). This relationship was also seen more broadly, with astrocyte Ca^{2+} occurring when bi-hemispheric arousal-associated desynchronized electrical activity reduced and cortical synchrony increased (Fig. 5). Furthermore, we found that NE-specific astrocyte Ca^{2+} signaling, and its relationship to arousal, was not dependent on the activity of nearby

neurons, suggesting that astrocytes can act directly downstream of neuromodulatory signaling to modulate neuronal activity (Fig. 4). These findings support a model in which astrocytes dynamically respond to NE to modulate neuronal activity on the physiological timescales, i.e., seconds, of arousal.

Receptor subtype-specific relationships between NE and cortical state

Our work not only positions cortical astrocytes as drivers of neuronal synchrony on multiple scales in the wake state, but also expands current understanding of the role of NE in cortical state regulation. In contrast to the generally desynchronizing role of NE[59], we found that specific pharmacological stimulation of the Adra1a receptor leads to reduced cortical neuronal activity (Fig. 6d, right) and alters the pattern of cortical neuronal activity (Fig. 6e–f). Adra1a receptor stimulation also led to increases in cortical synchrony without altering HF power (Fig. 7a–d). This perhaps counterintuitive relationship was initially hypothesized by early pharmacological work[60], but to our knowledge has not been validated nor widely accepted in the field. Our findings here suggest that that even within the same family, activation of different NE-receptor subtypes may have profoundly different effects on cortical state regulation and by extension arousal, attention, and behavior. This may provide a basis for understanding the disparate effects of adrenergic receptors on perception and cognition[61–63].

What is arousal?

In this study, we used pupil diameter as an external read-out for a complicated set of underlying biological processes that work in tandem, and influence neural activity in a variety of brain regions[64–68]. While we focused on NE specifically, many neuromodulators including acetylcholine[40,69,70] and serotonin[71,72] vary with arousal and are known to modulate cortical state. Understanding how these additional neuromodulatory inputs affect astrocyte and neuronal activity will be vital for a complete description of cortical state regulation in awake animals. Additionally, while our work establishes a strong role for astrocytes in mediating arousal-associated changes in neuronal activity and cortical state, we did not directly link these changes to behavioral outcomes. Future studies should focus on how arousal-associated astrocyte Ca^{2+} influences the general perceptual effects of arousal[8] and extend these findings to the specific effects of attention[73,74]. It will also be important to examine how external stimuli-driven[33,75,76] and arousal-driven astrocyte Ca^{2+} signaling lead to changes in behaviorally relevant neuronal population activity and cortical synchrony.

How do sub-populations of astrocytes and neurons respond to arousal?

To expand the impact of our findings, the experiments we have described here could be extended to dissect the role of specific subpopulations of neurons and astrocytes, or types of Ca^{2+} activity in these populations. In this work, we analyzed Ca^{2+} imaging data as homogenous cellular populations, in part due to an acquisition frame rate (~2Hz) which was necessary for imaging astrocyte populations on a wider scale (0.5mm^2). However, there may be differences between the population-level Ca^{2+} activity we identified and fast Ca^{2+} responses to arousal.

Both astrocytes[24,50,77] and neurons[78] can be split into multiple sub-populations, and neuronal subtypes—in particular inhibitory interneuron subtypes—have unique relationships to arousal and cortical state[79]. In our work, we used PC analysis to account for heterogenous neuronal responses to arousal, and we found Adra1a-mediated astrocytic modulation of neuronal responses to arousal. However, we did not identify the particular effect of our manipulations on neuronal subtypes. Based on the overall reduction of neuronal activity with A61603 injection (Fig. 6d, right), and the overall increase in neuronal activity (Fig. 6h) and LFP power with knockout of astrocytic-Adra1a receptors (Fig. 7h), our work suggests astrocytic modulation of cortical inhibition is a likely candidate for the downstream circuit mechanisms controlling cortical state, as has been proposed in other contexts[53]. Cortical interneurons have been shown both to play a critical role in the control of cortical state[70,80–85], and to be particularly sensitive to their electrostatic extracellular environment[86]. Neuromodulator-driven astrocytic control of the extracellular environment[87] and inhibitory control of nearby neurons[27] may act as prime loci of control for cortical circuit activity and state.

In addition, within our smFISH dataset (Extended Data Fig. 4) as well as in published single-cell data[88], cortical astrocytes show variable expression of neuromodulatory receptors, and some astrocytes lack any transcripts for Adra1a at all. This suggests molecularly distinct, and potentially functionally distinct, subpopulations of cortical astrocytes with differential sensitivity and responses to arousal-related neuromodulators. It also suggests that gap junctions, ATP signaling, and other mechanisms[89–92] that create networks within the astrocyte syncytium may be particularly important for arousal-associated astrocyte activity and modulation of cortical circuits.

Identifying the specific relationships among subpopulations of astrocytes and neurons, and determining which are modulated by arousal and in what manner, will be important for understanding what constitutes a cortical circuit and how cortical circuit activity is regulated. Furthermore, much like the effects of arousal, these relationships may be layer-specific[51], and likely differ across cortical areas[93]. Future study of cellular sub-population-specific effects on cortical state, particularly in additional cortical regions and in combination with behavioral assessments, will provide a richer appreciation of the cellular mechanisms that regulate cortical state in response to arousal.

1.5 Methods

Animals

All procedures were carried out in accordance with protocols approved by the University of California, San Francisco Institutional Animal Care and Use Committee. Animals were housed and maintained in a temperature-controlled environment on a 12-h light–dark cycle, with *ad libitum* food and water. All imaging/electrophysiology experiments were performed at the same time each day. Adult C57BL/6 mice, Adra1a$^{fl/fl}$ mice, or Adra1a wild-type mice aged 1–6 months at time of surgery were used. For experiments involving Adra1a $^{fl/fl}$ mice, the experimenter was blind to animal genotype before surgery, recording, and analysis.

Generation of Adra1a$^{fl/fl}$ mice

The Mouse Biology Program at the University of California, Davis, constructed the mouse. A floxed FLAG-α1A knock-in vector was made using standard methods as follows: The targeting vector contained a 5’ arm of 5.4 kb and a 3’ arm of 5.5 kb. Lox P sites were placed upstream and downstream of the α1A-AR gene first coding exon. A Kozak sequence and single FLAG tag were upstream, and the neomycin-resistance gene was downstream.

The vector was electroporated into the C57BL/6N ES cell line JM8.F6. The resulting ES cell clones were screened by long range PCR for loss of the native allele and homologous recombination, and containing a single copy of the plasmid by LoxP PCR. Two clones passed these screens and had normal chromosome counts. Both ES clones were microinjected into blastocysts, and transferred to e2.5 stage pseudo pregnant recipients. The resulting chimeras were screened for percent ES cell derived coat color, and those greater than 50% were mated to C57BL/6N females. Germline heterozygous mice were produced, and mated to MMRRC strain C57BL/6-Tg(CAG-Flpo)1Afst/Mmucd, RRID: MMRRC:036512-UCD, for excision of the Neo selection cassette. Neo-excised mice were identified via PCR, and mated further to C57BL/6J mice to remove the FLP transgene. Mice were continued in C57BL/6J.

Routine PCR genotyping used 5’-gcttcctcaggctcacgtttcc and 3’-gccttagaaatgttcacctgtgc primers upstream and downstream of the LoxP site (Extended Data Fig. 5). These mice are available upon request from corresponding author.

Surgical procedures and viral infection

Mice were administered dexamethasone (5mg/kg, s.c.) at least 1 hour prior to surgery, and anesthetized using 1.5% isoflurane (Patterson Veterinary Supply, 78908115). After hair removal and three alternating swabs of 70% ethanol (Thermo Fisher Scientific, 04-355-720) and Betadine (Thermo Fisher Scientific, NC9850318), a custom-made titanium headplate was attached to the skull using cyanoacrylate glue and C&B Metabond (Parkell, S380). If recording LFP, 0.5mm burr holes were made bilaterally over the visual cortex, and bilaterally over the cerebellum for reference, and a ~200µm diameter PFA-coated tungsten wire (A-M Systems, 796500) was implanted -0.2mm into each hole and secured with Metabond. For imaging and LFP experiments, a 3mm craniotomy was made over the right visual cortex and the right visual cortex burr hole was made lateral to the craniotomy.

For viral infection, 400–800nL total volume of the following viruses were injected alone, or in combination by premixing the solutions before aspiration: AAV5.GfaABC$_1$D.GCaMP6f.SV40 (Addgene, 52925-AAV5), AAV9.hSyn.NE2h (Vigene, YL10074-AV9), AAV9.GfaABC$_1$D.JRGECO1b (Vigene, custom-ordered), AAV9.Syn.GCaMP6f.WPRE.SV40 (Penn Vector Core, AV-8-PV2822), AAV2.hSYN.hM4D(Gi)-mCherry (Addgene, 50475-AAV2), AAV5.GFAP(0.7).EGFP.T2A.iCre (Vector Biolabs, VB1131).

Injections were made through a glass pipette and UMP3 microsyringe pump (World Precision Instruments) into the right visual cortex at coordinates centered on +2.5mm m/l, +0.5mm a/p, and -0.3 d/v from lambda. After allowing at least ten minutes for viral

diffusion, the pipette was slowly withdrawn and a glass cranial window implanted using a standard protocol[94].

Immunohistochemistry and in situ hybridization

Following *in vivo* experiments mice were overdosed on isoflurane and then perfused transcardially with phosphate buffered saline (PBS, Sigma-Aldrich P3813) followed by 4% paraformaldehyde in PBS (Santa Cruz Biotechnology, CAS 30525-89-4). Brains were removed and postfixed overnight in 4% paraformaldehyde, followed by cryoprotection in 30% sucrose in PBS for two days at 4°C. Brains were snap frozen in dry ice and stored at -80°C until adhesion onto a sectioning block with Optimal Cutting Temperature Compound (Thermo Fisher Scientific, 23-730-571). 40µm coronal sections were taken on a cryostat and stored in cryoprotectant at -20 °C until immunohistochemistry was performed. For immunohistochemistry, free-floating sections spanning the rostral-caudal axis were selected and washed with 1x PBS for five minutes three times on an orbital shaker, followed by permeabilization with 0.01% PBS-Triton X for 30 min. Sections were then blocked with 10% NGS (Sigma-Aldrich, S26-100ML) for 1 hr. Immediately after, sections were incubated with chicken α-GFP (1:3000, Abcam, ab13970) and either rabbit α-NeuN (1:1000, EMD Millipore, ABN78) or mouse α-NeuN (1:1000, Millipore Sigma, MAB377) and rabbit α-S100B (1:500, Millipore Sigma, SAB5500172). Sections were then washed with 1x PBS for five minutes three times on a shaker, followed by secondary incubation with Thermo Fisher Scientific goat α-chicken Alexa Fluor 488 and either goat α-rabbit Alexa Fluor 405 or goat α-mouse Alexa Fluor 405; goat α-rabbit Alexa Fluor 555 for 2 hours at 20°C on a shaker. Sections were

washed again with 1x PBS for five minutes three times, then mounted and cover slipped with Fluoromount-G. For whole section examples, images were taken using a Keyence BZ-X800 fluorescence microscope to assess viral spread. 2x images were acquired and the images computationally stitched with Keyence Analysis Software. For cell counting 60x z-stacks were captured on spinning-disk confocal (Zeiss). Slides were oil-immersed. The Fiji plugin Cell Counter was used to quantify the number of GFP^+, $NeuN^+$, and $GFP^+/NeuN^+$ cells to determine colocalization. Each animal had two sections with each section having six distinct field-of-views containing 20 z-planes. A cell was considered GFP^+ when signal was confined to soma and processes, and $GFP^+/NeuN^+$ when cells exhibited merged signals.

Single-molecule, fluorescent *in situ* hybridization data collection was performed using LaST map smFISH as previously described.[50] Astrocyte cell boundaries were segmented using an ilastik pixel classifier and a customized watershed segmentation. In order to preserve processes of astrocyte and not cut them off from the DAPI signals, a pixel classifier was trained by using only large gaussian filters (5/10 pixels) during the feature extraction step. As a result, astrocyte processes were detected with fewer splits. Pixel classification only carves out non-background pixels from the image and doesn't identify the astrocyte boundaries separating neighboring cells, i.e. instance segmentation. To address this problem, we first used CellPose to identify all nuclei from the image. Subsequently, the centroids of all nuclei were extracted and used as the seeds to generate astrocyte boundaries between adjacent cells using a watershed segmentation. As a result, astrocytes with touching processes were separated. Finally,

non-cell debris might remain in the segmentation image, we thus further used an object classification workflow in ilastik to remove them.

All mRNA signals were detected using a Python package called TrackPy using 5 pixels as diameter and 96 as percentile threshold. These detected spots were then assigned to each astrocyte that they sat within by using a python package called shapely. Due to the tissue damage that occurred during the sample preparation step, only 7 cortex surface areas from all sections were eligible for downstream processing to ensure the comparability between tissue sections. For all these regions, both white matter boundaries and the superficial cortex area were manually annotated. For each cell, the distance to both the white matter boundary (d_WM) and distance to the cortex surface (d_ep) were calculated. The relative cortical depth (D_relaCortex) was thus defined as:

$$D_{relaCortex} = \frac{d_{ep}}{d_{ep} + d_{WM}}$$

Recording setup

Animals were given at least 1 week after surgery for recovery and viral expression. They were then habituated on a custom-made circular running wheel over at least two days, and for a cumulative time of at least 2.5 hours, before experimental recordings began. After habituation, mice were head-fixed on the wheel and movements were recorded by monitoring deflections of colored tabs on the edge of the wheel using an optoswitch (Newark, HOA1877-003).

Pupillometry

Pupil recordings were made using a Genie near-infrared (NIR) camera (1stVision, M640), a telescopic lens (Thorlabs, MVL50TM23), and acquired at 30Hz using the MATLAB Image Acquisition toolbox. A small monitor (Amazon, B06XKLNMW3) showing a consistent teal background color (RGB: 0,1,1) was placed by the mouse to allow for observation of the full range of pupil dynamics in an otherwise dark room. For experiments without imaging, a NIR light (Amazon, B00NFNJ7FS) was used to visualize the pupil.

Two-photon imaging

Two-photon imaging was performed on a microscope (Bruker) with two tunable Ti:sapphire lasers (MaiTai, SpectraPhysics) and a Nikon 16x, 0.8 N.A. water-dipping objective with a 2x-optical zoom (frame rate: 1.7Hz, FOV: 412μm^2, resolution: 512x512 pixels). 950nm excitation light with a 515/30 emission filter was used to image green-emitting fluorophores, and 1040nm light with a 605/15 emission filter was used to image red-emitting fluorophores. Recordings lasted from ten minutes to one hour.

Electrophysiological recordings

Visual cortex LFP was recorded at 1KHz and subtracted from the ipsilateral cerebellar LFP before 1KHz amplification (Warner Instruments, DP-304A) and acquired using PrairieView (Bruker) or PackIO[95].

In vivo pharmacology

Recordings were taken before and after saline, Prazosin-HCl (5mg/kg Sigma-Aldrich, P7791-50MG), A61603(1µg/kg or 10µg/kg, Tocris, 1052), or clozapine N-oxide (CNO, 1mg/kg or 5mg/kg, Tocris, 4936) were injected intraperitonially while animals remained head-fixed on the wheel, to ensure post-treatment recordings were comparable with baseline measures.

Data analysis

All data analysis was done in MATLAB unless otherwise indicated. No statistical methods were used to pre-determine sample sizes, but they are similar to previous reports[22,40]. Boxplots are shown with the central mark indicating the median and the bottom and top edges of the box indicating the 25th and 75th percentiles, respectively. Whiskers extend to the most extreme data point or within 1.5 times the interquartile range from the bottom or top of the box, and all other data are plotted as individual points, as listed in the figure legends. For statistical comparisons, non-parametric tests were used, or where indicated, normality was assumed but not formally tested, and t-tests were used. Hierarchical bootstrapping was performed based on a MATLAB implementation (https://github.com/jenwallace/Hierarchical_bootstrap_Matlab) of the methodology, and used in order to reduce the statistical error rate of comparisons while retaining statistical power[96]. All multiway comparisons were adjusted for using Tukey-Kramer correction. No data was excluded from analyses except for the following (not pre-determined): In hSYN-hM4Di experiments, outliers were excluded across all conditions from small stationary responses to avoid confounding effects from other

influences on astrocyte Ca^{2+}, as described in methods. For *in vivo* pharmacology experiments, electrical artifacts in band power were excluded before analysis, as described in methods. Samples were allocated into experimental groups by cell-type expression of each individual fluorescent sensor. Only adult animals (1–6 months of age) were used in experiments, and both male and female were used and randomly selected. For imaging and electrical recordings of spontaneous activity, blinding was not relevant because cell-type viral expression is evident from expression pattern. For in vivo pharmacology, blinding was not possible because control recordings were taken prior to treatment recordings to avoid confounding the treatment effects. For $Adra1a^{fl/fl}$ mice, the experimenter was blinded to genotype before data collection and analysis.

Speed calculations

To compute wheel speed, a detected break in the optoswitch circuit was determined when the absolute value of the derivative of the raw voltage trace was at least 2 standard deviations above the mean. For recordings with very little movement (std < 0.1), this threshold generated false positives so a set threshold of 0.1 was used. The number of breaks in the optoswitch circuit per second was then calculated, and using the circumference and number of evenly spaced colored tabs at the edge of the wheel, the wheel speed was determined and used for all subsequent analyses using speed. Movement periods were defined by wheel speed ≥ 10 cm/s and movement bouts that were separated by ≤ 2 s were considered one event. To ensure that movement related dynamics were not included in stationary analysis, data was excluded from at least ten seconds around identified movement periods.

Pupillometry

Following acquisition, pupil data was processed through a Python function which used contrast detection to identify the edges of the backlit pupil from the sclera and fit an ellipse whose major radius was taken as the pupil diameter. The diameter was then low-pass filtered to 0.5 Hz and normalized to a range between 0 and 1 to give pupil diameter as percent maximum. The pupil derivate was normalized to the acquisition rate (30Hz) to compute pupil phase and to determine the phase of astrocyte Ca^{2+} events and the cross-correlations with $GRAB_{NE}$. Stationary arousal dilations and constrictions were identified by the sign of the calculated pupil derivative and only changes in pupil diameter > 10% were used for subsequent analyses.

LFP

All spectral analysis was done using Chronux[97]. Raw LFP data was visually inspected to confirm useable signal was present, and then 60 Hz noise was filtered out and drifting baselines were compensated for using linear fitting. LFP power for frequency bands was computed using built-in Chronux functions with a time-bandwidth of 2.5 and two tapers, no frequency padding, and 5 s moving windows. For changes in LFP band power around arousal or astrocyte Ca^{2+} events, the median band-limited power was obtained and then normalized to the median band-limited power in the event-triggered time window to get relative band power. The median power before an event onset vs after was combined for each recording, and for $Adra1a^{fl/fl}$ mice, the ratio between the two was computed and compared to Adra1a wild-type mice. For changes in LFP power

after A61603 administration, the band-limited power for saline and drug data were calculated, outliers were removed to avoid contamination by recording artifacts, and then this power was normalized to the band-limited power for the respective baseline recording.

For total power in Adra1a$^{fl/fl}$ and control mice, no baseline correction was done to avoid skewing the analysis. Spectrum power was calculated by concatenating recordings from all mice of each genotype and computing average or individual spectra with a time-bandwidth of 6 and 8 tapers to increase accuracy. The total power was then computed by summing across all frequency bands. Relative power was computing by dividing the spectrum from each mouse by its total power, and relative band power was computed by summing the power from each frequency band and dividing by the total power.

Ca^{2+} imaging

Astrocyte Ca^{2+} events and fluorescence were extracted using the AQuA software analysis package[34]. For dual-color imaging with neuronal Ca^{2+} indicators, particular care was taken to avoid AQuA detection of neuronal activity; the standard deviation of the neuronal channel was taken in FIJI and a mask was created in AQuA to exclude areas of high neuronal activity and soma from analysis. Astrocyte events were only included if they had an area greater than 10 µm, lasted for at least 2 frames, and had an AQuA p-value < 0.05. To obtain the average astrocyte Ca^{2+} fluorescence, the compensated fluorescence traces which account for spatially overlapping events was taken, normalized to their maximum value, and then averaged together.

Neuronal Ca^{2+} events and fluorescence were extracted from neuropil background semi-automatically using Suite2P[98]. We identified Ca^{2+} events by taking identified spikes in the Ca^{2+} fluorescence data and thresholding them for only the largest (> 3std over the mean) events. To calculate the average neuronal Ca^{2+} fluorescence, the trace from each neuron was normalized to its maximum value and averaged together.

Machine-learning based analysis of input contribution to astrocyte Ca^{2+}

As an alternative to assess the contribution of biological inputs on astrocyte Ca^{2+}, data from dual-color Ca^{2+} imaging was used to train a machine-learning model to predict average Ca^{2+} activity. To include LFP data, the spectrogram data from each LFP recording was decomposed using Principal Component Analysis based on the eigenvectors from the ipsilateral recording that accounted for the largest proportion of the variance. The PC1 in this data corresponded to cortical synchrony, with positive weights for high frequency and negative weights for low frequencies, matching a previous report but with inverse sign[99]. LFP PC1 for ipsilateral and contralateral recordings, as well as speed, pupil diameter, and average Ca^{2+} fluorescence for neurons and astrocytes, was then z-scored and resampled to 10Hz before being concatenated. This dataset was then imported into Python for machine learning analysis using the SciKit-learn toolbox. For analysis, randomly generated data was added for comparison, and rows without both ipsilateral and contralateral LFP recordings were excluded from subsequent analysis. Average astrocyte Ca^{2+} data was used as the target dataset and data was split into training (80%) and testing (20%) before classification using a Random Forest Regression model. The model was validated using

the R^2 between the predicted average astrocyte Ca^{2+} fluorescence from the model and the actual average astrocyte Ca^{2+} data of the test set. Permutation testing of the predictors was then used to determine their relative contributions to model prediction.

$GRAB_{NE}$ Analysis

In $GRAB_{NE}$ imaging data, we observed background fluorescence fluctuations which we thought might arise from hemodynamic artifacts. To ensure the data reflected the NE signal, hemodynamic artifacts in the data were removed by a custom-designed, data processing pipeline. The predominant hemodynamic artifact in the data was assumed to reflect fluctuating hemoglobin levels altering brain absorptivity causing an attenuation of light. As such, the signal from each pixel could be modeled as,

$$Y_k(t) = F_k(t) \cdot e^{-\mu_k(t)X} + N(t) = F_k(t) \cdot e^{h_k(t)} + N(t)$$

where k is index of pixel, $Y_k(t)$ and $F_k(t)$ are, respectively, the observed curve and the real fluorescence of kth pixel, $\mu_k(t)$ is the absorption coefficient for kth pixel, X is the path distance, the term $e^{h_k(t)}$ represents the intensity attenuation, and N(t) is the noise. In our data, the identified hemodynamic signal across pixels was approximately synchronous, but varied in magnitude, thus the attenuation of one pixel can be represented by another, that is $e^{h_j(t)} = e^{ah_k(t)+b}$ $(j \neq k)$. Based on the findings above, we designed the following pipeline:

1. We selected one connected vascular region with minimal fluorescence in the average projection of the data and calculated an initial vascular reference curve. This region was assumed to have the lowest possibility to contain any true $GRAB_{NE}$ signal.

2. To avoid compensating for slow changes in the true $GRAB_{NE}$ signal, we subtracted the curve of each pixel by a 100-frame moving average.

3. We applied linear regression and fit the logarithm of the processed curve to the initial vascular reference curve. The exponential of the fit data was then taken to represent the hemodynamic effect for each pixel. To account for cases where the initial reference curve was contaminated, we iteratively refined the reference curve before fitting, that is, we calculated the weighted average of the original curve for all pixels (fitting parameter a in $e^{ah_k(t)+b}$ for each pixel is considered as the weight) and subtracted its moving average.

4. We removed the hemodynamic artifact (if any) by dividing the raw pixel curve by the exponential of the fitting data, $F_k(t) \approx \frac{Y_k(t)}{e^{h_k(t)}}$.

Next, only the least (1–25%) hemodynamically affected pixels with the lowest *a* were taken, excluding the bottom 1% which often contained artifacts, and these were averaged together and used as the final $GRAB_{NE}$ signal. For spectral analysis, each recording was concatenated together in ten-minute segments, padding with its median value if necessary, and then run in Chronux with no frequency padding, a time-bandwidth of three, five tapers, and passing frequencies above half the window size ($3e^{-3}$Hz) and less than the Nyquist frequency (0.9Hz). To identify phasic increases in the $GRAB_{NE}$ signal built-in MATLAB functions were used to determine local peaks in the signal and a prominence threshold was used to determine the different magnitudes of $GRAB_{NE}$ increases.

Event triggered-averages

All averages were computed by identifying events (e.g., movement offset, pupil dilation, etc.) and taking data in a symmetric time window around the events. The data is subsequently plotted as the mean and standard error across all events, except for spectrograms where the median was used.

Correlations

For comparisons of maximum and change in astrocyte Ca^{2+}/pupil/speed after arousal, values were computed for each trace separately and then linearly correlated with p-values describing the probability of a true R^2 relationship between each two metrics. For correlations between astrocyte and neuronal Ca^{2+} activity, the average population fluorescence was taken for each and z-scored before cross-correlation. For behavioral state-separated cross-correlations, the same procedure applied, but only z-scored data from either moving periods, or stationary periods, was used. For correlations within neuronal and astrocyte populations, the pairwise correlation between each cell (neurons) or event (astrocytes) was computed, the symmetric and autocorrelations were excluded, and the overall mean was taken to obtain a single value indicating the synchrony of Ca^{2+} dynamics within each cellular population. For cross-correlations between pupil and imaging data ($GRAB_{NE}$ and astrocyte Ca^{2+}) all data was z-scored, resampled to either 10 or 30Hz, padded with nan values if unequal in length, and then cross-correlated. For cross-correlations between LFP band power and Ca^{2+} imaging data, all data was z-scored, averaged, and then resampled to 2Hz to match the LFP resolution before cross-correlation.

hSYN-hM4Di

To estimate the effect of CNO on astrocyte Ca^{2+}, the average Ca^{2+} event properties and overall event rate for each recording were randomly sampled 10^4 times and CNO data was subtracted from corresponding baseline data. This procedure generated the range of treatment effects possible from the sampled data, and a p-value was calculated as the proportion of CNO difference from baseline that were less than the maximum, or greater than the minimum, difference found in saline conditions. For calculating the modulation of astrocyte Ca^{2+} responses to arousal, the absolute change in average astrocyte Ca^{2+} fluorescence after either movement onset or pupil dilation was determined. Outliers during small stationary responses which might reflect the influence of other variables on astrocyte Ca^{2+}, were excluded. The magnitude of astrocyte Ca^{2+} responses to arousal after treatment was then compared to baseline responses.

Neuronal arousal PC analysis

PCA was done using the built-in MATLAB function on z-scored neuronal Ca^{2+} data. The pupil diameter and PC data was then resampled to an effective rate of 10Hz, and the Pearson's correlation between the pupil diameter and each PC was used to identify the arousal PC for each recording This PC was then normalized to the maximum value before subsequent analysis.

For comparisons between wild-type and $Adra1a^{fl/fl}$ mice, the response to each movement onset or stationary pupil dilation was normalized to the median value in the window, and then the average arousal PC value during the event period was taken with a 2-frame offset to account for a slight lag in the arousal-associated neuronal response.

1.6 Figures

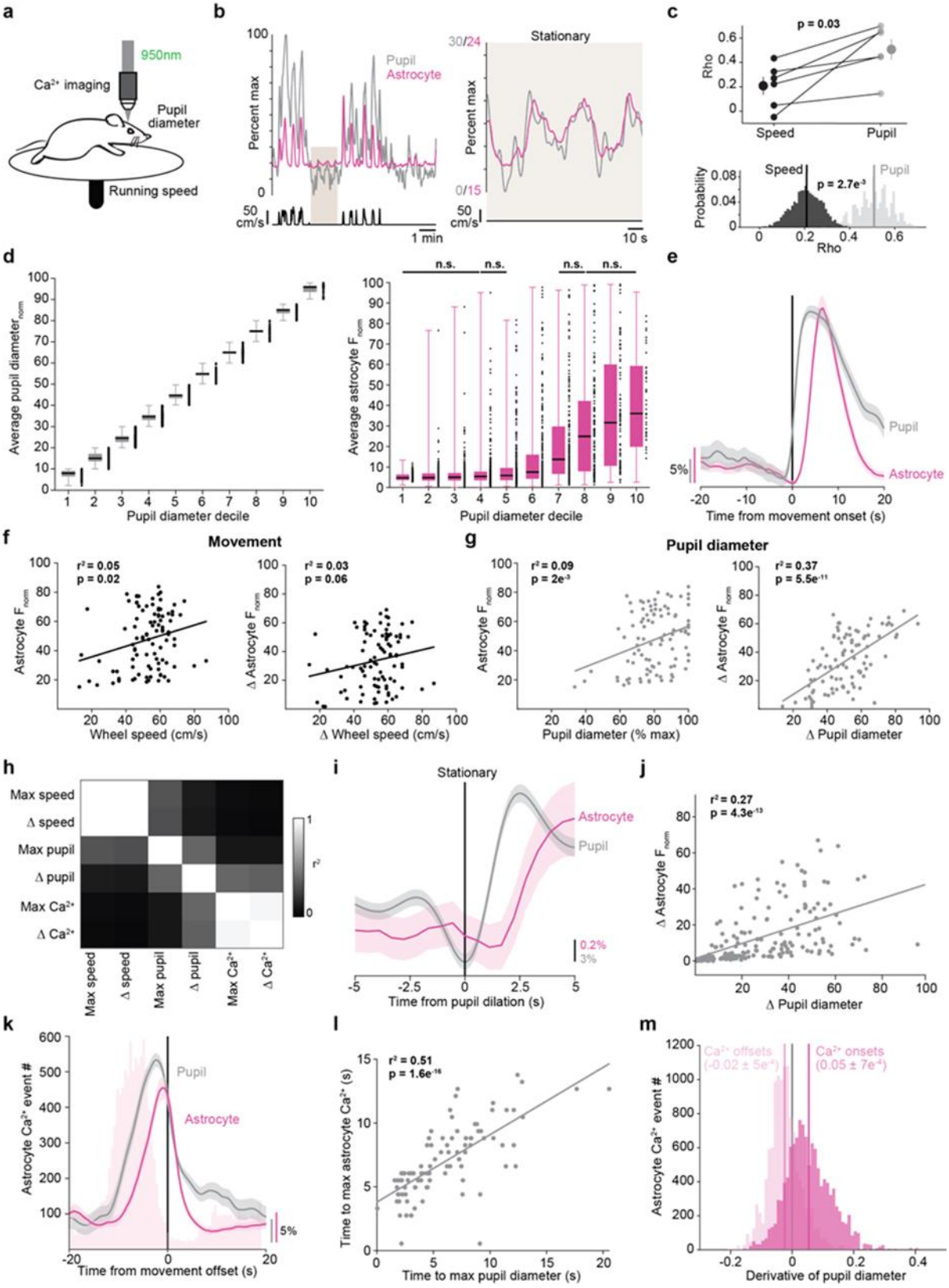
a
950nm
Ca²⁺ imaging
Pupil diameter
Running speed
b
Pupil
Astrocyte
Percent max
Stationary
30/24
0/15
50 cm/s
1 min
10 s
c
p = 0.03
Rho
Speed
Pupil
Probability
p = 2.7e⁻³
d
Average pupil diameter norm
Pupil diameter decile
Average astrocyte F norm
n.s.
e
Pupil
Astrocyte
5%
Time from movement onset (s)
f
Movement
r² = 0.05
p = 0.02
r² = 0.03
p = 0.06
Astrocyte F norm
Δ Astrocyte F norm
Wheel speed (cm/s)
Δ Wheel speed (cm/s)
g
Pupil diameter
r² = 0.09
p = 2e⁻³
r² = 0.37
p = 5.5e⁻¹¹
Pupil diameter (% max)
Δ Pupil diameter
h
Max speed
Δ speed
Max pupil
Δ pupil
Max Ca²⁺
Δ Ca²⁺
r²
i
Stationary
Astrocyte
Pupil
0.2%
3%
Time from pupil dilation (s)
j
r² = 0.27
p = 4.3e⁻¹³
k
Astrocyte Ca²⁺ event #
Pupil
Astrocyte
5%
Time from movement offset (s)
l
r² = 0.51
p = 1.6e⁻¹⁶
Time to max astrocyte Ca²⁺ (s)
Time to max pupil diameter (s)
m
Ca²⁺ offsets (-0.02 ± 5e⁻⁴)
Ca²⁺ onsets (0.05 ± 7e⁻⁴)
Derivative of pupil diameter

Figure 1. Changes in arousal shape astrocyte Ca^{2+} activity independent of locomotion.
(a) Experimental setup. **(b)** Representative astrocyte Ca^{2+} (magenta), pupil diameter (grey), and wheel speed (black) show that these measures are closely related (left), even during stationary periods (right, smoothed with a 5-frame window). **(c)** Astrocyte Ca^{2+} correlates better with pupil diameter than speed when comparing across mice (top, two-sided signed-rank test) or using hierarchical bootstrapping (HB) of recordings (n = 6 mice). Values of n are applied throughout the figure. **(d)** Left: Separating pupil diameter based on size. Right: Astrocyte Ca^{2+} was not different within low or high pupil sizes (n = 3206 time-bins, One-sided Kruskal-Wallis test, $p > 0.05$ indicated as n.s., Supplementary Table 1. Boxplot shows median and IQR. Whiskers extend to the most extreme data points). **(e)** Astrocyte Ca^{2+} and pupil diameter dynamics aligned to mouse movement onset at t = 0 (n = 104 movement onsets). **(f–g)** Linear regression (trend lines) of astrocyte Ca^{2+} and either wheel speed or pupil diameter, after movement onset (n = 104 movement onsets, two-sided t-test). **(f)** Neither maximum wheel speed (left) nor changes in wheel speed (right) correlate well with astrocyte Ca^{2+} responses. **(g)** Maximum pupil diameter (left) predicts astrocyte Ca^{2+} less strongly than changes in pupil diameter (right). **(h)** Heat-map of r^2 values between the variables in f–g. **(i)** Astrocyte Ca^{2+} response to pupil dilation during stationary periods (n = 188 stationary dilations). **(j)** Changes in stationary pupil diameter correlate with astrocyte Ca^{2+} (n = 188 stationary dilations, two-sided t-test). **(k)** Astrocyte Ca^{2+} events (light pink bars) begin before movement offset, but average astrocyte Ca^{2+} fluorescence (magenta trace) peaks with pupil diameter at the end of movement (n = 104 movement offsets). **(l)** The latency to maximum astrocyte Ca^{2+} and pupil diameter after movement onset (n = 104 movement bouts, two-sided t-test) are correlated. **(m)** Astrocyte Ca^{2+} events (n = $1.17e^4$ astrocyte Ca^{2+} events) begin (dark pink) with pupil dilation (i.e., when pupil derivative is positive) and end (light pink) with constriction (negative pupil derivative). Data is presented as mean ± S.E.M unless otherwise noted.

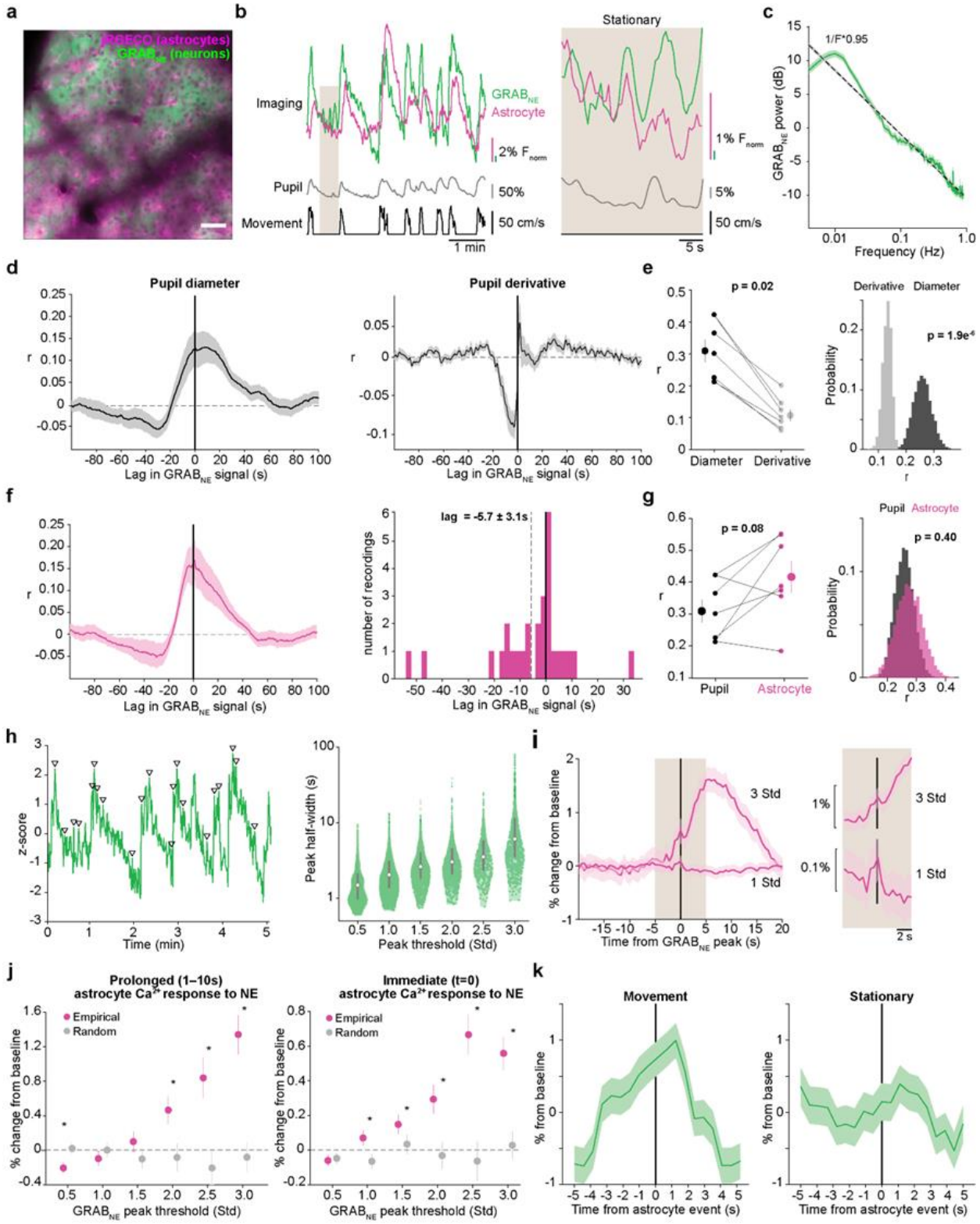
a
jRGECO (astrocytes)
GRAB$_{NE}$ (neurons)
b
Imaging
GRAB$_{NE}$
Astrocyte
2% F$_{norm}$
Pupil
50%
Movement
50 cm/s
1 min
Stationary
1% F$_{norm}$
5%
50 cm/s
5 s
c
1/F^0.95
GRAB$_{NE}$ power (dB)
Frequency (Hz)
d
Pupil diameter
Pupil derivative
r
Lag in GRAB$_{NE}$ signal (s)
e
p = 0.02
Diameter
Derivative
Derivative Diameter
p = 1.9e^{-6}
Probability
f
number of recordings
lag = -5.7 ± 3.1s
g
p = 0.08
Pupil
Astrocyte
Pupil Astrocyte
p = 0.40
h
z-score
Time (min)
Peak half-width (s)
Peak threshold (Std)
i
% change from baseline
3 Std
1 Std
Time from GRAB$_{NE}$ peak (s)
1%
0.1%
2 s
j
Prolonged (1–10s)
astrocyte Ca^{2+} response to NE
Immediate (t=0)
astrocyte Ca^{2+} response to NE
Empirical
Random
GRAB$_{NE}$ peak threshold (Std)
k
Movement
Stationary
% from baseline
Time from astrocyte event (s)

Figure 2. Astrocytes are sensitive to a range of NE increases.
(a) *In vivo* 2P image showing dual-color expression of neuronal $GRAB_{NE}$ and astrocyte jRGECO1b. Scale bar = 50µm. n = 28 recordings from 7 mice throughout figure. **(b)** Representative traces smoothed with a 5-frame window. Astrocyte Ca^{2+} (magenta), $GRAB_{NE}$ (green), pupil diameter (grey), and wheel speed (black) show a close relationship over the course of minutes (left), and over the course of seconds during stationary periods (right). **(c)** The power spectrum of $GRAB_{NE}$ dynamics shows an inverse relationship with frequency ($F^{-0.95}$, dotted line) and increased power in slow fluctuations (period > 30 s, mean with jackknifed error bars). **(d)** $GRAB_{NE}$ positively correlates with pupil diameter (left), but not the derivative of pupil diameter (right). **(e)** $GRAB_{NE}$ is more strongly correlated with pupil diameter than pupil derivative across mice (left, two-sided signed-rank test) and across recordings (HB). **(f)** Left: astrocyte Ca^{2+} activity positively correlates with $GRAB_{NE}$ activity. Right: Astrocyte Ca^{2+} activity follows changes in $GRAB_{NE}$. **(g)** No difference was found between the $GRAB_{NE}$ correlation with astrocytes compared to pupil diameter across mice (left, $p = 0.08$, two-sided signed-rank test) or across recordings (HB). **(h)** Left: phasic increases in $GRAB_{NE}$ signal, with arrowheads marking a subset of peaks. Right: Larger increases in $GRAB_{NE}$ had longer durations ($p < 0.05$ for all bins, One-sided Kruskal-Wallis test, n and p-values listed in Supplementary Table 2. Boxplot shows median and IQR). **(i)** Example astrocyte Ca^{2+} traces separated by $GRAB_{NE}$ peak amplitude. Left: astrocyte Ca^{2+} activity showed large and persistent responses to large increases (e.g., 3 std) in $GRAB_{NE}$. Right (shaded area = 5s before and after t = 0): both large and small (e.g., 1 std) changes in $GRAB_{NE}$ drove small transient increases in astrocyte Ca^{2+}. **(j)** Left: Astrocyte Ca^{2+} persistently increased after large (≥ 2std) increases in $GRAB_{NE}$, and scaled with $GRAB_{NE}$ amplitude (* = $p < 0.05$, two-sided rank-sum test, n and p-values listed in Supplementary Table 3). Right: Astrocyte Ca^{2+} showed proportional, time-locked responses to even small changes (≥ 1 std) in $GRAB_{NE}$ (* = $p < 0.05$. rank-sum test, see Supplementary Table 3 for details). **(k)** $GRAB_{NE}$ activity around astrocyte Ca^{2+} onsets at t = 0s (n = $1.2e^4$ events) shows increased extracellular NE before astrocyte Ca^{2+} events in both movement and stationary periods. Data are presented as mean ± S.E.M.

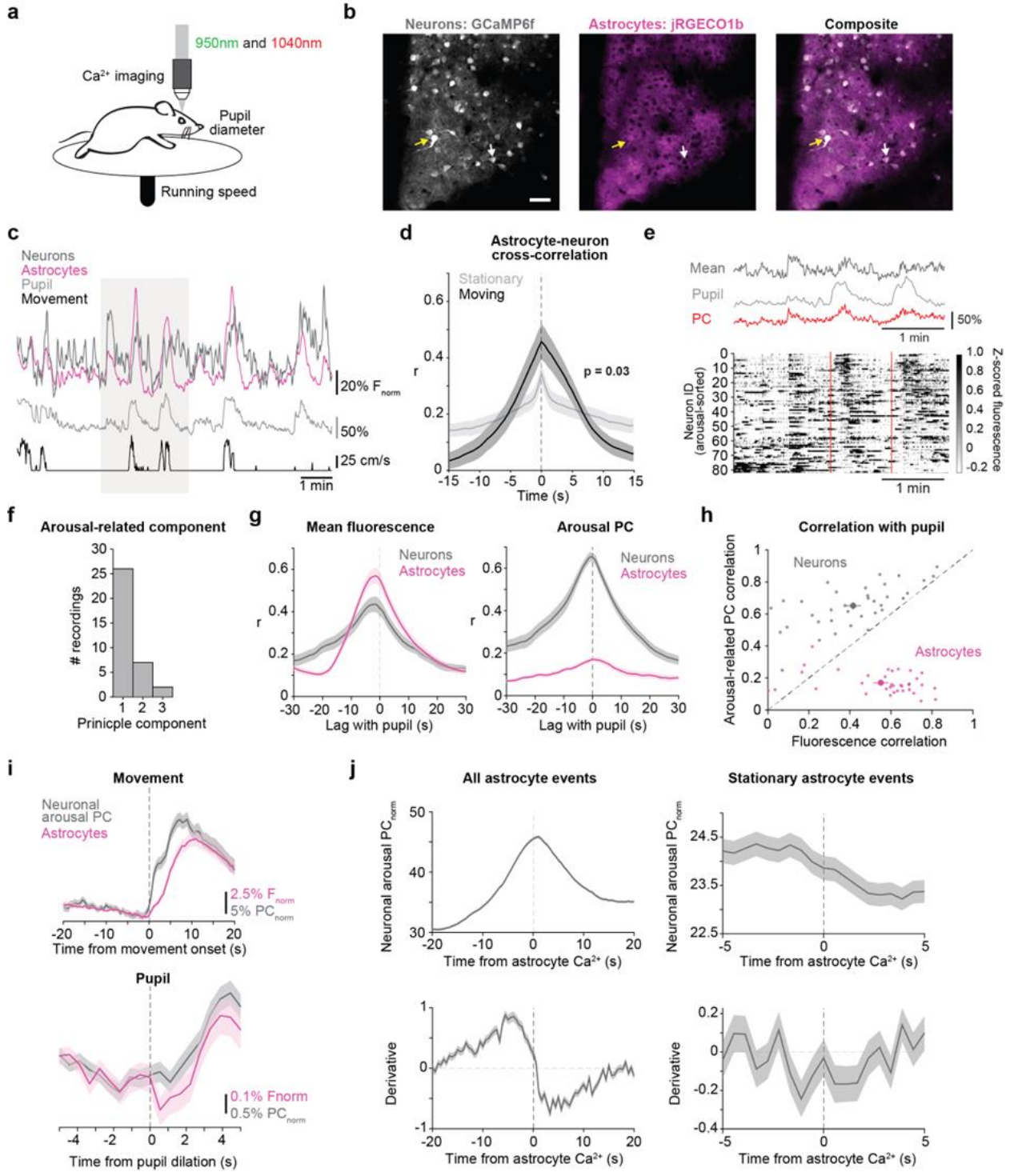
a
950nm and 1040nm
Ca2+ imaging
Pupil diameter
Running speed
b
Neurons: GCaMP6f
Astrocytes: jRGECO1b
Composite
c
Neurons
Astrocytes
Pupil
Movement
20% Fnorm
50%
25 cm/s
1 min
d
Astrocyte-neuron cross-correlation
Stationary
Moving
p = 0.03
r
Time (s)
e
Mean
Pupil
PC
50%
1 min
Neuron ID (arousal-sorted)
Z-scored fluorescence
f
Arousal-related component
recordings
Prinicple component
g
Mean fluorescence
Arousal PC
Neurons
Astrocytes
Lag with pupil (s)
h
Correlation with pupil
Arousal-related PC correlation
Fluorescence correlation
i
Movement
Neuronal arousal PC
Astrocytes
2.5% Fnorm
5% PCnorm
Time from movement onset (s)
Pupil
0.1% Fnorm
0.5% PCnorm
Time from pupil dilation (s)
j
All astrocyte events
Stationary astrocyte events
Neuronal arousal PCnorm
Time from astrocyte Ca2+ (s)
Derivative

Figure 3. Astrocyte Ca^{2+} precedes increased neuronal activity following spontaneous arousal.

(a) Experimental paradigm for dual-color Ca^{2+} imaging of neurons and astrocytes. **(b)** Representative 2P images of *in vivo* neuronal GCaMP6f (grey) and astrocyte jRGECO1b (magenta). Yellow arrows indicate bleed-through in the red channel, while white arrows show a neuron with no bleed through. Scale bar = 50µm. **(c)** Example of neuronal (dark grey) and astrocyte (magenta) Ca^{2+} activity, with pupil diameter (light grey) and wheel speed (black). **(d)** Astrocyte and neuronal Ca^{2+} were positively correlated, and increased their correlation during movement compared to stationary periods (two-sided Rank Sum test; throughout figure, n = 33 recordings from 8 mice). **(e)** Top: An example of pupil diameter (light grey) fluctuations alongside changes in the neuronal mean fluorescence (dark grey) and arousal-associated principal component (PC) of neuronal activity (red). Bottom: An example heatmap of single-cell neuronal activity sorted by arousal PC weight shows that the arousal PC captured heterogenous neuronal responses to arousal, including around movement events (red dashed lines). **(f)** The component number of the arousal PC. **(g)** Both neurons (grey) and astrocytes (pink) showed positive correlations between mean Ca^{2+} fluorescence and pupil diameter (left). Using PC analysis, we identified neuronal activity that showed strong correlation with pupil diameter, whereas astrocyte Ca^{2+} activity was not amenable to this analysis. **(h)** Scatter plot of the correlation between either arousal PC (y-axis) or mean fluorescence (x-axis) for each recording. PC analysis identified arousal-associated neuronal activity for neurons (grey dots), but not astrocytes (magenta dots). **(i)** Astrocyte Ca^{2} signaling (magenta) occurred alongside increase in arousal-associated neuronal activity (grey), and peaked with reductions in neuronal activity, for both movement (top, n = 134 movement bouts) and stationary increases in arousal (bottom, n = 772 pupil dilations). **(j)** Top: Arousal-associated neuronal activity tends to peak and then decrease around astrocyte Ca^{2+} activity both overall (left, n = $8.9e^{4}$ events) and during stationary periods (right, n = $3.2e^{4}$ events). Bottom: The derivative of arousal-associated neuronal activity demonstrates that arousal-associated neuronal activity decreases directly following astrocyte Ca^{2+} events both overall (left) and during stationary periods (right). All data is presented as mean ± S.E.M unless otherwise noted.

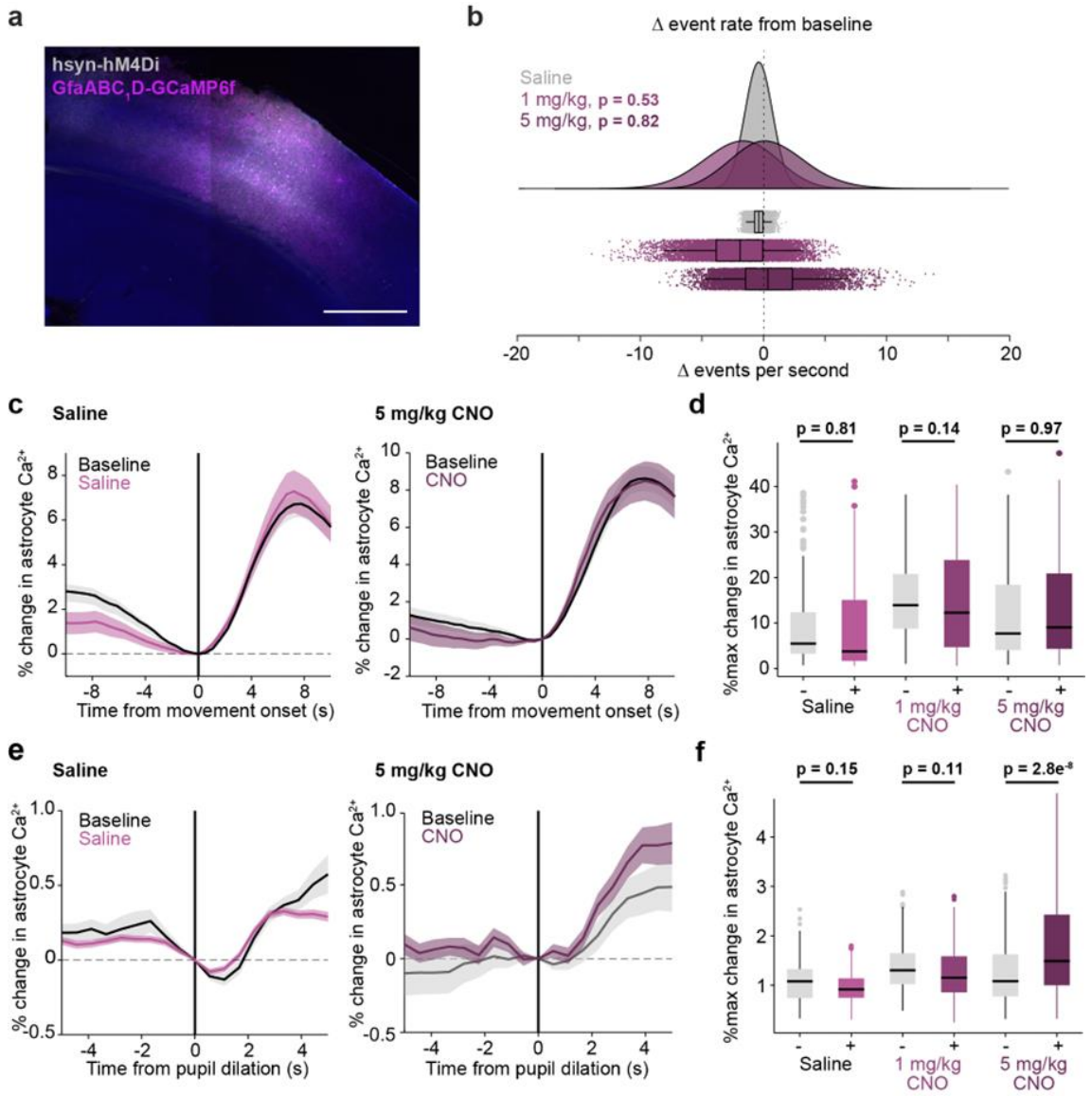

Figure 4. Arousal-driven astrocyte Ca^{2+} is not dependent on local neuronal activity.
(a) Confocal image showing cortical expression of both astrocyte GCaMP6f (magenta) and neuronal inhibitory DREADD hM4Di (grey). Scale bar = 500µm. **(b)** Bootstrapped change in astrocyte event rate (n = $1e^5$ resampled events from 5 mice) after saline (grey) or CNO (purple) administration. No significant change in astrocyte Ca^{2+} event rate was found when local neuronal activity was inhibited ($p < 0.05$, proportion of non-overlapping bootstrapped change in event rates). **(c)** Average change in astrocyte Ca^{2+} response to movement after saline (left) or CNO (right, 5mg/kg) compared to the baseline in each animal (black lines). **(d)** No significant ($p < 0.05$) difference in astrocyte Ca^{2+} responses (% change in astrocyte Ca^{2+} relative to t = 0; box and whisker plot with outliers as open circles), to movement after saline or either 1mg/kg or 5mg/kg of CNO was found (One-sided Kruskal-Wallis test, n and p-values listed in Supplementary Table 4). **(e)** Average change in astrocyte Ca^{2+} response to stationary pupil dilation after saline (left) or CNO (right, 5mg/kg). **(f)** No significant difference ($p < 0.05$) was found within saline or 1mg/kg CNO conditions. 5mg/kg CNO caused an enhancement in astrocyte responses to arousal (Kruskal-Wallis test, n and p-values listed in Supplementary Table 4). Boxplots show median and IQR, with whiskers extended to 1.5 * IQR. Line plots are presented as mean ± S.E.M.

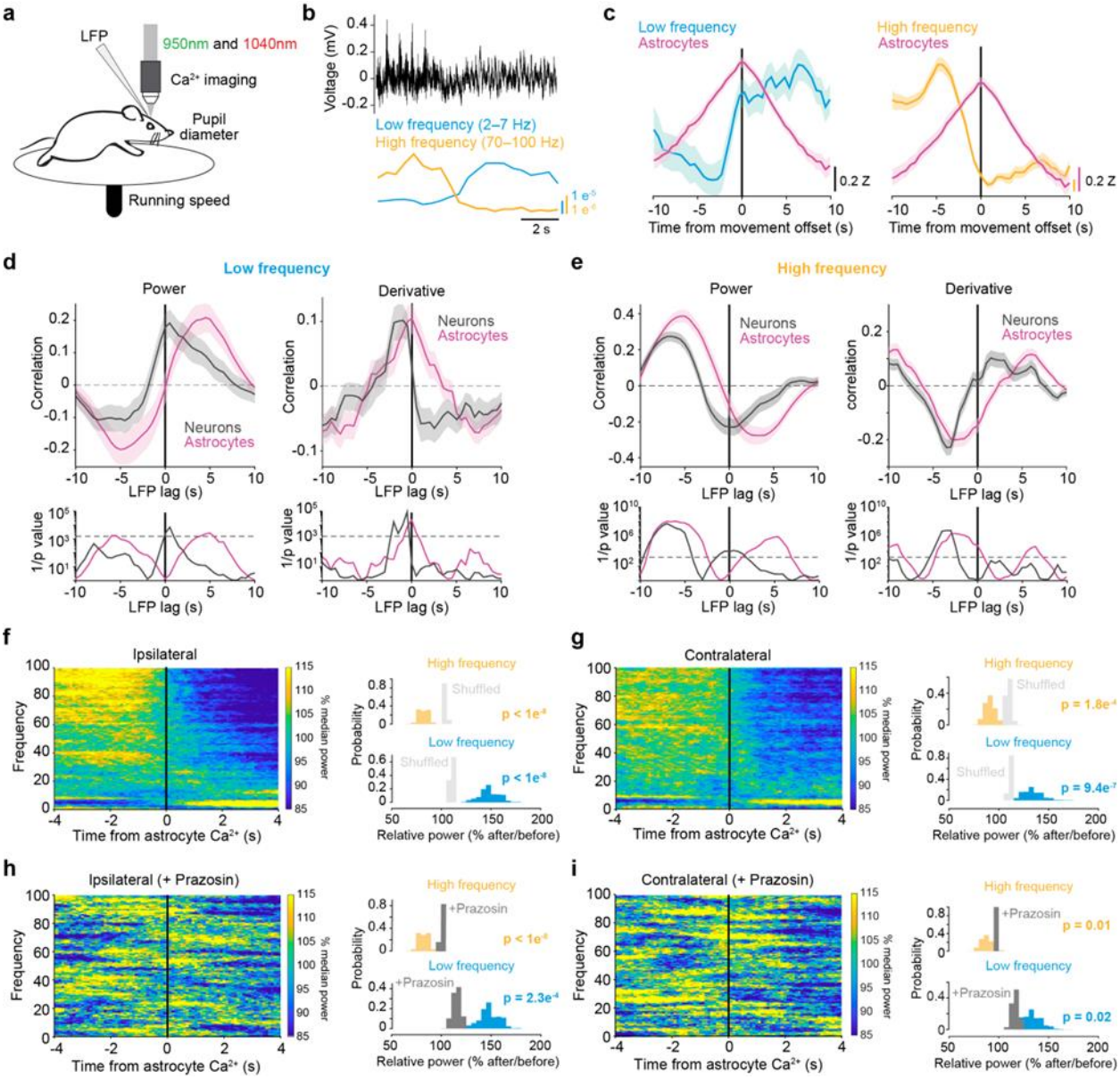
a
LFP
950nm and 1040nm
Ca2+ imaging
Pupil diameter
Running speed
b
Voltage (mV)
Low frequency (2–7 Hz)
High frequency (70–100 Hz)
2 s
c
Low frequency
Astrocytes
High frequency
Astrocytes
0.2 Z
Time from movement offset (s)
d
Low frequency
Power
Derivative
Neurons
Astrocytes
Correlation
1/p value
LFP lag (s)
e
High frequency
Power
Derivative
Neurons
Astrocytes
f
Ipsilateral
Frequency
% median power
Time from astrocyte Ca2+ (s)
High frequency
Shuffled
p < 1e-4
Low frequency
Shuffled
p < 1e-4
Probability
Relative power (% after/before)
g
Contralateral
High frequency
Shuffled
p = 1.8e-4
Low frequency
Shuffled
p = 9.4e-7
h
Ipsilateral (+ Prazosin)
High frequency
+Prazosin
p < 1e-4
Low frequency
+Prazosin
p = 2.3e-4
i
Contralateral (+ Prazosin)
High frequency
+Prazosin
p = 0.01
Low frequency
+Prazosin
p = 0.02

Figure 5. NE-dependent astrocyte Ca^{2+} occurs at the crux of cortical state changes.
(a) Experimental set-up. **(b)** Example LFP data (black) with calculated low-frequency (2–7Hz, blue) and high-frequency (70–100Hz, orange) power. **(c)** Average LFP low-frequency (left) and high-frequency (right) power with astrocyte Ca^{2+} activity (magenta) around movement offset at t = 0s (n = 52 offsets from 4 mice). **(d)** Top: Cross-correlation between astrocyte (magenta) or neuronal Ca^{2+} (grey) activity and low-frequency power (left), or the derivative of low-frequency power (right). Bottom: significance (1/p, two-sided signed-rank test) for astrocytes and neurons. Dashed line is the threshold of correction for multiple comparison. **(e)** High-frequency power and its derivative are cross-correlated to neuronal and astrocyte Ca^{2+}, as for low-frequency power in (d). Neuronal Ca^{2+} correlated with LFP power while Astrocyte Ca^{2+} correlated with the derivative of LFP power. **(f–i)** LFP power dynamics in ipsilateral (f) and contralateral (g) cortex, centered around astrocyte Ca^{2+} onsets at t = 0s. LFP power in a 5s window around astrocyte Ca^{2+} events was computed, and each frequency was normalized by its median power. (All p-values from HB). **(f–g)** Left: astrocyte Ca^{2+} events occur at the crux of ipsilateral (f , n = 4 mice) and contralateral (g, n = 5 mice) LFP state transitions from high- to low-frequency-dominated states. Comparisons are made using HB between empirical data (colored bars) and shuffled distributions (light grey). Right: high-frequency power (orange) decreased and low-frequency power (blue) increased after astrocyte Ca^{2+} events. **(h–i)** This relationship was abolished in both ipsilateral (h) and contralateral (i) cortical LFP recordings after administration of the Adra1 receptor antagonist Prazosin (5mg/kg, i.p., n = 4 mice), for both low- and high-frequency power (comparisons are made using HB between state changes without Prazosin (colored bars) and with the addition of Prazosin (dark grey). Line plots are presented as mean ± S.E.M.

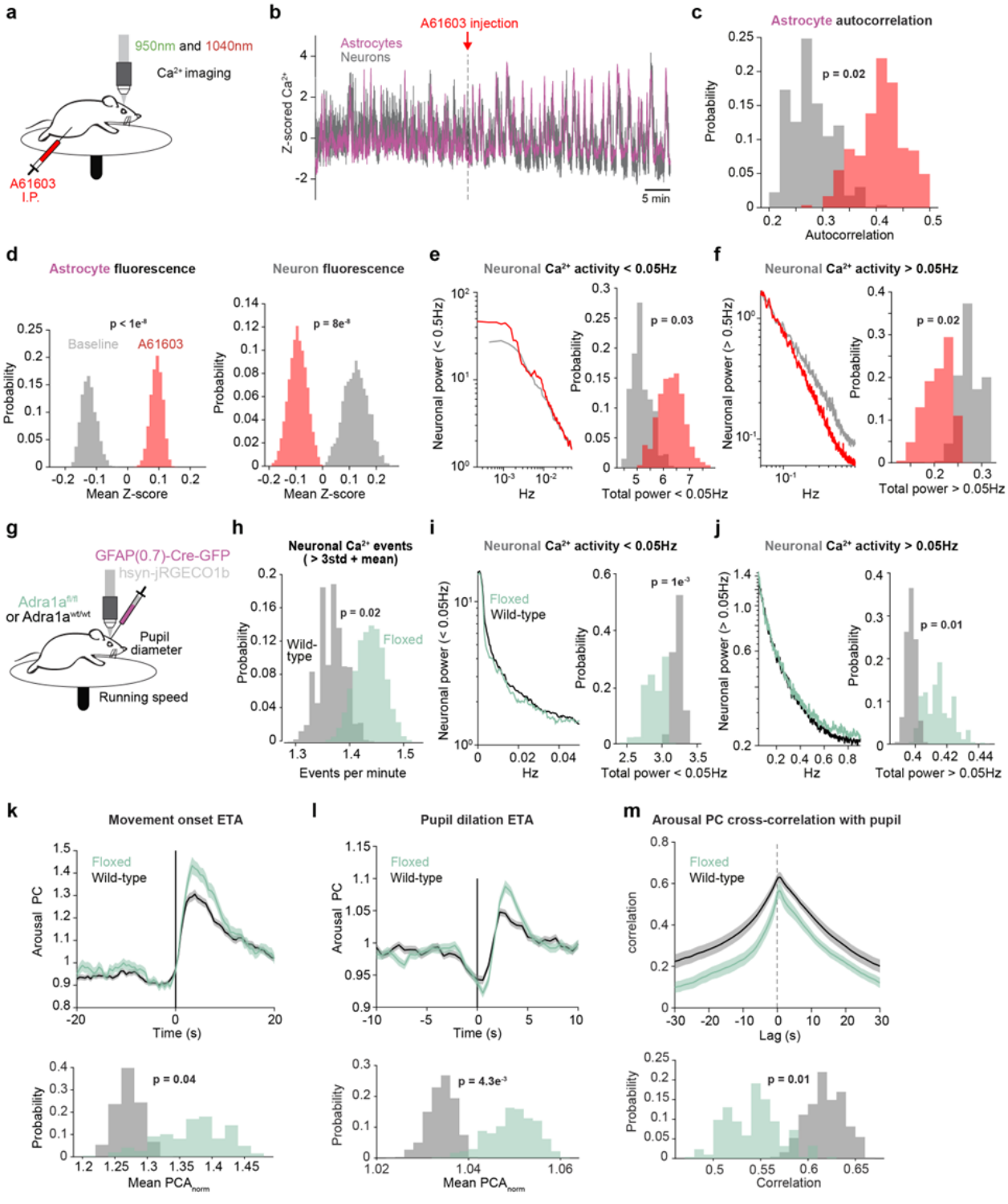
a
950nm and 1040nm
Ca2+ imaging
A61603
I.P.
b
A61603 injection
Astrocytes
Neurons
Z-scored Ca2+
5 min
c
Astrocyte autocorrelation
p = 0.02
Probability
Autocorrelation
d
Astrocyte fluorescence
p < 1e-8
Baseline
A61603
Probability
Mean Z-score
Neuron fluorescence
p = 8e-8
Probability
Mean Z-score
e
Neuronal Ca2+ activity < 0.05Hz
Neuronal power (< 0.5Hz)
Hz
p = 0.03
Probability
Total power < 0.05Hz
f
Neuronal Ca2+ activity > 0.05Hz
Neuronal power (> 0.5Hz)
Hz
p = 0.02
Probability
Total power > 0.05Hz
g
GFAP(0.7)-Cre-GFP
hsyn-jRGECO1b
Adra1a fl/fl
or Adra1a wt/wt
Pupil diameter
Running speed
h
Neuronal Ca2+ events
(> 3std + mean)
p = 0.02
Wild-type
Floxed
Probability
Events per minute
i
Neuronal Ca2+ activity < 0.05Hz
Floxed
Wild-type
Neuronal power (< 0.05Hz)
Hz
p = 1e-3
Probability
Total power < 0.05Hz
j
Neuronal Ca2+ activity > 0.05Hz
Neuronal power (> 0.05Hz)
Hz
p = 0.01
Probability
Total power > 0.05Hz
k
Movement onset ETA
Floxed
Wild-type
Arousal PC
Time (s)
p = 0.04
Probability
Mean PCA norm
l
Pupil dilation ETA
Floxed
Wild-type
Arousal PC
Time (s)
p = 4.3e-3
Probability
Mean PCA norm
m
Arousal PC cross-correlation with pupil
Floxed
Wild-type
correlation
Lag (s)
p = 0.01
Probability
Correlation

Figure 6. Adra1a receptors modulate basal neuronal activity and neuronal population responses to arousal.

(a) Experimental schematic for dual-color imaging with *in vivo* pharmacology. **(b)** An example of population astrocyte (magenta) and neuron (grey) Ca^{2+} activity in response to A61603 (10µg/kg, i.p.). **(c–f)** Histograms show differences between metrics at baseline (grey) or after A61603 (red) using HB (n = 4 mice panels c–g). **(c)** Astrocyte Ca^{2+} activity became more homogenous as measured by autocorrelation. **(d)** Astrocytes (left) showed increased population Ca^{2+} fluorescence while neurons (right) showed decreased population Ca^{2+} fluorescence after A61603 administration. **(e)** Neuronal activity power spectra < 0.05Hz (left) showed more power after A61603 injection (right, HB). **(f)** Same as in (e) for power > 0.05Hz. (**g)** Schematic for neuronal Ca^{2+} imaging in homozygous $Adra1a^{fl/fl}$ mice and wild-type litter-mate controls; all mice were injected with GFAP-Cre (n = 4 $Adra1a^{fl/fl}$ and 4 wild-type littermate controls, panels h–l). **(h)** Overall, neuronal activity was increased in $Adra1a^{fl/fl}$ mice (green) relative to wild-type (grey). **(i–j)** Neuronal activity < 0.05Hz was decreased and neuronal activity > 0.05Hz was increased in $Adra1a^{fl/fl}$ mice. **(k)** Arousal-associated neuronal activity was increased following movement in $Adra1a^{fl/fl}$ mice (green, n = 177 movement bouts) compared to wild-type (grey, n = 400). **(l)** $Adra1a^{fl/fl}$ mice (green, n = 923 pupil dilations) showed increased arousal-associated neuronal activity compared to wild-type (grey, n = 1396 pupil dilations) following stationary increases in pupil diameter. **(m)** Arousal-associated neuronal activity was less correlated with the pupil diameter overall in $Adra1a^{fl/fl}$ (green, n=23 recordings) compared to wild-type mice (grey, n = 14 recordings). For all panels histograms are showing HB distributions (n = 4 $Adra1a^{fl/fl}$ and 4 wild-type littermate controls). All line plots are presented as mean ± S.E.M.

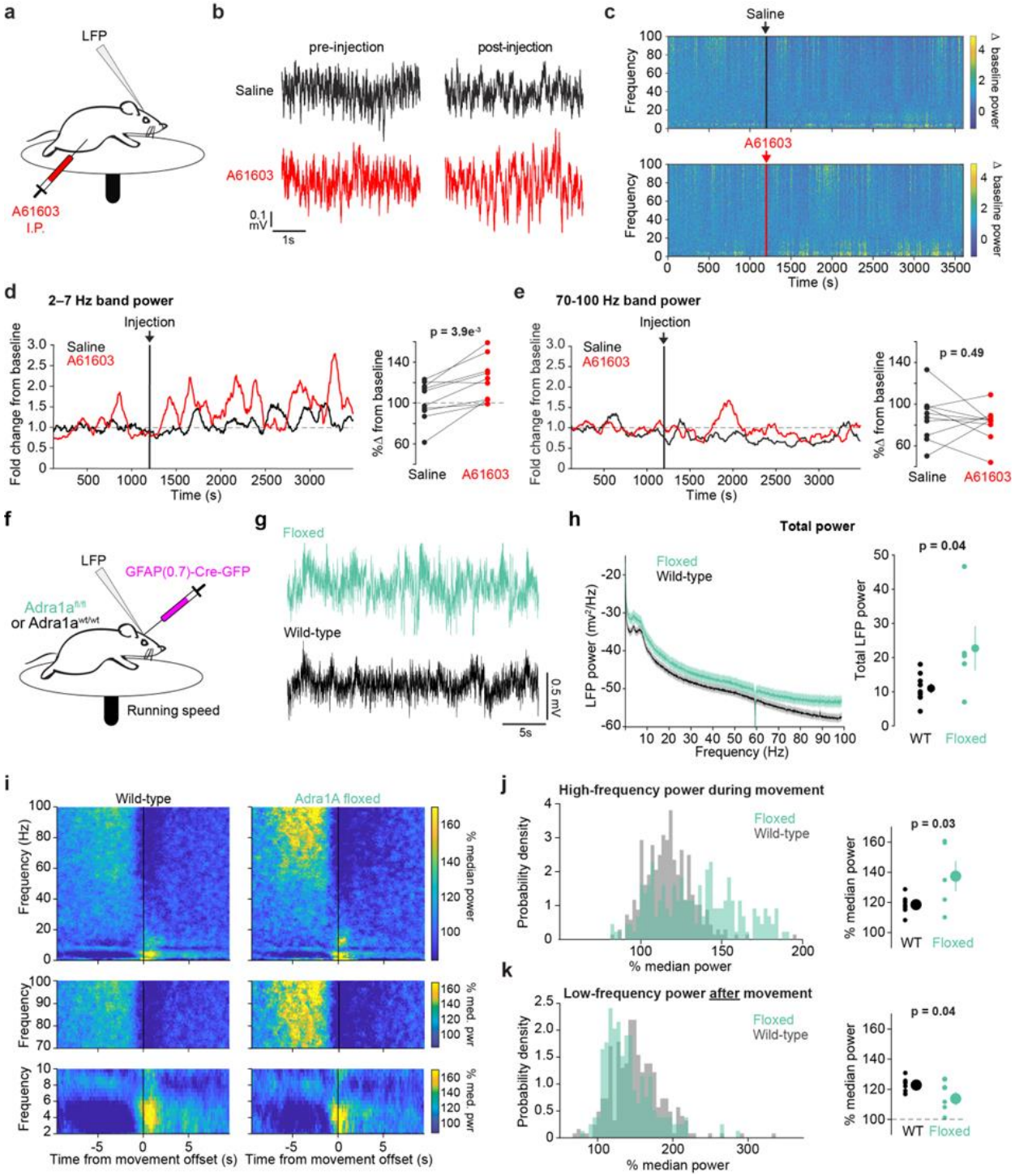
a
LFP
A61603
I.P.
b
pre-injection
post-injection
Saline
A61603
0.1 mV
1s
c
Saline
A61603
Frequency
Δ baseline power
Time (s)
d
2–7 Hz band power
Injection
Saline
A61603
Fold change from baseline
Time (s)
p = 3.9e-3
%Δ from baseline
e
70-100 Hz band power
p = 0.49
f
LFP
GFAP(0.7)-Cre-GFP
Adra1a fl/fl
or Adra1a wt/wt
Running speed
g
Floxed
Wild-type
0.5 mV
5s
h
Total power
LFP power (mv²/Hz)
Frequency (Hz)
p = 0.04
Total LFP power
WT
Floxed
i
Wild-type
Adra1A floxed
Frequency (Hz)
% median power
Time from movement offset (s)
j
High-frequency power during movement
Probability density
% median power
p = 0.03
k
Low-frequency power after movement
p = 0.04

Figure 7. Genetic removal of astrocyte Arda1a impairs cortical resynchronization after arousal.

(a) Experimental set-up for LFP recording with *in vivo* pharmacology. **(b)** Example cortical LFP data following i.p. injections of either saline (black) or the Adra1a-specific agonist A61603 (1µg/Kg, red). **(c)** Representative spectrograms from saline- (top) and A61603-injected (bottom) mice. Arrows and vertical lines indicate time of injection. **(d)** Left: example of 2–7Hz band power change with saline or A61603 injection, smoothed with a two-minute moving average. Right: A61603 increased low-frequency power compared to saline (two-sided signed-rank test, n = 10 mice). **(e)** Left: Representative trace of 70–100Hz band power with saline or A61603 injection. Right: A61603 did not affect high-frequency power compared to saline (two-sided signed-rank test, n = 10 mice). **(f)** LFP recordings were performed in homozygous Adra1a$^{fl/fl}$ mice and wild-type litter-mate controls; all mice were injected with GFAP-Cre. **(g)** Representative 30s of LFP data from Adra1a$^{fl/fl}$ (green) and wild-type (black) mice. **(h)** Average LFP spectra from Adra1a$^{fl/fl}$ (n = 5) and wild-type (n = 9) mice, with total LFP power higher in Adra1a$^{fl/fl}$ mice (two-sided t-test, shaded region shows theoretical error bars with p = 0.05). **(i)** Average LFP spectrograms around movement offset (t = 0s) for wild-type (left) and Adra1a$^{fl/fl}$ (right) mice. Data are normalized by the median power at each frequency to show state-related changes in LFP. Top: entire spectrograms from 0–100Hz. Middle: 70–100Hz range showing increased power in Adra1a$^{fl/fl}$ mice compared to wild-type during movement. Bottom: 2–7Hz range showing reduced power after movement offset in Adra1a$^{fl/fl}$ mice. **(j)** There was increased 70–100Hz power in Adra1a$^{fl/fl}$ mice during movement (left, n = 303 wild-type and 194 Adra1a$^{fl/fl}$ movement offsets) between cohorts (right, n = 5 Adra1a$^{fl/fl}$ and 9 wild-type mice, two-sided t-test). **(k)** Same as in (j) for 2–7Hz power after mice stopped moving. For all scatter plots, individual data is plotted as mean ± S.E.M.

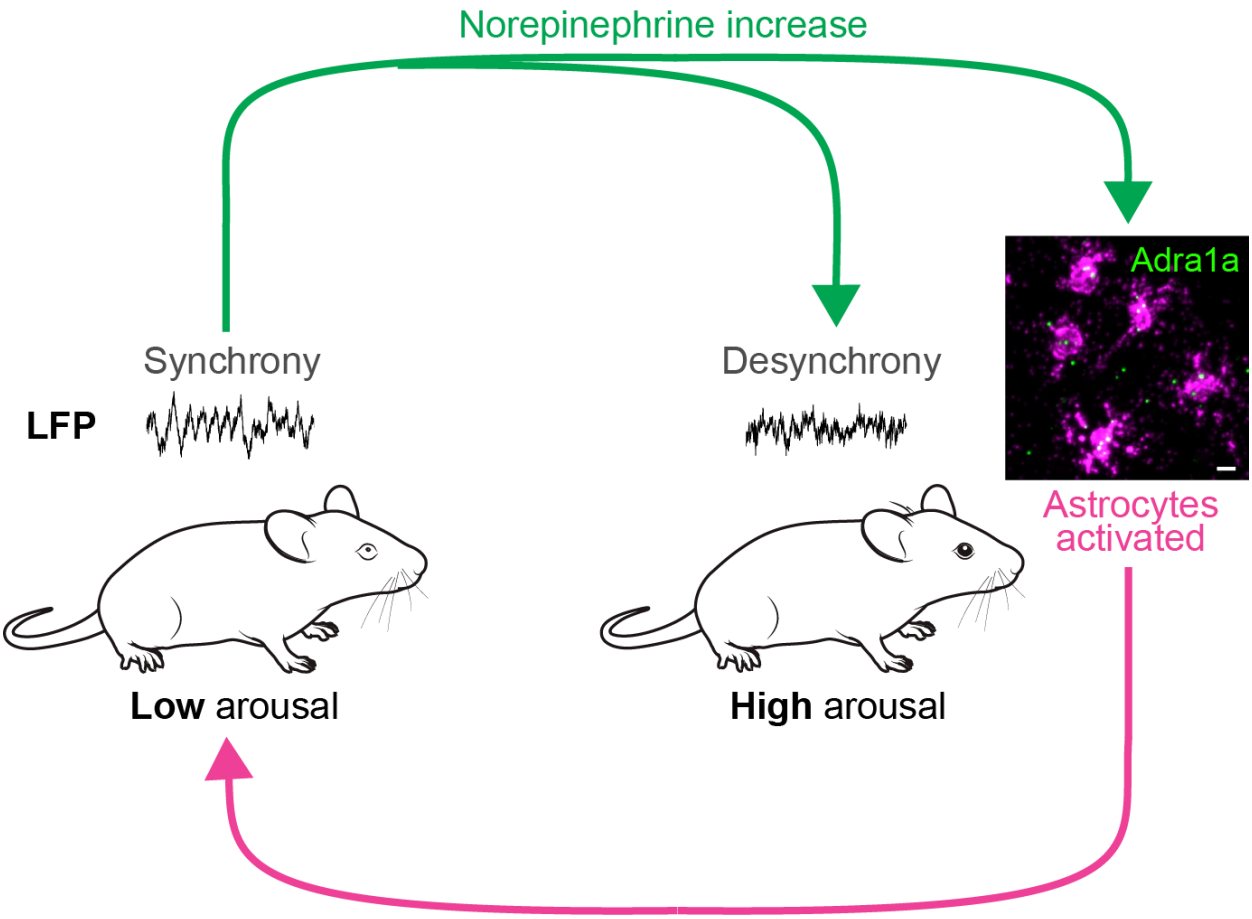

Figure 8. Model of astrocyte regulation of arousal-associated cortical state.
NE (green arrows) drives changes from states of low arousal with synchronized cortical activity (left) to states of high arousal with desynchronized cortical activity (right). Simultaneous activation of astrocytes through the Adra1a receptor leads to Ca^{2+} signaling (magenta arrow) which drives the cortex back to a synchronized state following increases in arousal. Scale bar = 10µm.

1.7 Extended Data

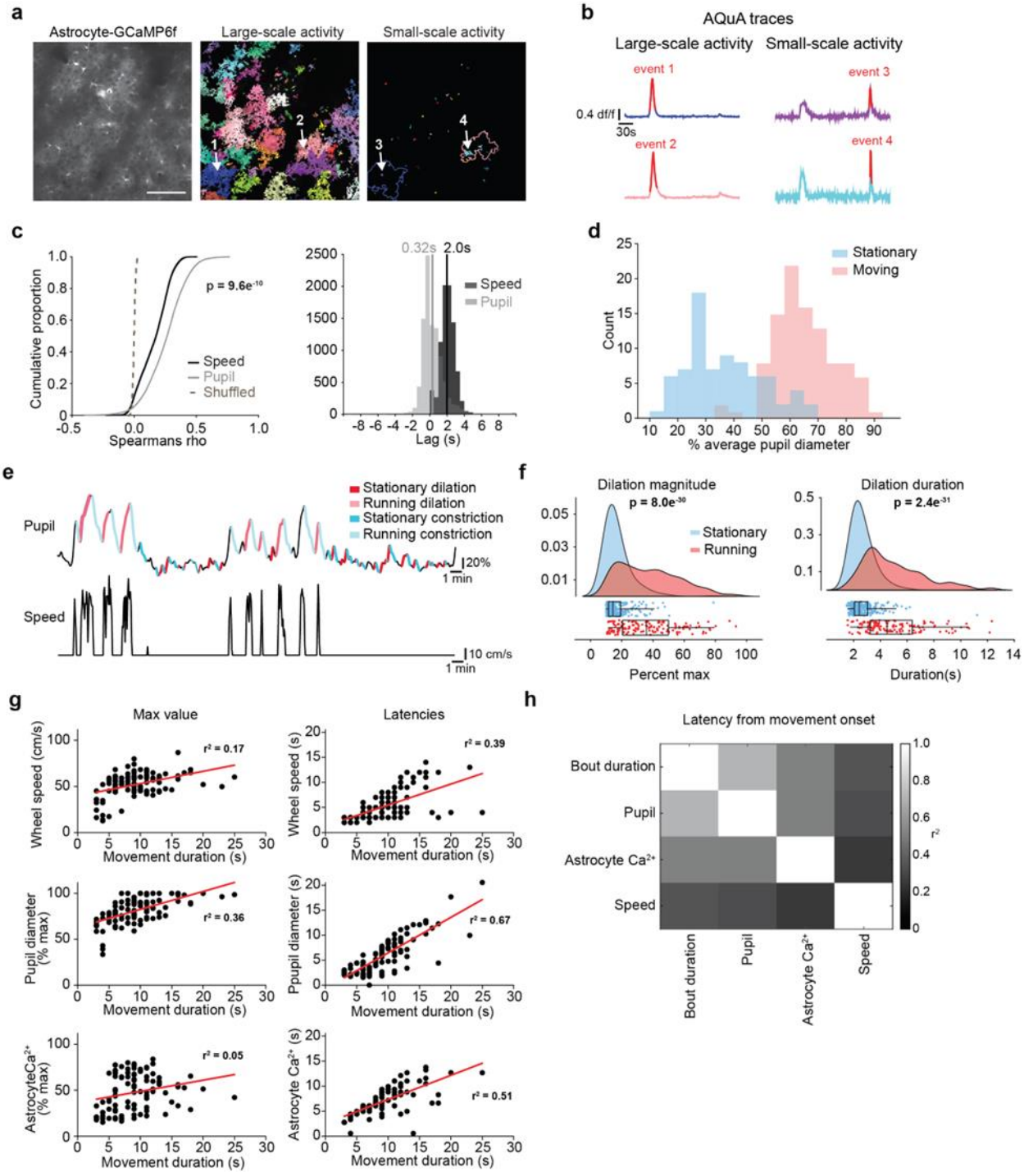

Extended Data Figure 1. Dissection of astrocyte Ca^{2+} and behavioral state.
(a) 2P mean projection image of *in vivo* astrocyte GcaMP6f (left, scale bar = 100µm). AQuA detected both large (middle) and small (right) astrocyte Ca^{2+} events within the entire movie, even when they were spatially overlapping. Arrows indicate two pairs of spatially overlapping events (arrows 1 and 3, and arrows 2 and 4). **(b)** Traces from the AQuA events shown in (a), with the time period of the AQuA-detected event highlighted in red. **(c)** Related to Fig. 1c: Individual astrocyte Ca^{2+} events correlated better with pupil diameter (left, n = $1.2e^4$ Ca^{2+} events, One-sided Kruskal-Wallis test) and had a shorter lag with pupil diameter than wheel speed (right, pupil n = $9.6e^3$, wheel n = $8.3e^3$, rank-sum test). **(d)** Related to Fig. 1d: average pupil diameter during movement (n = 100) and stationary periods (n = 76). **(e)** Classification of behavioral state by both pupil diameter and movement. **(f)** Pupil dilation is smaller (left) and shorter (right, rank-sum tests) during stationary periods (n = 261 dilations, blue) compared with movement-associated dilations (n = 136 dilations, red, boxplots show median and IQR with whiskers to 1.5 * IQR). **(g)** Related to Fig. 1l: Left: Movement duration (n = 104) was related to the maximum wheel speed (top) and pupil diameter (middle), but not to the maximum astrocyte Ca^{2+} (bottom). Right: the latency to the maximum wheel speed (top), pupil diameter (middle), and astrocyte Ca^{2+} (bottom) were strongly linked to movement duration. **(h)** Heatmap summary of the r^2 between the latencies in (g) right, and movement bout duration.

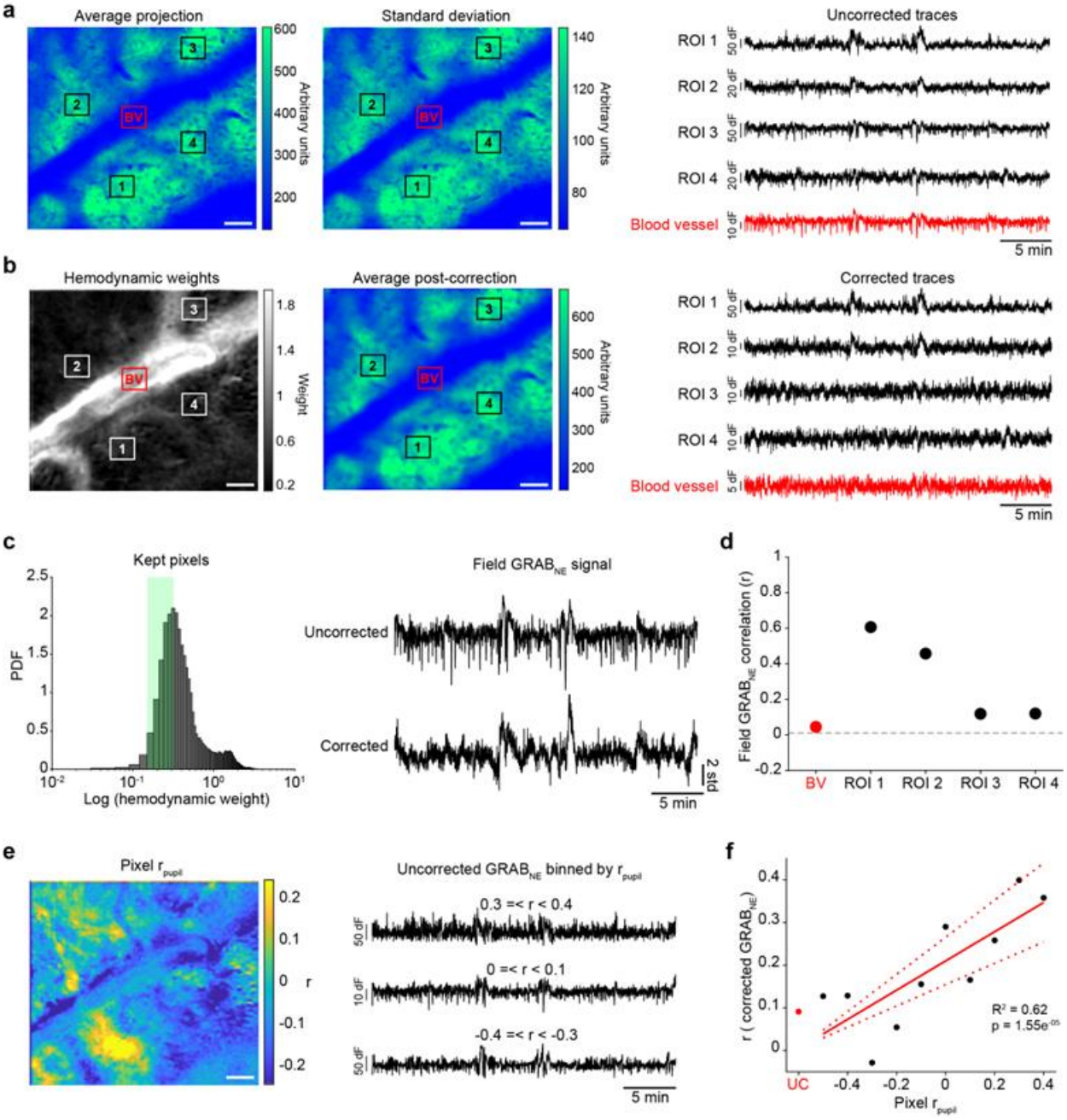
a
Average projection
Standard deviation
Uncorrected traces
ROI 1
ROI 2
ROI 3
ROI 4
Blood vessel
Arbitrary units
5 min
b
Hemodynamic weights
Average post-correction
Corrected traces
Weight
c
Kept pixels
PDF
Log (hemodynamic weight)
Field GRAB$_{NE}$ signal
Uncorrected
Corrected
2 std
d
Field GRAB$_{NE}$ correlation (r)
BV
e
Pixel r$_{pupil}$
Uncorrected GRAB$_{NE}$ binned by r$_{pupil}$
0.3 =< r < 0.4
0 =< r < 0.1
-0.4 =< r < -0.3
f
r (corrected GRAB$_{NE}$)
UC
Pixel r$_{pupil}$
R² = 0.62
p = 1.55e-05

Extended Data Figure 2. Hemodynamic correction of 2P $GRAB_{NE}$ signals
(a) Left: Average projection of a single $GRAB_{NE}$ recording with four regions-of-interest (ROI) in areas with clear $GRAB_{NE}$ fluorescence (black squares, labeled 1–4) and one ROI in a blood vessel (red square, labeled BV). Middle: standard deviation projection. Right: average fluorescence in each ROI before hemodynamic correction. **(b)** Left: Estimated hemodynamic signal present in each pixel. Middle: recovered average projection after hemodynamic correction. Note average fluorescence after hemodynamic correction is broadly similar the uncorrected data in (a) with some blurring due to Gaussian smoothing in preprocessing. Right: average fluorescence in each ROI after hemodynamic correction. **(c)** ROI-free methodology for obtaining $GRAB_{NE}$ signal. Left: Following hemodynamic correction, the bottom quartile of pixels with the lowest hemodynamic weights, excluding the bottom 1% which often had artefactual signals, were kept. Right: These pixels were averaged together to produce the corrected $GRAB_{NE}$ signal (bottom) which had substantially less hemodynamic contamination than the uncorrected field fluorescence (top). **(d)** Correlation between the corrected $GRAB_{NE}$ signal and the uncorrected ROIs in (a) and (b). **(e)** Left: Correlation between uncorrected $GRAB_{NE}$ fluorescence and pupil diameter. Right: Example traces from the average of pixels that were positively correlated (top), negatively correlated (bottom), or showed little relationship (middle) with pupil diameter. **(f)** The corrected $GRAB_{NE}$ signal is not very similar to average uncorrected $GRAB_{NE}$ signal (red dot) but instead reflects the $GRAB_{NE}$ signal of binned pixels (black dots) that are correlated to the pupil diameter ($R^2 = 0.62$, $p = 1.55^{-5}$)

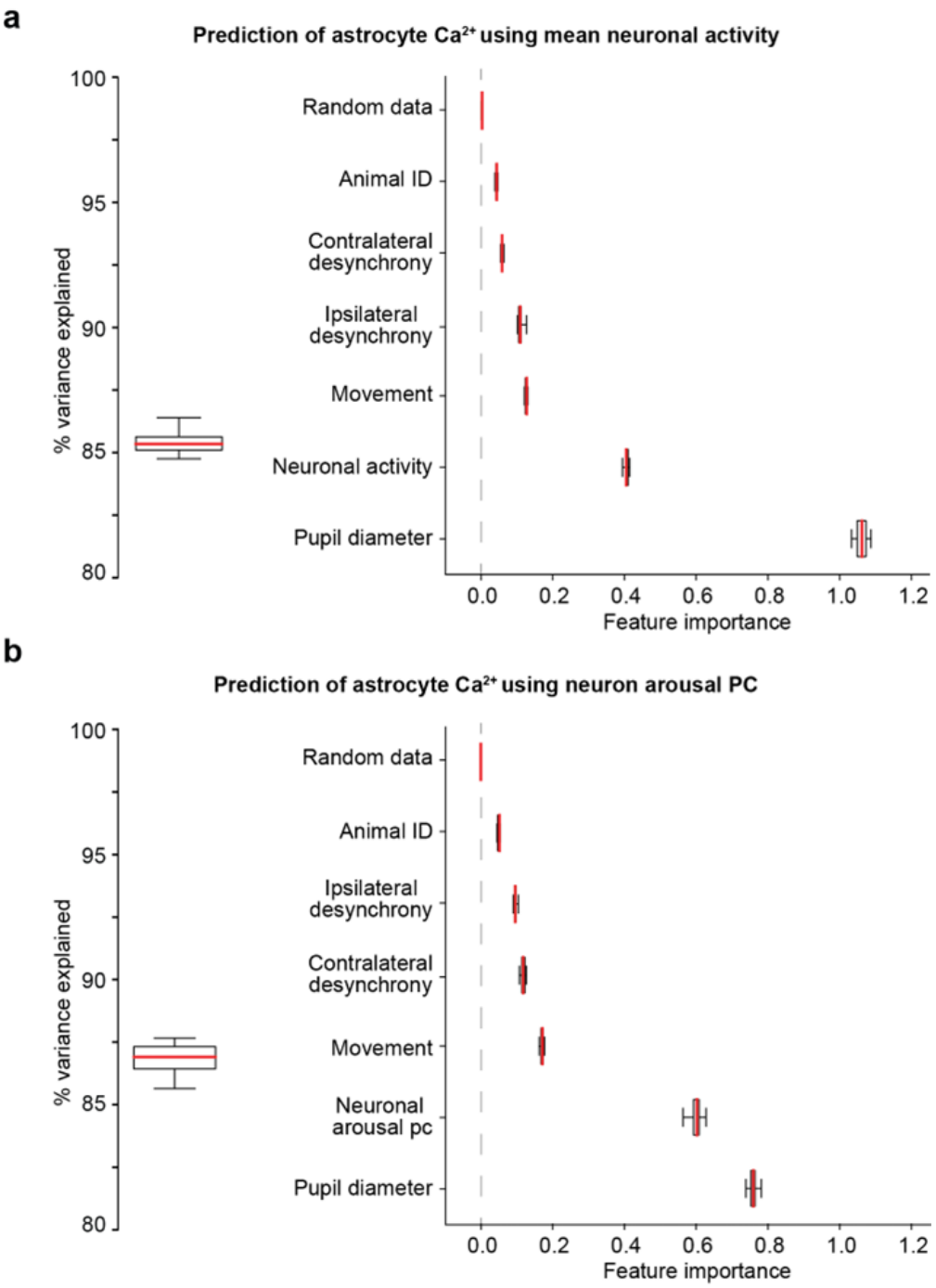

Extended Data Figure 3. Analysis of contributions to astrocyte Ca^{2+}
(a) Left: A Random Forest Regression model was trained (80% of data, $2.3e^4$ samples) to predict (20% of data, 5.6^3 samples) average astrocyte Ca^{2+} fluorescence accurately (mean r^2 = 0.85 ± $4.5e^{-3}$ std, n = 10 cross-validations). Right: Relative feature importance based on permutation testing of each predictor. Randomly generated data was included as a negative control and did not inform model predictions. **(b)** Same analysis as in (a), using the neuronal arousal PC rather than average neuronal activity. Random Forest Regression using the neuronal arousal PC showed a similar accuracy to that using mean neuronal fluorescence (mean r^2 = 0.87 ± $6.4e^{-3}$ std, n = 10 cross-validations). Boxplots show median and IQR with whiskers to 1.5 * IQR.

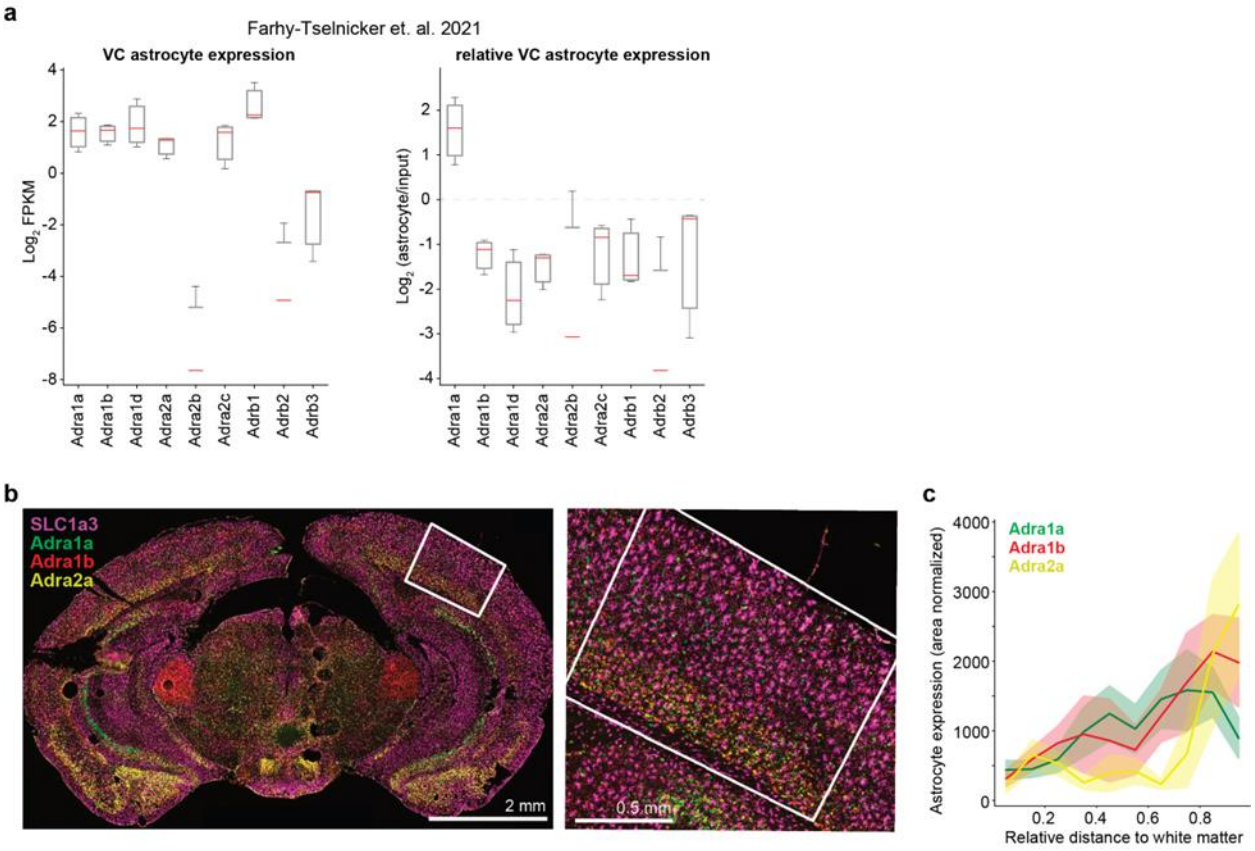

Extended Data Figure 4. Cortical astrocyte expression of adrenergic receptors.
(a) Ribosomal-mRNA expression in visual cortex astrocytes of P120 mice from the Farhy-Tselnicker et. al. publicly available dataset. Visual cortex astrocytes show expression of many adrenergic receptors (left) but preferentially express the Adra1a receptor relative to input control (right). **(b)** Left: Representative brain section with Adra1a (green), Adra1b (red), and Adra2a (yellow) mRNA labeled by smFISH using the LaST map pipeline[50]. SLC1a3 (GLAST) mRNA expression (purple) was used to define the location of astrocytes. The white square shows a representative ROI used to quantify visual cortex expression. Right: High-magnification image of visual cortex, showing receptor mRNA both within astrocytes marked by high GLAST mRNA (purple), and outside of astrocytes. **(c)** Quantification of NE-receptor mRNA expression in visual cortex astrocytes, quantified by relative cortical depth. Line plots show mean ± std (n = 3 mice, 7 ROIs).

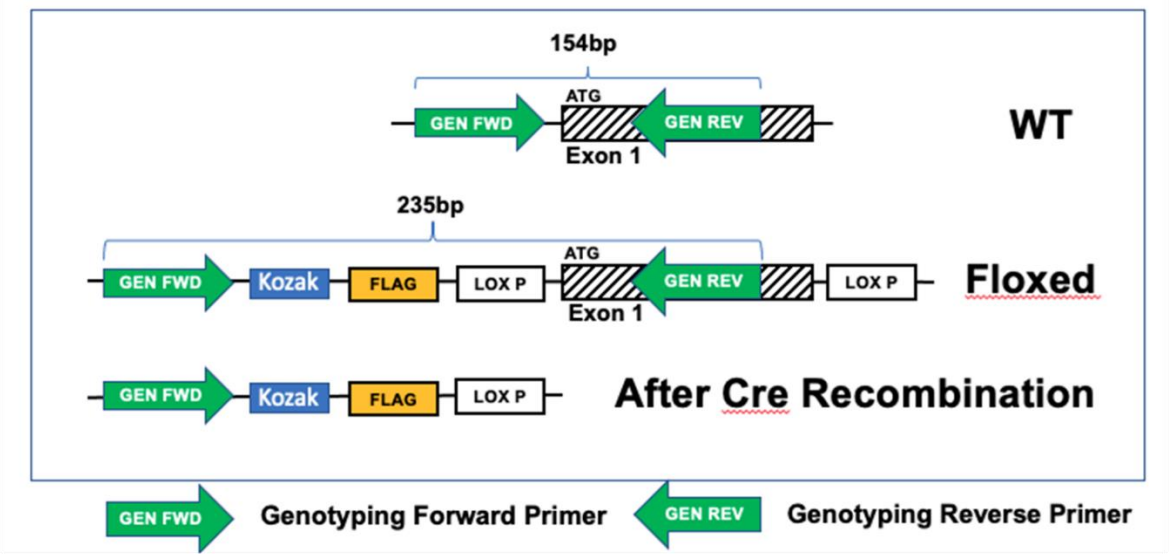

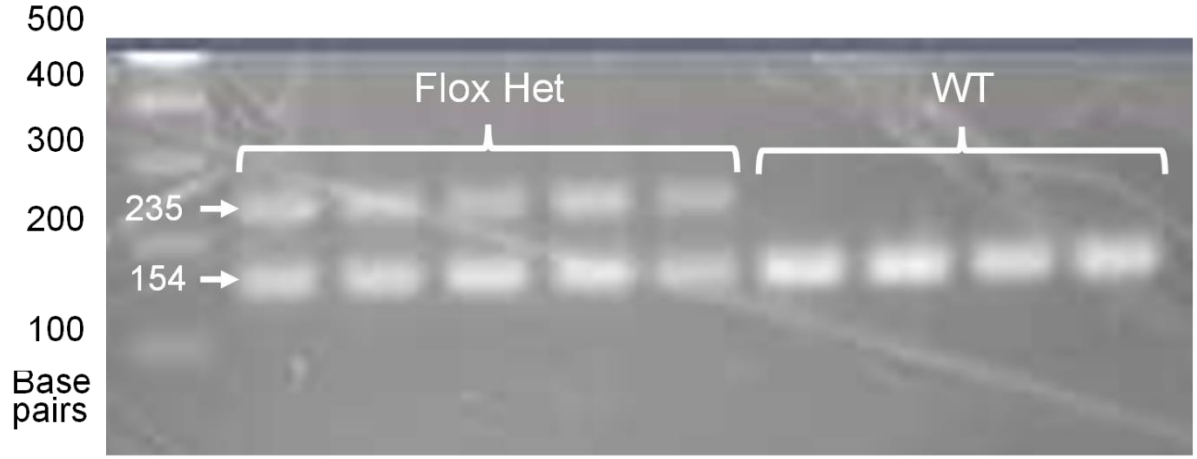

Extended Data Figure 5. Generation of Adra1a$^{fl/fl}$ mice.
Top: schematic of the genetic strategy used to generate conditional deletion of Adra1a. Primers (green arrows) were designed to identify and distinguish between the endogenous and knock-in Adra1a alleles. Bottom: Numbers are in base pairs. Validation of the knock-in strategy used to generate Adra1a$^{fl/fl}$ mice. PCR of Adra1a$^{fl/+}$ mice generates both a 154 base pair band corresponding to the wild type allele and a 235 base pair band corresponding to successful LoxP knock-in, which is not found in wild-type mice.

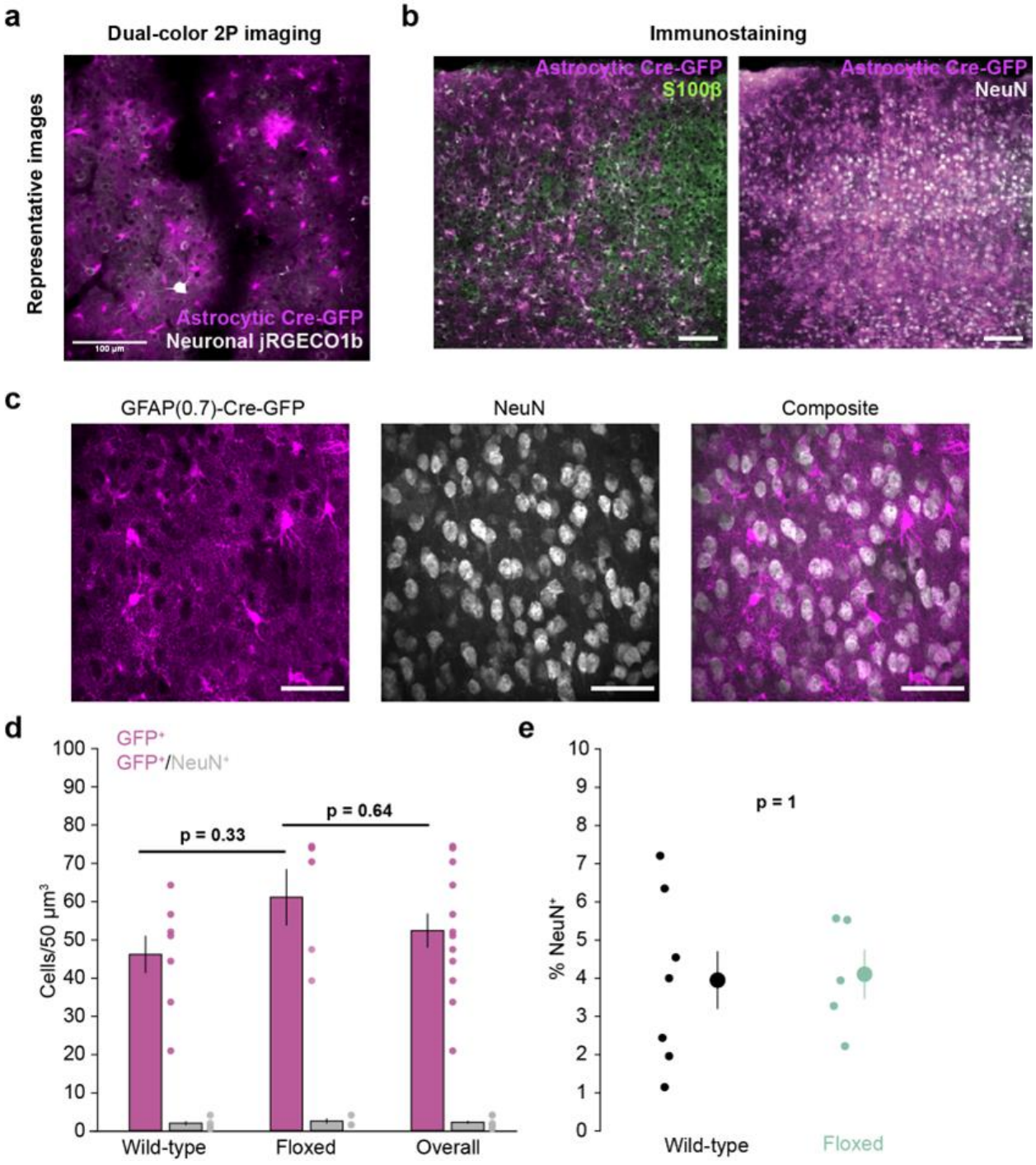
a
Dual-color 2P imaging
Representative images
Astrocytic Cre-GFP
Neuronal jRGECO1b
100 μm
b
Immunostaining
Astrocytic Cre-GFP
S100β
Astrocytic Cre-GFP
NeuN
c
GFAP(0.7)-Cre-GFP
NeuN
Composite
d
GFP+
GFP+/NeuN+
Cells/50 μm3
p = 0.33
p = 0.64
Wild-type
Floxed
Overall
e
% NeuN+
p = 1
Wild-type
Floxed

Extended Data Figure 6. Astrocyte-specific Cre expression.
(a) Representative average 2P image of *in vivo* neuronal jRGECO1b (gray) and astrocytes expressing Cre-GFP (magenta) **(b)** Example images show astrocyte-specific Cre-GFP (magenta) expression overlaps with the astrocyte marker S100β (left, green) but not the neuronal marker NeuN (right, grey), scale bar = 100µm. **(c)** Representative mean-projection of a confocal 60x z-stack used for cell counting. Each animal had two sections with each section having six distinct field-of-views containing 20 z-planes. GFAP(0.7)-Cre-GFP expression (left) was highly astrocytic and the neuronal marker NeuN (middle) was rarely colocalized (right, scale bars = 50µm). **(d)** Cre expression in neurons (grey bars) was low across genotypes (overall = 2.2 ± 0.39 neurons/50µm^3) and no difference was found between Cre expression in Adra1a$^{fl/fl}$ mice and control mice or the cohort as a whole (One-sided Kruskal-Wallis test). **(e)** Cre-expressing neurons were rare in both wild-type (black, 4.0% ± 0.75%) and Adra1a$^{fl/fl}$ mice (green, 4.1% ± 0.65%, two-sided ranked-sum test). (n = 7 Adra1a$^{fl/fl}$ and n = 5 wild-type mice for all graphs. Data are presented as mean ± S.E.M.)

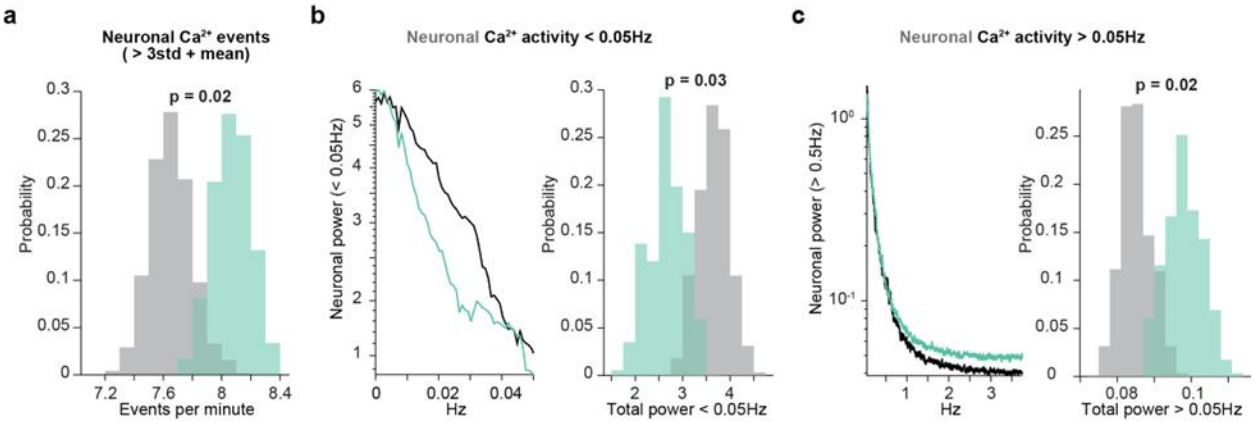

Extended Data Figure 7. Increased activity in Adra1a$^{fl/fl}$ mice imaging at 7.5Hz.
(a–c) Histograms show neuronal activity in Adra1a$^{fl/fl}$ (green) and wild-type littermate mice (grey) based on HB. **(a)** Neuronal Ca^{2+} event rate was increased in Adra1a$^{fl/fl}$ (green, n = 4 mice) compared to wild-type mice (grey, n = 4 mice). **(b)** Left: power spectrum of Adra1a$^{fl/fl}$ (green) and wild-type (black) Ca^{2+} activity between 0–0.05 Hz. Right: Total power in 0–0.05Hz neuronal Ca^{2+} activity, comparing Adra1a$^{fl/fl}$ and wild-type mice. **(c)** Same analysis as (b), comparing power in neuronal Ca^{2+} fluctuations > 0.05Hz.

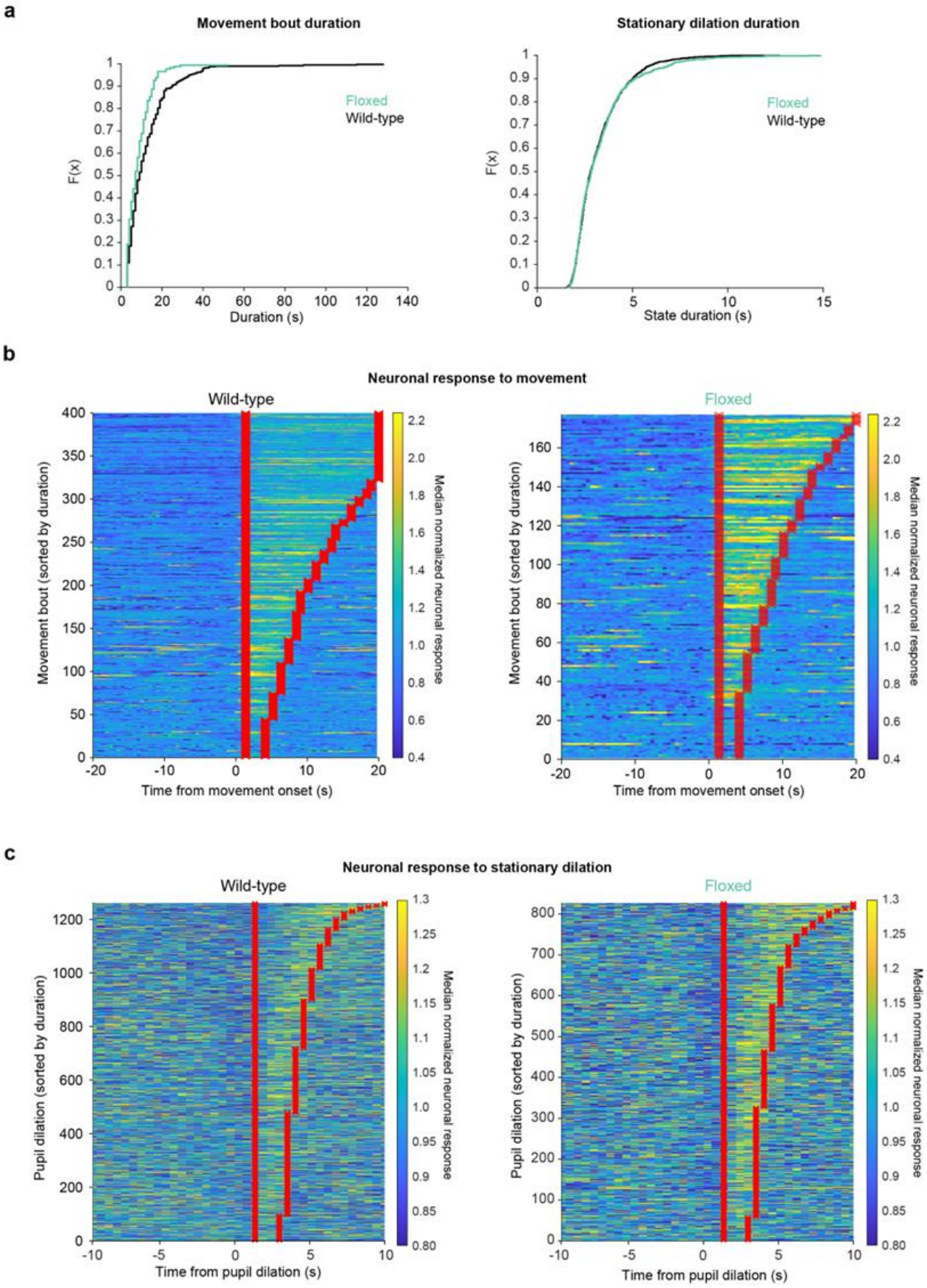
a
Movement bout duration
F(x)
Duration (s)
Floxed
Wild-type
Stationary dilation duration
State duration (s)
b
Neuronal response to movement
Wild-type
Floxed
Movement bout (sorted by duration)
Time from movement onset (s)
Median normalized neuronal response
c
Neuronal response to stationary dilation
Pupil dilation (sorted by duration)
Time from pupil dilation (s)

Extended Data Figure 8. Quantification of arousal-associated neuronal activity
(a) Cumulative distribution plots of the duration of movement bouts (left) and stationary pupil dilations (right) for wild-type (black, n = 400 movement bouts and 1396 pupil dilations) and Adra1a$^{fl/fl}$ (green, n = 177 movement bouts and n = 923 pupil dilations) mice. **(b)** Analysis range (red) used to quantify the normalized arousal PC response to movement in wild-type (left) and Adra1a$^{fl/fl}$ (right) mice. Each row represents one movement event, and the movements from all recordings and mice are concatenated to show the entire dataset (n = 4 wild-type mice and n = 4 Adra1a$^{fl/fl}$ mice). **(c)** Same analysis as in (b), showing stationary pupil dilations in Adra1a$^{fl/fl}$ mice compared to wild-type.

Supplementary Table 1. Statistics for Fig. 1d

Bin X	Bin Y	Lower bound	Difference	Upper bound	p-value	Bin #	# samp.
1	2	-240.15	-35.43	169.3	1.00E+00	1	249
1	3	-295.35	-90.42	114.5	9.29E-01	2	604
1	4	-399.03	-184.07	30.89	1.70E-01	3	600
1	5	-551.53	-324.93	-98.33	2.45E-04	4	447
1	6	-810.7	-569.21	-327.71	1.79E-07	5	341
1	7	-1223.7	-965.97	-708.21	1.79E-07	6	258
1	8	-1464.6	-1181.2	-897.87	1.79E-07	7	201
1	9	-1709.1	-1372	-1034.8	1.79E-07	8	146
1	10	-1955.5	-1502.1	-1048.6	1.79E-07	9	88
2	3	-211.68	-55	101.69	9.84E-01	10	42
2	4	-318.25	-148.64	20.96	1.46E-01		
2	5	-473.63	-289.5	-105.37	2.88E-05		
2	6	-735.96	-533.78	-331.6	1.79E-07		
2	7	-1151.9	-930.54	-709.19	1.79E-07		
2	8	-1396.5	-1145.8	-895.1	1.79E-07		
2	9	-1646.7	-1336.5	-1026.4	1.79E-07		
2	10	-1900.4	-1466.6	-1032.8	1.79E-07		
3	4	-263.49	-93.64	76.2	7.70E-01		
3	5	-418.86	-234.5	-50.15	2.31E-03		
3	6	-681.16	-478.78	-276.4	1.79E-07		
3	7	-1097.1	-875.55	-654.01	1.79E-07		
3	8	-1341.7	-1090.8	-839.94	1.79E-07		
3	9	-1591.8	-1281.5	-971.23	1.79E-07		
3	10	-1845.5	-1411.6	-977.75	1.79E-07		
4	5	-336.31	-140.86	54.59	4.02E-01		
4	6	-597.68	-385.14	-172.6	5.36E-07		
4	7	-1012.8	-781.9	-551.04	1.79E-07		
4	8	-1256.3	-997.15	-738.03	1.79E-07		
4	9	-1504.9	-1187.9	-870.87	1.79E-07		
4	10	-1756.7	-1318	-879.27	1.79E-07		
5	6	-468.58	-244.28	-19.97	2.03E-02		
5	7	-882.77	-641.04	-399.31	1.79E-07		
5	8	-1125.1	-856.29	-587.44	1.79E-07		
5	9	-1372.1	-1047	-722	1.79E-07		
5	10	-1621.7	-1177.1	-732.59	1.79E-07		
6	7	-652.51	-396.76	-141.02	4.03E-05		
6	8	-893.54	-612.02	-330.49	1.79E-07		
6	9	-1138.3	-802.75	-467.17	1.79E-07		
6	10	-1385.2	-932.85	-480.54	1.79E-07		
7	8	-510.85	-215.25	80.35	3.86E-01		
7	9	-753.46	-405.99	-58.52	8.32E-03		
7	10	-997.29	-536.09	-74.89	8.92E-03		
8	9	-557.59	-190.74	176.12	8.26E-01		
8	10	-796.81	-320.84	155.14	5.04E-01		
9	10	-639.92	-130.1	379.72	9.99E-01		

Supplementary Table 2. Statistics for Fig. 2h

Std Thresh. X	Std Thresh. Y	Lower bound	Difference	Upper bound	p-value	Std Thresh.	# samp.
0.5	1	-2386.5	-2140.6	-1894.8	2.07E-08	0.5	5551
0.5	1.5	-3965.4	-3671.2	-3376.9	2.07E-08	1	3441
0.5	2	-4833.4	-4465.9	-4098.4	2.07E-08	1.5	2023
0.5	2.5	-5737.5	-5256.7	-4775.8	2.07E-08	2	1147
0.5	3	-7316.4	-6926.3	-6536.2	2.07E-08	2.5	617
1	1.5	-1848	-1530.5	-1213.1	2.07E-08	3	995
1	2	-2711.6	-2325.3	-1938.9	2.07E-08		
1	2.5	-3611.4	-3116	-2620.6	2.07E-08		
1	3	-5193.5	-4785.7	-4377.8	2.07E-08		
1.5	2	-1213.6	-794.74	-375.91	9.70E-07		
1.5	2.5	-2106.6	-1585.5	-1064.4	2.07E-08		
1.5	3	-3693.9	-3255.1	-2816.4	2.07E-08		
2	2.5	-1356.5	-790.76	-225.03	9.61E-04		
2	3	-2951.3	-2460.4	-1969.5	2.07E-08		
2.5	3	-2250.3	-1669.6	-1089	2.07E-08		

Supplementary Table 3. Supplementary Table 3: Statistics for Fig. 2j

Prolonged

Std. Threshold	# samples	p-value
0.5	5551	7.40E-03
1	3441	3.45E-01
1.5	2023	5.21E-01
2	1147	4.52E-02
2.5	617	3.14E-03
3	995	6.38E-11

Immediate

Std. Threshold	# samples	p-value
0.5	5551	9.09E-01
1	3441	4.53E-06
1.5	2023	6.30E-03
2	1147	5.70E-06
2.5	617	6.46E-08
3	995	2.25E-06

Supplementary Table 4. Statistics for Fig. 4d

Cond. X	Cond. Y	Lower bound	Difference	Upper bound	p-val	Cond.	# samples
Sb	St	-55.885	43.189	142.26	8.16E-01	Sb	213
Sb	CNO1b	-314.17	-221.1	-128.02	2.08E-08	St	129
Sb	CNO1t	-226.4	-142.04	-57.68	2.36E-05	CNO1b	159
Sb	CNO5b	-172.33	-88.142	-3.9574	3.39E-02	CNO1t	231
Sb	CNO5t	-218.46	-115.4	-12.349	1.78E-02	CNO5b	233
St	CNO1b	-369.51	-264.28	-159.06	2.07E-08	CNO5t	114
St	CNO1t	-282.83	-185.23	-87.62	9.68E-07		
St	CNO5b	-228.79	-131.33	-33.873	1.71E-03		
St	CNO5t	-272.74	-158.59	-44.438	1.06E-03		
CNO1b	CNO1t	-12.451	79.057	170.57	1.36E-01		
CNO1b	CNO5b	41.606	132.95	224.3	4.81E-04		
CNO1b	CNO5t	-3.2907	105.69	214.68	6.34E-02		
CNO1t	CNO5b	-28.556	53.897	136.35	4.25E-01		
CNO1t	CNO5t	-75.008	26.636	128.28	9.76E-01		
CNO5b	CNO5t	-128.76	-27.261	74.239	9.73E-01		

Legend
Sb: Saline – Baseline period
St: Saline – Treatment period
CNO1b: 1mg/Kg CNO – Baseline period
CNO1t: 1mg/Kg CNO – Treatment period
CNO5b: 5mg/Kg CNO – Baseline period
CNO5t: 5mg/Kg CNO – Treatment period

1.8 References

1. Harris, K. D. & Thiele, A. Cortical state and attention. *Nat. Rev. Neurosci.* **12,** 509–523 (2011).

2. Crochet, S. & Petersen, C. C. H. Correlating whisker behavior with membrane potential in barrel cortex of awake mice. *Nat. Neurosci.* **9,** 608–610 (2006).

3. Niell, C. M. & Stryker, M. P. Modulation of visual responses by behavioral state in mouse visual cortex. *Neuron* **65,** 472–479 (2010).

4. Greenberg, D. S., Houweling, A. R. & Kerr, J. N. D. Population imaging of ongoing neuronal activity in the visual cortex of awake rats. *Nat. Neurosci.* **11,** 749–751 (2008).

5. Steriade, M., McCormick, D. A. & Sejnowski, T. J. Thalamocortical oscillations in the sleeping and aroused brain. *Science* **262,** 679–685 (1993).

6. Fries, P. Neuronal gamma-band synchronization as a fundamental process in cortical computation. *Annu. Rev. Neurosci.* **32,** 209–224 (2009).

7. Vinck, M., Batista-Brito, R., Knoblich, U. & Cardin, J. A. Arousal and locomotion make distinct contributions to cortical activity patterns and visual encoding. *Neuron* **86,** 740–754 (2015).

8. McGinley, M. J. *et al.* Waking state: rapid variations modulate neural and behavioral responses. *Neuron* **87,** 1143–1161 (2015).

9. Poulet, J. F. A. & Petersen, C. C. H. Internal brain state regulates membrane potential synchrony in barrel cortex of behaving mice. *Nature* **454,** 881–885 (2008).

10. Bennett, C., Arroyo, S. & Hestrin, S. Subthreshold mechanisms underlying state-dependent modulation of visual responses. *Neuron* **80,** 350–357 (2013).

11. Einstein, M. C., Polack, P.-O., Tran, D. T. & Golshani, P. Visually Evoked 3-5 Hz Membrane Potential Oscillations Reduce the Responsiveness of Visual Cortex Neurons in Awake Behaving Mice. *J. Neurosci.* **37,** 5084–5098 (2017).

12. Breton-Provencher, V. & Sur, M. Active control of arousal by a locus coeruleus GABAergic circuit. *Nat. Neurosci.* **22,** 218–228 (2019).

13. Liu, Y., Rodenkirch, C., Moskowitz, N., Schriver, B. & Wang, Q. Dynamic Lateralization of Pupil Dilation Evoked by Locus Coeruleus Activation Results from Sympathetic, Not Parasympathetic, Contributions. *Cell Rep.* **20,** 3099–3112 (2017).

14. Polack, P.-O., Friedman, J. & Golshani, P. Cellular mechanisms of brain state-dependent gain modulation in visual cortex. *Nat. Neurosci.* **16,** 1331–1339 (2013).

15. Carter, M. E. *et al.* Tuning arousal with optogenetic modulation of locus coeruleus neurons. *Nat. Neurosci.* **13,** 1526–1533 (2010).

16. Aston-Jones, G., Rajkowski, J., Kubiak, P. & Alexinsky, T. Locus coeruleus neurons in monkey are selectively activated by attended cues in a vigilance task. *J. Neurosci.* **14,** 4467–4480 (1994).

17. Constantinople, C. M. & Bruno, R. M. Effects and mechanisms of wakefulness on local cortical networks. *Neuron* **69,** 1061–1068 (2011).

18. Liu, Y. U. *et al.* Neuronal network activity controls microglial process surveillance in awake mice via norepinephrine signaling. *Nat. Neurosci.* **22,** 1771–1781 (2019).

19. Albertini, G., Etienne, F. & Roumier, A. Regulation of microglia by neuromodulators: Modulations in major and minor modes. *Neurosci. Lett.* **733,** 135000 (2020).

20. Stowell, R. D. *et al.* Noradrenergic signaling in the wakeful state inhibits microglial surveillance and synaptic plasticity in the mouse visual cortex. *Nat. Neurosci.* **22,** 1782–1792 (2019).

21. Nakadate, K., Imamura, K. & Watanabe, Y. Cellular and subcellular localization of alpha-1 adrenoceptors in the rat visual cortex. *Neuroscience* **141,** 1783–1792 (2006).

22. Ding, F. *et al.* α1-Adrenergic receptors mediate coordinated Ca^{2+} signaling of cortical astrocytes in awake, behaving mice. *Cell Calcium* **54,** 387–394 (2013).

23. Oe, Y. *et al.* Distinct temporal integration of noradrenaline signaling by astrocytic second messengers during vigilance. *Nat. Commun.* **11,** 471 (2020).

24. Paukert, M. *et al.* Norepinephrine controls astroglial responsiveness to local circuit activity. *Neuron* **82,** 1263–1270 (2014).

25. Ye, L. *et al.* Ethanol abolishes vigilance-dependent astroglia network activation in mice by inhibiting norepinephrine release. *Nat. Commun.* **11,** 6157 (2020).

26. Bazargani, N. & Attwell, D. Amines, astrocytes, and arousal. *Neuron* **94,** 228–231 (2017).

27. Ma, Z., Stork, T., Bergles, D. E. & Freeman, M. R. Neuromodulators signal through astrocytes to alter neural circuit activity and behaviour. *Nature* **539,** 428–432 (2016).

28. Mu, Y. *et al.* Glia Accumulate Evidence that Actions Are Futile and Suppress Unsuccessful Behavior. *Cell* **178,** 27–43.e19 (2019).

29. Bojarskaite, L. *et al.* Astrocytic Ca^{2+} signaling is reduced during sleep and is involved in the regulation of slow wave sleep. *Nat. Commun.* **11,** 3240 (2020).

30. Vaidyanathan, T. V., Collard, M., Yokoyama, S., Reitman, M. E. & Poskanzer, K. E. Cortical astrocytes independently regulate sleep depth and duration via separate GPCR pathways. *Elife* **10,** (2021).

31. Ingiosi, A. M. *et al.* A role for astroglial calcium in mammalian sleep and sleep regulation. *Curr. Biol.* **30,** 4373–4383.e7 (2020).

32. Poskanzer, K. E. & Yuste, R. Astrocytes regulate cortical state switching in vivo. *Proc. Natl. Acad. Sci. USA* **113,** E2675–84 (2016).

33. Lines, J., Martin, E. D., Kofuji, P., Aguilar, J. & Araque, A. Astrocytes modulate sensory-evoked neuronal network activity. *Nat. Commun.* **11,** 3689 (2020).

34. Wang, Y. *et al.* Accurate quantification of astrocyte and neurotransmitter fluorescence dynamics for single-cell and population-level physiology. *Nat. Neurosci.* **22,** 1936–1944 (2019).

35. Srinivasan, R. *et al.* $Ca(^{2+})$ signaling in astrocytes from Ip3r2(-/-) mice in brain slices and during startle responses in vivo. *Nat. Neurosci.* **18,** 708–717 (2015).

36. Stitt, I., Zhou, Z. C., Radtke-Schuller, S. & Fröhlich, F. Arousal dependent modulation of thalamo-cortical functional interaction. *Nat. Commun.* **9,** 2455 (2018).

37. Reimer, J. *et al.* Pupil fluctuations track fast switching of cortical states during quiet wakefulness. *Neuron* **84,** 355–362 (2014).

38. Aston-Jones, G. & Cohen, J. D. Adaptive gain and the role of the locus coeruleus-norepinephrine system in optimal performance. *J. Comp. Neurol.* **493,** 99–110 (2005).

39. Feng, J. *et al.* A genetically encoded fluorescent sensor for rapid and specific in vivo detection of norepinephrine. *Neuron* **102,** 745–761.e8 (2019).

40. Reimer, J. *et al.* Pupil fluctuations track rapid changes in adrenergic and cholinergic activity in cortex. *Nat. Commun.* **7,** 13289 (2016).

41. Stringer, C. *et al.* Spontaneous behaviors drive multidimensional, brainwide activity. *Science* **364,** 255 (2019).

42. Di Castro, M. A. *et al.* Local Ca^{2+} detection and modulation of synaptic release by astrocytes. *Nat. Neurosci.* **14,** 1276–1284 (2011).

43. Bindocci, E. *et al.* Three-dimensional Ca^{2+} imaging advances understanding of astrocyte biology. *Science* **356,** (2017).

44. Panatier, A. *et al.* Astrocytes are endogenous regulators of basal transmission at central synapses. *Cell* **146,** 785–798 (2011).

45. Chapin, J. K. & Nicolelis, M. A. Principal component analysis of neuronal ensemble activity reveals multidimensional somatosensory representations. *J. Neurosci. Methods* **94,** 121–140 (1999).

46. Armbruster, B. N., Li, X., Pausch, M. H., Herlitze, S. & Roth, B. L. Evolving the lock to fit the key to create a family of G protein-coupled receptors potently activated by an inert ligand. *Proc. Natl. Acad. Sci. USA* **104,** 5163–5168 (2007).

47. Herreras, O. Local field potentials: myths and misunderstandings. *Front. Neural Circuits* **10,** 101 (2016).

48. Pankratov, Y. & Lalo, U. Role for astroglial α1-adrenoreceptors in gliotransmission and control of synaptic plasticity in the neocortex. *Front. Cell Neurosci.* **9,** 230 (2015).

49. Farhy-Tselnicker, I. *et al.* Activity-dependent modulation of synapse-regulating genes in astrocytes. *Elife* **10,** (2021).

50. Bayraktar, O. A. *et al.* Astrocyte layers in the mammalian cerebral cortex revealed by a single-cell in situ transcriptomic map. *Nat. Neurosci.* **23,** 500–509 (2020).

51. Speed, A., Del Rosario, J., Burgess, C. P. & Haider, B. Cortical State Fluctuations across Layers of V1 during Visual Spatial Perception. *Cell Rep.* **26,** 2868–2874.e3 (2019).

52. Kohro, Y. *et al.* Spinal astrocytes in superficial laminae gate brainstem descending control of mechanosensory hypersensitivity. *Nat. Neurosci.* **23,** 1376–1387 (2020).

53. Wahis, J. & Holt, M. G. Astrocytes, Noradrenaline, α1-Adrenoreceptors, and Neuromodulation: Evidence and Unanswered Questions. *Front. Cell Neurosci.* **15,** 645691 (2021).

54. Papouin, T., Dunphy, J. M., Tolman, M., Dineley, K. T. & Haydon, P. G. Septal Cholinergic Neuromodulation Tunes the Astrocyte-Dependent Gating of Hippocampal NMDA Receptors to Wakefulness. *Neuron* **94,** 840–854.e7 (2017).

55. Vazey, E. M., Moorman, D. E. & Aston-Jones, G. Phasic locus coeruleus activity regulates cortical encoding of salience information. *Proc. Natl. Acad. Sci. USA* **115,** E9439–E9448 (2018).

56. Aston-Jones, G., Foote, S. L. & Segal, M. Impulse conduction properties of noradrenergic locus coeruleus axons projecting to monkey cerebrocortex. *Neuroscience* **15,** 765–777 (1985).

57. Bernardinelli, Y. *et al.* Activity-dependent structural plasticity of perisynaptic astrocytic domains promotes excitatory synapse stability. *Curr. Biol.* **24,** 1679–1688 (2014).

58. Bernardinelli, Y. *et al.* Astrocytes display complex and localized calcium responses to single-neuron stimulation in the hippocampus. *J. Neurosci.* **31,** 8905–8919 (2011).

59. Berridge, C. W., Schmeichel, B. E. & España, R. A. Noradrenergic modulation of wakefulness/arousal. *Sleep Med. Rev.* **16,** 187–197 (2012).

60. Stumpf, C. & Pichler, L. Synchronizing effect of the alpha 1-adrenoceptor agonist 2-(2-chloro-5-trifluoromethylphenylimino)imidazolidine on rabbit electroencephalogram. *Arzneimittelforschung.* **38,** 770–774 (1988).

61. Berridge, C. W. & Spencer, R. C. Differential cognitive actions of norepinephrine a2 and a1 receptor signaling in the prefrontal cortex. *Brain Res.* **1641,** 189–196 (2016).

62. Salgado, H., Treviño, M. & Atzori, M. Layer- and area-specific actions of norepinephrine on cortical synaptic transmission. *Brain Res.* **1641,** 163–176 (2016).

63. Perez, D. M. α1-Adrenergic Receptors in Neurotransmission, Synaptic Plasticity, and Cognition. *Front. Pharmacol.* **11,** 581098 (2020).

64. España, R. A., Schmeichel, B. E. & Berridge, C. W. Norepinephrine at the nexus of arousal, motivation and relapse. *Brain Res.* **1641,** 207–216 (2016).

65. Scammell, T. E., Arrigoni, E. & Lipton, J. O. Neural circuitry of wakefulness and sleep. *Neuron* **93,** 747–765 (2017).

66. Tyree, S. M. & de Lecea, L. Optogenetic investigation of arousal circuits. *Int. J. Mol. Sci.* **18,** (2017).

67. Thiele, A. & Bellgrove, M. A. Neuromodulation of Attention. *Neuron* **97,** 769–785 (2018).

68. McGinley, M. J., David, S. V. & McCormick, D. A. Cortical membrane potential signature of optimal states for sensory signal detection. *Neuron* **87,** 179–192 (2015).

69. Sugihara, H., Chen, N. & Sur, M. Cell-specific modulation of plasticity and cortical state by cholinergic inputs to the visual cortex. *J Physiol Paris* **110,** 37–43 (2016).

70. Lee, A. M. *et al.* Identification of a brainstem circuit regulating visual cortical state in parallel with locomotion. *Neuron* **83,** 455–466 (2014).

71. Monti, J. M. Serotonin control of sleep-wake behavior. *Sleep Med. Rev.* **15,** 269–281 (2011).

72. Celada, P., Puig, M. V. & Artigas, F. Serotonin modulation of cortical neurons and networks. *Front Integr Neurosci* **7,** 25 (2013).

73. Miller, E. K. & Buschman, T. J. Cortical circuits for the control of attention. *Curr. Opin. Neurobiol.* **23,** 216–222 (2013).

74. Speed, A., Del Rosario, J., Mikail, N. & Haider, B. Spatial attention enhances network, cellular and subthreshold responses in mouse visual cortex. *Nat. Commun.* **11,** 505 (2020).

75. Slezak, M. *et al.* Distinct Mechanisms for Visual and Motor-Related Astrocyte Responses in Mouse Visual Cortex. *Curr. Biol.* **29,** 3120–3127.e5 (2019).

76. Stobart, J. L. *et al.* Cortical circuit activity evokes rapid astrocyte calcium signals on a similar timescale to neurons. *Neuron* **98,** 726–735.e4 (2018).

77. Miller, S. J. *et al.* Molecularly defined cortical astroglia subpopulation modulates neurons via secretion of Norrin. *Nat. Neurosci.* **22,** 741–752 (2019).

78. Johnson, M. B. & Walsh, C. A. Cerebral cortical neuron diversity and development at single-cell resolution. *Curr. Opin. Neurobiol.* **42,** 9–16 (2017).

79. Pala, A. & Petersen, C. C. State-dependent cell-type-specific membrane potential dynamics and unitary synaptic inputs in awake mice. *Elife* **7,** (2018).

80. Chen, N., Sugihara, H. & Sur, M. An acetylcholine-activated microcircuit drives temporal dynamics of cortical activity. *Nat. Neurosci.* **18,** 892–902 (2015).

81. Zucca, S. *et al.* An inhibitory gate for state transition in cortex. *Elife* **6,** (2017).

82. Chen, J.-Y., Chauvette, S., Skorheim, S., Timofeev, I. & Bazhenov, M. Interneuron-mediated inhibition synchronizes neuronal activity during slow oscillation. *J. Physiol. (Lond.)* **590,** 3987–4010 (2012).

83. Sohal, V. S., Zhang, F., Yizhar, O. & Deisseroth, K. Parvalbumin neurons and gamma rhythms enhance cortical circuit performance. *Nature* **459,** 698–702 (2009).

84. Cardin, J. A. *et al.* Driving fast-spiking cells induces gamma rhythm and controls sensory responses. *Nature* **459,** 663–667 (2009).

85. Rasmussen, R. *et al.* Cortex-wide Changes in Extracellular Potassium Ions Parallel Brain State Transitions in Awake Behaving Mice. *Cell Rep.* **28,** 1182–1194.e4 (2019).

86. Tewari, B. P. *et al.* Perineuronal nets decrease membrane capacitance of peritumoral fast spiking interneurons in a model of epilepsy. *Nat. Commun.* **9,** 4724 (2018).

87. Ding, F. *et al.* Changes in the composition of brain interstitial ions control the sleep-wake cycle. *Science* **352,** 550–555 (2016).

88. Batiuk, M. Y. *et al.* Identification of region-specific astrocyte subtypes at single cell resolution. *Nat. Commun.* **11,** 1220 (2020).

89. Kiyoshi, C. M. & Zhou, M. Astrocyte syncytium: a functional reticular system in the brain. *Neural Regen. Res.* **14,** 595–596 (2019).

90. Verkhratsky, A. Physiology of neuronal-glial networking. *Neurochem. Int.* **57,** 332–343 (2010).

91. Mazaud, D., Capano, A. & Rouach, N. The many ways astroglial connexins regulate neurotransmission and behavior. *Glia* **69,** 2527–2545 (2021).

92. Rivera, A., Vanzulli, I. & Butt, A. M. A central role for ATP signalling in glial interactions in the CNS. *Curr Drug Targets* **17,** 1829–1833 (2016).

93. Shimaoka, D., Harris, K. D. & Carandini, M. Effects of arousal on mouse sensory cortex depend on modality. *Cell Rep.* **22,** 3160–3167 (2018).

94. Goldey, G. J. *et al.* Removable cranial windows for long-term imaging in awake mice. *Nat. Protoc.* **9,** 2515–2538 (2014).

95. Watson, B. O., Yuste, R. & Packer, A. M. PackIO and EphysViewer: software tools for acquisition and analysis of neuroscience data. *BioRxiv* (2016). doi:10.1101/054080

96. Saravanan, V., Berman, G. J. & Sober, S. J. Application of the hierarchical bootstrap to multi-level data in neuroscience. *Neuron. Behav. Data Anal. Theory* **3,** (2020).

97. Bokil, H., Andrews, P., Kulkarni, J. E., Mehta, S. & Mitra, P. P. Chronux: a platform for analyzing neural signals. *J. Neurosci. Methods* **192,** 146–151 (2010).

98. Pachitariu, M. *et al.* Suite2p: beyond 10,000 neurons with standard two-photon microscopy. *BioRxiv* (2016). doi:10.1101/061507

99. Watson, B. O., Levenstein, D., Greene, J. P., Gelinas, J. N. & Buzsáki, G. Network homeostasis and state dynamics of neocortical sleep. *Neuron* **90,** 839–852 (2016).

CONCLUSION

Although it was initially described about a decade ago[1,2], the extent, pattern, and role of NE activation of cortical astrocytes had remained elusive. Through this thesis work, I have described one potential role for NE-astrocyte signaling: it may act as a non-neuronal neuromodulatory pathway by which to regulate the levels and patterns of neuronal activity in the cortex. However, this work raises several questions about the role of astrocytes in circuit modulation, the receptor and cell-type specific effects of NE, and the implications for NE-astrocyte signaling as a circuit mechanism to modulate perception and behavior.

Specificity in astrocyte modulation of circuits across brain regions

In this work, we define the role of only one input, NE, on astrocytes. One primary question this work raises, therefore, is whether this activity is a specific function of NE signaling or a general function of astrocytes in response to neurotransmitters. Although the evidence is still emerging, several recent studies suggest that modulation of circuit activity is a general principle for cortical astrocytes, but the nature and sign of that modulation is likely input- and brain region-dependent.

Input-dependent astrocyte modulation of cortical activity patterns

Recent work provides some evidence that sensory-evoked astrocyte activity may have similar roles for cortical circuit modulation to those we describe here[3]. This study found that prolonged electrical foot shocks in anesthetized mice lead to cortical desynchrony, which is limited by stimulus-evoked astrocyte Ca^{2+} activity. These results suggest that the resynchronizing effect of astrocytes we describe is not NE specific, but a general

property of astrocytes regardless of the input they receive. However, sensory stimulation alone has also been shown to increase arousal, particularly when it is presented outside of task-related behavior[4,5]. Furthermore, foot shock has been used not as a sensory stimulus but as painful and stressor in other paradigms[6], which the LC is highly responsive to[7,8]. Finally, although it has been shown that astrocytes can respond to sensory stimulation independently from the effects of arousal and NE[9,10], other work suggests astrocytes can act as integrators of NE and sensory-activity[11]. Therefore, further dissection of NE versus sensory stimulation-evoked changes in astrocyte neuromodulation is necessary to understand their contributions to astrocyte-mediated cortical synchrony.

In addition, activation of differently coupled chemogenetic receptors in astrocyte somatosensory cortex has also been found to drive changes in cortical state. Using Gq-coupled Designer Receptors Exclusively Activated by Designer Drug (DREADD) expression in astrocytes, which the authors liken to acetylcholine, and Gi/o coupled DREADD expression which the authors liken to $GABA_B$, they found changes in cortical state following ligand-based activation of these receptors. Consistent with this work, the authors noted large increases in low-frequency power following activation of Gq DREADD in astrocytes. In addition, they found increases in low-frequency power following Gi-DREADD activation, but the data also shows increases in total power across the spectrum, indicating a differential effect of Gq and Gi/o pathways on cortical state in astrocytes, and by extension different effects of neuromodulators that signal through differently coupled receptors like acetylcholine and GABA[12].

Further, evidence for input-specific roles for cortical astrocytes has been found in the prefrontal cortex. $GABA_B$ receptor-mediated signaling through astrocytes was found to have an opposite role for modulating cortical circuits than described in this thesis. Instead, astrocyte activity was linked to increases in low-gamma oscillations[13]. However, similar to this thesis work, the authors observed general increases in neuronal activity which is not cell-type specific, but applies to both excitatory and inhibitory neurons. Intriguingly, other recent work has identified that astrocytes in the PFC are not endogenously sensitive to arousal, suggesting a profoundly different role in NE-mediated signaling for astrocytes in this brain region[14]. These findings together suggest that NE and GABA likely play a different role for driving astrocytic contributions to circuit function across cortical regions.

While this is not a complete survey, these studies are compelling examples of the most relevant work in the field, and provide strong recent evidence of specificity in astrocytic contributions to cortical oscillations. Although much more work needs to be done, these studies in combination with work presented in this thesis suggest that modulation of cortical state is a fundamental role for cortical astrocytes. However, these studies also suggest the possibility for input-specific roles for astrocytic neuromodulation, and region-specific differences between sensory cortices and other cortical areas.

Astrocyte modulation of circuit activity outside of the cortex

The hypothesis that astrocytes act to shape neural circuit activity is also supported from data outside the cortex, which similarly suggests a role for astrocytes in circuit modulation with region specific effects. For instance, in the mouse striatum, reducing astrocyte Ca^{2+} activity leads to reduced excitability of GABAergic medium spiny neurons

and excessive self-grooming which was linked to reductions in tonic inhibition stemming from increased GABA uptake by astrocytes[15]. This study reported that reducing astrocyte activity led to increases in correlated neuronal activity, an opposite relationship to the cortical effects I describe here. However, this finding suggests that astrocyte activity leads to appropriate regulation of circuit desynchrony and synchrony in the striatum as well as cortex, although the roles for these oscillations may be regional. However, this correlation was selectively increased during times when mice weren't grooming, Furthermore, although the striatum has little enervation by the LC, bath application of the α1-NE receptor agonist phenylephrine produced dramatic astrocytic activation in this study. These results suggest that astrocytic α1-NE receptors in the striatum might still play pivotal roles in circuit modulation, perhaps through dopaminergic activation of α1A-NE receptors as has been described in the prefrontal cortex[14].

In the hippocampus, astrocytes have been described not in coordinating the slow rhythmic activity of neurons, but rather in inducing high-frequency coupling and rhythmogenesis. This specifically matches findings for the role of astrocytes in prefrontal cortex, which is a main connection partner of the hippocampus[16], implying the role of astrocytes may be better described by functional circuit involvement than regionalization alone. Recently, these findings were extended with computational modeling which demonstrated astrocytic control of hippocampal inhibition could act as key control points for instating and maintaining high-frequency activity[17].

These studies, in combination with this thesis and other work on cortical astrocytes, suggest that modulation of neuronal circuit properties is likely a general feature of the physiological function of astrocytes. However, much like in the cortex, future work

should investigate the specificity of input pathways in driving astrocyte activity and determining their effect on cortical state. Future studies should focus not only on ligands as a whole, but also on receptor subtype-specific effects for the same ligand. This functional mapping will be crucial next steps for better integrating astrocytes into the role of circuits and behaviors.

Deeper understandings of NE-mediated control of neural circuits

Monoaminergic neuromodulation is an evolutionary ancient adaptation which has been proposed to have emerged alongside bilateralization to give rise to more complex and diverse behavioral repertoires[18]. How this is accomplished at the level of cells and circuits remains an open question in the field. One mechanism may be through differential effects by means of signaling through separate receptor families, for instance by regional and neuronal specific activation of α-NE receptors or β-NE receptors[19]. This thesis work expands on this premise, demonstrating that at an even more fine-grained level, cell-type and receptor subtype in the same family can also drastically determine the effects of neuromodulatory signaling. We show that specific activation of a subclass of α1-NE receptors can have paradoxical effects on circuit activity compared to the endogenous agonist and I argued that astrocyte-specific effects are one likely mechanism by which this paradoxical effect occurs. However, although based on the data presented here astrocytes preferentially express the Adra1A receptor, this and other work has found Adra1A on non-astrocytic cells[20,21]. These raise clear questions for other roles of Adra1A across cell-types and brain regions. It also raises questions for the combinatorial roles of NE receptor subtypes across different cells and circuits. With the newly afforded genetic access to selectively remove NE receptors in a subtype and

cell-type specific manner, future work should remove these receptors in subclasses of neurons and determine their contributions to cortical state. In addition, there is growing understanding of molecular heterogeneity across astrocytes within and outside the cortex[20,22–24]. Careful dissection of NE receptor signaling and receptor subtype on astrocytes that are regionally or molecularly distinct will be fundamental for generating a holistic view of NE-driven astrocyte functions in neural circuits.

Implications for cortical astrocytes in arousal and attention

This thesis work directly suggests astrocytes act as fundamental, endogenous, and local neuromodulatory units in the cortex and act to modify circuit activity. However, it does not provide evidence for what role this might have in the regulation of perception and behavioral functions. Below, I hypothesize potential roles of astrocyte modulation both in the generalized role of arousal, and for specific effects of attention, and suggest future avenues of research which might clarify the role of these cells in behavioral processes.

Potential astrocytic involvement in arousal-related sensation

The work presented here implicates astrocytes as fundamental players in cortical circuits, but does not answer what role this serves for perception and how it might more specifically play a role in active cortical computations. One possibility, suggested by the findings of broad inhibitory and synchronizing effects of astrocytes in response to spontaneous changes in arousal and NE, is that astrocytes act solely as a "homeostatic" dampening system to regulate and counteract the cortical effects of NE. Despite its simplicity, this model could have profound implications for astrocytes as

modulators of arousal-related cognitive function. In general, arousal-related desynchrony in the cortex sensitizes and sharpens sensory response[25]. However, in agreement with the classical view[26], excess arousal has been demonstrated to reduce sensory discrimination and behavioral performance[27]. Based on this work, astrocytes therefore may act to help keep sensory cortical circuits in a more optimal detection range by reducing the excess effects of arousal. This hypothesis may be useful as it generates several predictions beyond simply suggesting astrocytic involvement in behavior. This hypothesis predicts that dampening arousal-related astrocyte activity should reduce perceptual sensitivity during high arousal periods, but could enhance perceptual sensitivity during low arousal periods. Conversely, activating astrocytes during high arousal periods might specifically improve sensory discrimination. Future studies on sensory discrimination using the CalEx system for inhibiting astrocyte activity[15] or melanopsin-based activation of astrocytes[13], in addition to the Adra1A knockout used here, could powerfully dissect the role of astrocytes in regulating the effects of arousal on perception and behavior.

Astrocytic involvement in attention – inhibiting non-salient information

Research in mouse visual cortex has primarily focused on the effects of general arousal level, and not attention, as it was only recently that robust spatial attention paradigms in mice have been developed[28–30]. Despite these limitations, it has been suggested that many of the effects of behavioral arousal in mice are analogous to the processes underling selective attention in primates, particularly the neuromodulatory control of cortical state[31]. The findings in this work, therefore, indicate a potential role for astrocytes in attentional systems more generally, although the form this would take is

unclear. One possibility based on the work in this thesis as well as prior literature, is that astrocytes could act to specifically dampen irrelevant or non-salient activity, leading to greater signal-to-noise not in general but for the specifically attended information.

In this thesis, I describe astrocytes acting as sensitive detectors of changes in arousal and NE, in order to modulate cortical state. This sensitivity might be crucial for systems like the LC which have multiple modes of activity. For the LC, two primary modes have been described: tonic firing over longer time periods and phasic modes which occur in short bursts[32,33]. This work using a genetically encoded NE indicator suggests that astrocytes are preferentially activated by phasic increases in NE, which could provide a mechanism for widening the cortical sensitivity to phasic NE increases regardless of tonic LC activity level. Behaviorally, phasic NE has been described to encode salience and to have pivotal roles in selective attention[34,35]. It has recently been described that the P300 event related potential, often referred to as an attentional correlate, is specifically influenced by phasic activation of NE[33]. Therefore, the preferential response of astrocytes to phasic changes in NE suggests astrocytes should be highly driven by attentional tasks. Though the field is open for exploration, findings that astrocyte activity is strongly driven by salient stimuli that lead to a startle response provides preliminary evidence in support of this hypotheis[36].

What role could NE-driven astrocytic signaling have for attention? If we assume a broad non-specific inhibition and synchronization, then perhaps astrocytes help to regulate lapses in attention and mind wandering[37]. However, work from other brain regions such as the striatum indicate that astrocytes can respond and act to modulate circuits in a pathway specific manner[38]. If astrocytes act similarly in the cortex, attention-related NE

could drive pathway specific inhibition and synchronization by astrocytes, which might be a mechanism for selective attention. To assess this in the future, optogenetic, chemogenetic, and receptor knockout manipulations could be used in the context of arousal. Based on this model, activation of astrocytes would be predicted to alter performance on tasks including spatial attention[28], divided attention[39], set-shifting tasks[40], or oddball paradigms[41]. Particularly, astrocyte activation in non-salient or non-attended regions would be predicted to boost attentional performance in these tasks, and inhibition of astrocyte activity would lead to greater effects of distractors.

Summary

Understanding the variety and regulation of activity patterns in the nervous system is a daunting task. Unlike developing a map of the connectome, which can broadly state its constitutive pieces as cells and synapses, the basic units in the function and modulation of neural circuits are only beginning to be explored. In this thesis, I build on a small but growing body of literature and show astrocytes act as part of the cortical neuromodulatory system. I tie this astrocytic role directly to NE signaling and identify a previously unrecognized role for a specific receptor pathway, suggesting a new way of understanding the actions of NE in the cortex. Future studies can build off this work in order to further delineate the regional and molecular input/output properties of astrocytes and explore their role in cortical circuit regulation as it relates to cognitive control by arousal and attention.

References

1. Ding, F. *et al.* α1-Adrenergic receptors mediate coordinated Ca^{2+} signaling of cortical astrocytes in awake, behaving mice. *Cell Calcium* **54,** 387–394 (2013).

2. Bekar, L. K., He, W. & Nedergaard, M. Locus coeruleus alpha-adrenergic-mediated activation of cortical astrocytes in vivo. *Cereb. Cortex* **18,** 2789–2795 (2008).

3. Lines, J., Martin, E. D., Kofuji, P., Aguilar, J. & Araque, A. Astrocytes modulate sensory-evoked neuronal network activity. *Nat. Commun.* **11,** 3689 (2020).

4. Ganea, D. A. *et al.* Pupillary dilations of mice performing a vibrotactile discrimination task reflect task engagement and response confidence. *Front. Behav. Neurosci.* **14,** 159 (2020).

5. Aston-Jones, G. & Bloom, F. E. Norepinephrine-containing locus coeruleus neurons in behaving rats exhibit pronounced responses to non-noxious environmental stimuli. *J. Neurosci.* **1,** 887–900 (1981).

6. Bali, A. & Jaggi, A. S. Investigations in foot shock stress of variable intensity in mice: Adaptation and role of angiotensin II. *Eur. J. Pharmacol.* **761,** 86–94 (2015).

7. Suárez-Pereira, I. *et al.* The role of the Locus Coeruleus in pain and associated stress-related disorders. *Biol. Psychiatry* (2021). doi:10.1016/j.biopsych.2021.11.023

8. Palkovits, M., Baffi, J. S. & Pacak, K. The role of ascending neuronal pathways in stress-induced release of noradrenaline in the hypothalamic paraventricular nucleus of rats. *J. Neuroendocrinol.* **11,** 529–539 (1999).

9. Slezak, M. *et al.* Distinct Mechanisms for Visual and Motor-Related Astrocyte Responses in Mouse Visual Cortex. *Curr. Biol.* **29,** 3120–3127.e5 (2019).

10. Stobart, J. L. *et al.* Cortical circuit activity evokes rapid astrocyte calcium signals on a similar timescale to neurons. *Neuron* **98,** 726–735.e4 (2018).

11. Paukert, M. *et al.* Norepinephrine controls astroglial responsiveness to local circuit activity. *Neuron* **82,** 1263–1270 (2014).

12. Durkee, C. A. *et al.* Gi/o protein-coupled receptors inhibit neurons but activate astrocytes and stimulate gliotransmission. *Glia* **67,** 1076–1093 (2019).

13. Mederos, S. *et al.* GABAergic signaling to astrocytes in the prefrontal cortex sustains goal-directed behaviors. *Nat. Neurosci.* **24,** 82–92 (2021).

14. Pittolo, S. *et al.* Dopamine Activates Astrocytes in Prefrontal Cortex via α1-Adrenergic Receptors. *BioRxiv* (2022). doi:10.1101/2022.07.19.500710

15. Yu, X. *et al.* Reducing astrocyte calcium signaling in vivo alters striatal microcircuits and causes repetitive behavior. *Neuron* **99,** 1170–1187.e9 (2018).

16. Lee, H. S. *et al.* Astrocytes contribute to gamma oscillations and recognition memory. *Proc. Natl. Acad. Sci. USA* **111,** E3343–52 (2014).

17. Makovkin, S., Kozinov, E., Ivanchenko, M. & Gordleeva, S. Controlling synchronization of gamma oscillations by astrocytic modulation in a model hippocampal neural network. *Sci. Rep.* **12,** 6970 (2022).

18. Goulty, M., Botton-Amiot, G., Rosato, E. & Sprecher, S. Neuromodulation by Monoamines is a Bilaterian Innovation. *bioRxiv* (2022).

19. McCormick, D. A., Pape, H. C. & Williamson, A. Actions of norepinephrine in the cerebral cortex and thalamus: implications for function of the central noradrenergic system. *Prog. Brain Res.* **88,** 293–305 (1991).

20. Batiuk, M. Y. *et al.* Identification of region-specific astrocyte subtypes at single cell resolution. *Nat. Commun.* **11,** 1220 (2020).

21. Cahoy, J. D. *et al.* A transcriptome database for astrocytes, neurons, and oligodendrocytes: a new resource for understanding brain development and function. *J. Neurosci.* **28,** 264–278 (2008).

22. Chai, H. *et al.* Neural Circuit-Specialized Astrocytes: Transcriptomic, Proteomic, Morphological, and Functional Evidence. *Neuron* **95,** 531–549.e9 (2017).

23. Huang, A. Y.-S. *et al.* Region-Specific Transcriptional Control of Astrocyte Function Oversees Local Circuit Activities. *Neuron* **106,** 992–1008.e9 (2020).

24. Bayraktar, O. A. *et al.* Astrocyte layers in the mammalian cerebral cortex revealed by a single-cell in situ transcriptomic map. *Nat. Neurosci.* **23,** 500–509 (2020).

25. Reimer, J. *et al.* Pupil fluctuations track fast switching of cortical states during quiet wakefulness. *Neuron* **84,** 355–362 (2014).

26. Yerkes, R. M. & Dodson, J. D. The relation of strength of stimulus to rapidity of habit-formation. *J. Comp. Neurol. Psychol.* **18,** 459–482 (1908).

27. McGinley, M. J., David, S. V. & McCormick, D. A. Cortical membrane potential signature of optimal states for sensory signal detection. *Neuron* **87,** 179–192 (2015).

28. Speed, A., Del Rosario, J., Mikail, N. & Haider, B. Spatial attention enhances network, cellular and subthreshold responses in mouse visual cortex. *Nat. Commun.* **11,** 505 (2020).

29. Speed, A., Del Rosario, J., Burgess, C. P. & Haider, B. Cortical State Fluctuations across Layers of V1 during Visual Spatial Perception. *Cell Rep.* **26,** 2868–2874.e3 (2019).

30. Michaiel, A. M., Abe, E. T. T. & Niell, C. M. Dynamics of gaze control during prey capture in freely moving mice. *Elife* **9,** (2020).

31. Harris, K. D. & Thiele, A. Cortical state and attention. *Nat. Rev. Neurosci.* **12,** 509–523 (2011).

32. Devilbiss, D. M. & Waterhouse, B. D. Phasic and tonic patterns of locus coeruleus output differentially modulate sensory network function in the awake rat. *J. Neurophysiol.* **105,** 69–87 (2011).

33. Vazey, E. M., Moorman, D. E. & Aston-Jones, G. Phasic locus coeruleus activity regulates cortical encoding of salience information. *Proc. Natl. Acad. Sci. USA* **115,** E9439–E9448 (2018).

34. Aston-Jones, G. & Bloom, F. E. Activity of norepinephrine-containing locus coeruleus neurons in behaving rats anticipates fluctuations in the sleep-waking cycle. *J. Neurosci.* **1,** 876–886 (1981).

35. Aston-Jones, G. & Cohen, J. D. Adaptive gain and the role of the locus coeruleus-norepinephrine system in optimal performance. *J. Comp. Neurol.* **493,** 99–110 (2005).

36. Srinivasan, R. *et al.* Ca($^{2+}$) signaling in astrocytes from Ip3r2(-/-) mice in brain slices and during startle responses in vivo. *Nat. Neurosci.* **18,** 708–717 (2015).

37. Unsworth, N. & Robison, M. K. Tracking arousal state and mind wandering with pupillometry. *Cogn Affect Behav Neurosci* **18,** 638–664 (2018).

38. Martín, R., Bajo-Grañeras, R., Moratalla, R., Perea, G. & Araque, A. Circuit-specific signaling in astrocyte-neuron networks in basal ganglia pathways. *Science* **349,** 730–734 (2015).

39. Wimmer, R. D. *et al.* Thalamic control of sensory selection in divided attention. *Nature* **526,** 705–709 (2015).

40. Janitzky, K. *et al.* Optogenetic silencing of locus coeruleus activity in mice impairs cognitive flexibility in an attentional set-shifting task. *Front. Behav. Neurosci.* **9,** 286 (2015).

41. Ross, J. M. & Hamm, J. P. Cortical microcircuit mechanisms of mismatch negativity and its underlying subcomponents. *Front. Neural Circuits* **14,** 13 (2020).

Publishing Agreement

It is the policy of the University to encourage open access and broad distribution of all theses, dissertations, and manuscripts. The Graduate Division will facilitate the distribution of UCSF theses, dissertations, and manuscripts to the UCSF Library for open access and distribution. UCSF will make such theses, dissertations, and manuscripts accessible to the public and will take reasonable steps to preserve these works in perpetuity.

I hereby grant the non-exclusive, perpetual right to The Regents of the University of California to reproduce, publicly display, distribute, preserve, and publish copies of my thesis, dissertation, or manuscript in any form or media, now existing or later derived, including access online for teaching, research, and public service purposes.

DocuSigned by:
Michael Reitman
14E6FFC72D9E464...
Author Signature

8/26/2022
Date